

# Problem Description

Most conventional Norwegian offshore fish farms use diesel-fueled aggregates as their source of electrical power. These aggregates are often oversized to cover the peak demand. This leads to low efficiency when running at lower loads, and thus yields a very high energy cost for the system. Instead of using fossil fueled equipment, it would be desirable to exploit renewable resources available at the fish farming site. The majority of Norwegian fish farming facilities are located along the western coastline. At the same time, there is a growing trend in the industry, leading to more fish farms situated further off the shore. Here, the wind conditions are of excellent quality many places, with both steady and high wind speeds. This makes it interesting to investigate a solution where the renewable resources from wind are incorporated with the conventional diesel aggregates, in order to generate power.

The purpose of this thesis is to shed some light on the possibilities of implementing such a hybrid system solution. A major part of the thesis comprises descriptions of the system components and the control mechanisms of these. Further, a dynamic simulation model will be implemented in the MATLAB<sup>®</sup>/Simulink environment. Based on this, some critical scenarios will be investigated for assessing the system's dynamic performance. The feasibility of this is hoped to encourage further work within this topic.



# Acknowledgements

This thesis concludes my final semester as a M.Sc. student at the Department of Electric Power Engineering at NTNU. The last five years have been a fantastic journey, and I am forever grateful for the experiences I have got from the years both in Trondheim and as an exchange student in New Zealand.

First and foremost I sincerely thank my supervisor, Professor Kjetil Uhlen for great counselling and valuable advices throughout the year. Your expertise and availability are highly appreciated.

Further, a special thank you is aimed to my external contacts at NVES; Pål Preede Revheim and Thomas Bjørdal. They have provided me with a lot of information, and then some. They also took the time to organise a meeting at Smøla so that I could discuss important details for the thesis directly with relevant partners within the fish farming industry.

In addition, I would also like to thank my friend and former M.Sc. student at NTNU, Alexander Gaugstad for helping me out with the simulation model. Your help has saved me a lot of frustration this semester.

Lastly, I would like to express gratitude towards my family and friends for your love and support. Completing this degree would not have been possible without you.

Trondheim, 09.06.2017



Marius Holt





# Abstract

This thesis aims to explore feasibility related to implementing a Hybrid Wind-Diesel System for an offshore fish farm. The primary motivation behind this is to exploit the excellent wind resources along the Norwegian coast in order to reduce CO<sub>2</sub> emissions related to the operation of diesel generators (DGs). Thus, instead of diesel as the only source of electrical power, the hybrid system will utilise a wind turbine and battery system to reduce the diesel generator's operating time as much as possible. Additionally, excessive wind energy from the wind turbine could be used to run auxiliary equipment on the farm, such as oxygen production, washers for lice removal and freshwater production.

As a starting point, the thesis provides a clear and perspicuous overview of conventional offshore fish farms and Hybrid Wind-Diesel Systems in general. This constitutes the basis for building a suitable model from fundamental blocks in the MATLAB<sup>®</sup>/Simulink environment. The purpose is assessing the system's dynamic performance when exposed to disturbances. Figure 1 displays the system layout schematic.

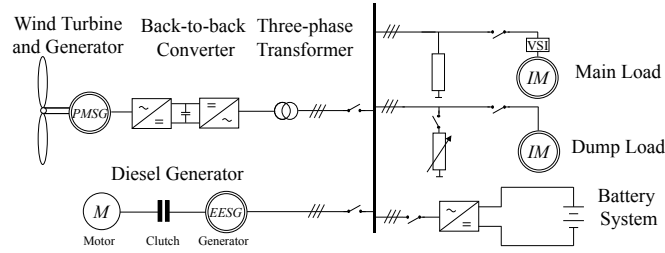


**Figure 1:** Simplified System Layout

The hybrid system comprises a Permanent Magnet Synchronous Generator (PMSG) wind turbine, connected to a 400 V AC bus bar through a back-to-back Voltage Source Converter (VSC) and a step-down transformer. The purpose of the turbine VSC is to facilitate variable speed operation of the turbine and also enhance system control. The battery is of Lithium-ion type and incorporates a VSC for AC/DC conversion. The fish farm also contains an Electrically Excited Synchronous generator (EESG) associated with a diesel engine. This can be used for fast active and reactive power support if the wind and battery system fails to cover the load. The main load is a fixed, inductive load together with a variable-speed Induction Motor (IM), and the dump load consists of a variable inductive load and a directly connected IM. Three critical situations have been investigated. These represent some of the most frequent and severe situations that the system will have to endure on a day-to-day basis. Start-up of the directly connected IM proved to be the most critical scenario, due to the high initial reactive power requirement. If sufficient resources of reactive power are not present, this may lead to a permanent voltage collapse. Starting the DG during sudden shortfall of wind indicated redundancy. However, the importance of bringing it online in generator operation and not in motor operation was highlighted. Start and stop of the feed blowers induced little stress on the system, even at low wind speeds. Overall, the system shows promising performance during most of the investigated disturbances.



# Sammendrag

Denne hovedoppgaven har i hensikt å utforske gjennomførbarheten ved et hybrid vind-diesel system for havbasert fiskeoppdrett. Hovedmotivet bak dette er å utnytte de ypperlige vindressursene som finnes langs norskekysten til å redusere CO<sub>2</sub>-utslipp i forbindelse med drift av dieselgeneratorer. I stedet for å ha dieselgenerator som den eneste elektrisitetskilden, vil det hybride systemet nyttiggjøre seg av en vindturbin og et batterisystem for å redusere driftstiden til dieselgeneratoren så mye som mulig. I tillegg kan et potensielt overskudd av vindenergi fra turbinen brukes til å kjøre annet utstyr på flåten, som oksygenproduksjon, lusespylere og ferskvannsproduksjon.

Som et naturlig startpunkt gir oppgaven en klar og tydelig oversikt over konvensjonelle havbaserte fiskeoppdrettsanlegg, samt hybride vind-diesel systemer generelt. Dette danner grunnlaget for å bygge en egnet modell ut ifra fundamentale blokker fra Simulinks bibliotek. Målet er å undersøke systemets dynamiske respons når det blir utsatt for forstyrrelser. Figur 1 viser systemutformingen.

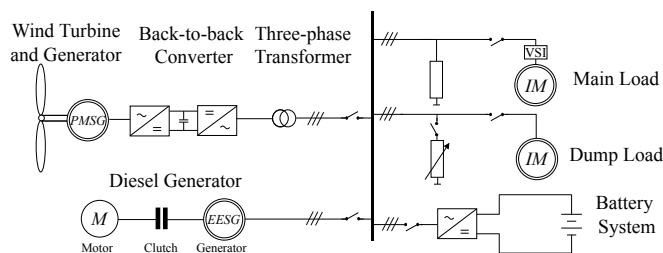


**Figure 1:** Simplified System Layout

Det hybride systemet består av en vindturbin med permanentmagnet-basert synkron-generator. Denne er koblet til en 400 V samleskinne via en back-to-back frekvensomformer og en transformator. Hensikten med turbinens frekvensomformer er å utnytte drift med variabel turbinhastighet i tillegg til å forsterke systemkontrollen. Batteriet er av typen Litium-ion og er utstyrt med en frekvensomformer. Oppdrettsanlegget innebærer også en synkron-generator, med justerbar feltmagnetisering, koblet til en dieselmotor. Denne kan brukes for rask effektregulering hvis turbinen og batterisystemet ikke dekke den aktuelle lasten. Hovedlasten består av en konstant, induktiv last sammen med en induksjonsmotor med variable hastighetskontroll. Overskuddslasten er en variabel induktiv last, i parallell med induksjonsmotor direkte koblet til samleskinnen. Tre kritiske situasjoner har blitt undersøkt. Disse representerer de hyppigste og mest kritiske situasjonene som systemet må tåle i en normal driftssituasjon. Start av den direktekoblede induksjonsmotoren viste seg å være det mest kritiske scenariet, på grunn av motorens høye forbruk av reaktiv effekt under oppstart. Hvis det ikke er tilstrekkelige reserver med reaktiv effekt i systemet, kan dette føre til en permanent spenningskollaps. Oppstart av dieselgeneratoren ved plutselig bortfall av vindkraft fremsto som redundant. Likevel ble det understreket viktigheten av å koble på aggregatet i generatordrift. Start og stopp av forblåserne viste seg å ha liten innvirkning på systemet.



# Table of Contents

	Page
<b>Problem Description</b>	<b>i</b>
<b>Acknowledgements</b>	<b>iii</b>
<b>Abstract</b>	<b>v</b>
<b>Sammendrag</b>	<b>vii</b>
<b>Glossary</b>	<b>xviii</b>
<b>1 Introduction</b>	<b>1</b>
1.1 Background and Objective . . . . .	1
1.2 Relation to Specialisation Project . . . . .	2
1.3 Scope of Work . . . . .	3
1.4 Thesis Outline . . . . .	3
1.5 Publications . . . . .	4
<b>2 The Proposed Fish Farm</b>	<b>5</b>
2.1 Description of the Farm . . . . .	5
2.2 Consumption Profile . . . . .	7
2.3 Wind Conditions at Site . . . . .	8
<b>3 Hybrid Wind-Diesel Systems</b>	<b>11</b>
3.1 System Description . . . . .	11
3.2 Voltage Source Converters . . . . .	13
3.3 Generic Control Model for VSCs . . . . .	16
3.4 The Wind Turbine System . . . . .	19
3.5 The Battery Energy Storing System . . . . .	33
3.6 Diesel Generator System . . . . .	39
3.7 Main Load . . . . .	44
3.8 Dump Load . . . . .	49

<b>4</b>	<b>Model Validation</b>	<b>51</b>
4.1	Wind System Validation . . . . .	51
4.2	Battery System Validation . . . . .	55
4.3	Diesel Generator Validation . . . . .	57
4.4	Discussion . . . . .	60
<b>5</b>	<b>Case Studies</b>	<b>63</b>
5.1	Case Study Introduction and Overview . . . . .	63
5.2	Case 1 - Starting and Stopping the Feed Blowers . . . . .	63
5.3	Case 2 - Sudden Shortfall of Wind Power . . . . .	66
5.4	Case 3 - Starting the Dump Load . . . . .	71
5.5	Discussion . . . . .	74
<b>6</b>	<b>Conclusions</b>	<b>77</b>
6.1	Shortcomings and Further Work . . . . .	78
	<b>References</b>	<b>81</b>
	<b>Appendices</b>	<b>89</b>
<b>A</b>	<b>The Park Transformation</b>	<b>90</b>
<b>B</b>	<b>Per-unit Calculation</b>	<b>91</b>
B.1	Per-unit Calculation for System 1 . . . . .	91
B.2	Per-unit Calculation for System 2 . . . . .	92
<b>C</b>	<b>Tuning of PI Controllers</b>	<b>93</b>
C.1	Modulus Optimum . . . . .	93
C.2	Symmetrical Optimum . . . . .	94
<b>D</b>	<b>Tuning of the System Controllers</b>	<b>95</b>
D.1	SSC Inner Current Controller . . . . .	95
D.2	GSC Inner Current Controller . . . . .	97

D.3	Pitch Angle Controller . . . . .	97
D.4	GSC Speed Controller . . . . .	98
D.5	SSC DC-Link Voltage Controller . . . . .	99
D.6	SSC Reactive Power Controller . . . . .	100
D.7	Battery Converter Controller . . . . .	101
<b>E</b>	<b>Derivation of Battery Parameters</b>	<b>102</b>
<b>F</b>	<b>Additional System Parameters</b>	<b>103</b>
<b>G</b>	<b>Additional Plots</b>	<b>105</b>
G.1	Wind Turbine GSC . . . . .	105
G.2	Wind Turbine SSC . . . . .	105
G.3	Battery System Control . . . . .	106
<b>H</b>	<b>IEC-61892 Standard</b>	<b>107</b>
<b>I</b>	<b>Wind Profile Model</b>	<b>108</b>
<b>J</b>	<b>The MATLAB<sup>®</sup>/Simulink Model</b>	<b>110</b>
J.1	Overall System Model . . . . .	111
J.2	Overall Wind Model . . . . .	112
J.3	Pitch Controller . . . . .	113
J.4	Aerodynamic Model . . . . .	114
J.5	GSC Model . . . . .	115
J.6	SSC Model . . . . .	116
J.7	GSC Current Control . . . . .	117
J.8	SSC Current Control . . . . .	118
J.9	Overall Battery Model . . . . .	119
J.10	Battery Converter . . . . .	120
J.11	Overall Diesel Generator Model . . . . .	121
<b>K</b>	<b>PowerPoint from EERA DeepWind'2017</b>	<b>122</b>





# List of Figures

	Page
1 Simplified System Layout . . . . .	v
2.1 Typical Offshore Fish Farm Layout as Seen From Above . . . . .	5
2.2 Yearly Variations in Daily Energy Consumption . . . . .	8
2.3 Consumption Profile for One Arbitrary Week . . . . .	8
2.4 Load Profile for Day 1 of the Year . . . . .	8
2.5 Load Profile for Day 140 of the Year . . . . .	8
2.6 Fitted Weibull Distribution with $c = 9.8$ and $k = 1.86$ . . . . .	9
2.7 Mean Wind Speed with Standard Deviation (1994-2014) . . . . .	9
3.1 Schematic of the System Layout . . . . .	12
3.2 Two-level Voltage Source Converter . . . . .	14
3.3 Pulse-Width Modulation (Single-Phase) . . . . .	15
3.4 Park Transformation Principle . . . . .	16
3.5 Complete Generic Current Controller . . . . .	17
3.6 Electric Equivalent of the Generic Equations . . . . .	18
3.7 Forces Acting on the Blades . . . . .	20
3.8 $C_p$ vs $\lambda$ Plot for Different Pitch Angles . . . . .	21
3.9 $P_{mech}$ vs $\omega_{mech}$ For Different Wind Speeds . . . . .	22
3.10 Fitted vs Discrete Power Curve . . . . .	23
3.11 Pitch Angle Controller . . . . .	23
3.12 One-Mass Drive Train Model . . . . .	24
3.13 Equivalent Circuit for SG in the dq frame . . . . .	27
3.14 Grid Side Converter Control Overview . . . . .	28
3.15 System Side Converter Control Overview . . . . .	29
3.16 Equivalent Circuit for SSC in the dq frame . . . . .	30
3.17 Per-unit Equivalent of VSC . . . . .	30
3.18 Typical Voltage-Droop Curve . . . . .	32
3.19 Principle of a LFP Battery During Discharge . . . . .	34
3.20 Battery Voltage vs Depleted Energy at 50 A Discharge Current . . . . .	37
3.21 Battery Converter Control . . . . .	38
3.22 Diesel Generator Schematic . . . . .	39
3.23 Diesel Engine Speed Governor Control . . . . .	40
3.24 Per-phase SM Equivalent . . . . .	41
3.25 Phasor Diagram for Lagging Load . . . . .	42
3.26 AC5A Exciter Block Diagram . . . . .	43
3.27 Main Load Schematic . . . . .	44
3.28 Variable Speed Induction Machine . . . . .	45
3.29 IM Torque-Speed Characteristic for Different $R_2$ . . . . .	46
3.30 Centrifugal Load Torque-Speed Characteristic . . . . .	47
3.31 TN-S Configuration Schematic . . . . .	48
3.32 The Dump Load Investigated . . . . .	49

4.1	Wind System Behaviour . . . . .	53
4.2	FFT Analysis of Current at PCC . . . . .	54
4.3	Battery System During Discharge . . . . .	56
4.4	FFT Analysis of Battery Current at the PCC . . . . .	57
4.5	Diesel Generator Behaviour During Changing Load . . . . .	59
5.1	System Behaviour During Start of Feed Flowers . . . . .	65
5.2	System Behaviour During Sudden Loss of Wind Power . . . . .	67
5.3	DG Speed, Terminal Voltage and Field Voltage . . . . .	68
5.4	Improved System Behaviour During Sudden Loss of Wind Power . . . . .	69
5.5	Improved DG Speed, Terminal Voltage and Field Voltage . . . . .	70
5.6	System Behaviour During Start of Dump Load . . . . .	72
5.7	Voltage Collapse During Start of 10 kVA IM . . . . .	73
B.1	Per-unit System Division . . . . .	91
C.1	Modulus Optimum Transfer Function . . . . .	94
C.2	Symmetrical Optimum Transfer Function . . . . .	94
D.1	Step Response for Current Controller . . . . .	96
D.2	Nichols Diagram for Current Controller . . . . .	96
D.3	Nichols Diagram for Pitch Controller . . . . .	97
D.4	Simulations with Varying Gain and Integral Time . . . . .	98
D.5	Nichols Diagram for DC-Link Voltage Controller . . . . .	99
D.6	Nichols Diagram for Reactive Power Controller . . . . .	100
D.7	Step Response for Battery Controller . . . . .	101
G.1	GSC Current Control, $i_d$ . . . . .	105
G.2	GSC Current Control, $i_q$ . . . . .	105
G.3	SSC Current Control, $i_d$ . . . . .	105
G.4	SSC Current Control, $i_q$ . . . . .	105
G.5	Battery Control, $v_d$ . . . . .	106
G.6	Battery Control, $v_q$ . . . . .	106

# List of Tables

	Page
3.1 Summary of Turbine Features . . . . .	20
3.2 Overview of PMSG Variables and Parameters . . . . .	26
3.3 Lithium-ion Battery Types . . . . .	35
3.4 Overview of Battery Variables and Parameters . . . . .	37
3.5 AC5A Parameters . . . . .	44
4.1 PMSG and Wind System Parameters . . . . .	51
4.2 Battery Parameters . . . . .	55
4.3 Diesel Generator Parameters . . . . .	57
E.1 Overview of Single LFP Characteristics . . . . .	102
F.1 Additional PMSG and Wind System Parameters . . . . .	103
F.2 Additional Battery Parameters . . . . .	103
F.3 Additional Diesel Generator Parameters . . . . .	103
F.4 DG Governor Control Parameters . . . . .	103
F.5 DG AC5A Exciter Parameters . . . . .	104
F.6 Feed Blower IM General Parameters . . . . .	104
F.7 Fixed-Speed IM General Parameters . . . . .	104
H.1 Extraction of Relevant IEC-61892 Data . . . . .	107



# Glossary

AC	✧	Alternating Current
AVR	✧	Automatic Voltage Regulator
BEM	✧	Blade Element Method
BESS	✧	Battery Energy Storage System
DC	✧	Direct Current
DFIG	✧	Doubly-Fed Induction Generator
DG	✧	Diesel generator
DoD	✧	Depth of Discharge
GSC	✧	Generator Side Converter
HAWT	✧	Horizontal Axis Wind Turbine
IGBT	✧	Insulated Gate Bipolar Transistor
IM	✧	Induction Motor
KCL	✧	Kirchhoff's Current Law
KVL	✧	Kirchhoff's Voltage Law
LFP	✧	Lithium Ferrophosphate/Lithium Iron Phosphate
Li-ion	✧	Lithium-ion
MOSFET	✧	Metal Oxide Semiconductor Field Effect Transistor
MPPT	✧	Maximum Power Point Tracking
N	✧	Neutral (conductor)
NVES	✧	Nasjonalt Vindenergisenter Smøla
PCC	✧	Point of Common Coupling
PE	✧	Protective Earth (conductor)
PLL	✧	Phase Locked Loop

PMSG	✦	Permanent Magnet Synchronous Generator
pu	✦	Per-unit
PV	✦	Photovoltaic
PWM	✦	Pulse-Width Modulation
SM	✦	Synchronous Machine
SOC	✦	State of Charge
SSC	✦	System Side Converter
TN-S	✦	Terra Neutral-Separated
VSC	✦	Voltage Source Converter
VSI	✦	Voltage Source Inverter
WFF	✦	Welfare Fish Farming

# 1 || Introduction

## 1.1 Background and Objective

Norway is blessed with a long coastline which spans over more than 100 000 km in total, bringing with it many excellent conditions for offshore fish farming [1]. Ever since the very start with a few enthusiasts in the early 1970's, aquaculture has become an increasingly important part of the Norwegian economy. In 2015, the export value of Norwegian aquaculture was around 47 billion Norwegian Crowns [2], which makes Norway the second largest exporter of fish farming products in the world after China [3].

Many Norwegian fish farming facilities are located in remote areas along the Norwegian coastline. For these facilities, grid connection often involves either very high investment costs or an unacceptably high grid loss. A consequence of this is that diesel fueled generators currently power most of these fish farms, as they are considered both robust and accessible. The diesel generators are also flexible in response to a variable demand. However, they are often over-dimensioned to meet the peak load [4]. This results in extensive periods where the engines are operated at low output power compared to nominal power, thus yielding high CO<sub>2</sub> emissions and a very low efficiency. Another drawback with diesel engines is the constant need for importation of diesel fuel, which is both expensive and a possible threat to the fragile surrounding ecosystem, if not handled properly. The wind conditions along the Norwegian coastline are excellent in many places. Therefore, it would be desirable to replace as much as possible of the diesel generators with energy from local renewable sources - such as wind power.

The Norwegian government has stated a goal for Norway to become the world's leading nation within seafood [5]. However, if this radical expansion is to be a reality, several responsibilities and challenges concerning fish health and environmental sustainability, have to be overcome. The biggest challenges present today concerns sea lice, escaping fish, excessive biological waste and CO<sub>2</sub> emissions.

In order to cope with these increasing problems, the Norwegian government has decided to actuate a new and comprehensive monitoring system of all fish farms [6]. This should be governed by indicators describing the environmental impact in addition to the establishment of 12 production zones along the coast. The hope is that these new regulations can improve the overall control and efficiency, and ultimately stimulate further growth in the industry. Another important governmental initiative regards distribution of concessions specially meant for research and development projects [7].

A consortium called Pure Farming AS submitted an application with a research related concession to the Department of Fisheries in May 2016. The proposition is named «Welfare Fish Farming» (WFF) and aims to facilitate environmentally friendly fish farming through an energy neutral fleet solution - with total control of sea lice.

A core part of the proposed concept is a Hybrid Wind-Diesel System exploiting a battery storage to supply the fleet with electrical power. The key motivation is to reduce the CO<sub>2</sub> emissions while improving fish health.

Even though hybrid system theory is relatively mature, no such system exists in the fish farming industry at present. Some preliminary studies have been performed considering economic feasibility and technical design choices [8] [9]. Nevertheless, [8] is a small project work and [9] is a bachelor thesis. Because of this, they are highly simplified due to their limited amount of time, and thus lack realism. Therefore, the primary objective of this study concerns implementing a detailed, dynamic model of the fictitious hybrid system. The purpose of this model will be to assess the system's ability to remain stable during normal and critical situations. Such critical situations may involve a sudden loss of wind power, start and stop of machinery and rapid changes in load.

As mentioned in the Problem Description, the MATLAB<sup>®</sup>/Simulink environment is used in the modular procedure of the system. MATLAB<sup>®</sup> is chosen due to its versatility. It is widely used within the university, it possesses excellent graphical tools for curve plotting, and it is compatible with other customisable programs. Simulink is an example of such software, specialised within multidomain dynamic analyses. MATLAB<sup>®</sup> was also used in the prefatory specialisation project. Therefore Simulink seems like a natural continuation for evaluating dynamic properties.

## 1.2 Relation to Specialisation Project

This master thesis is closely connected to the specialisation project written in the fall of 2016 [10]. The project title was "A Hybrid Wind-Diesel Stand-Alone System for Fish Farming Applications", and its main purpose was to discuss the possibilities of diesel fuel reduction by changing to a hybrid solution for conventional fish farms. This was performed through a steady-state performance model made in MATLAB<sup>®</sup>. In this thesis, the development of a dynamic system model has been the centre of focus. Therefore, this work deviates substantially from the specialisation project relating to the analysis part. However, the main core - namely the fish farm facility - remains the same. Thus some of the content in the project report has been re-used in this thesis, in order to create an independent and comprehensive text. This includes most of Chapter 2 and some parts of Chapter 3. Other parts may also have been re-used, but it should be noted that most of the re-used material is either rewritten or summarised.



## 1.3 Scope of Work

The workings of this thesis are confined to an introductory feasibility study on a Hybrid Wind-Diesel System for fish farming applications. The primary focus has been directed towards implementing a dynamic model. Control system for the power electronic converters present in the system has been built from scratch, as these have a significant impact on system behaviour and stability. Based on the developed Simulink model, three of the most frequent and critical situations that the system will have to endure on a day-to-day basis are examined. The results are mainly linked towards checking possible violations of frequency and voltage grid codes (e.g. IEC-61892), in addition to overall system stability during these disturbances. Some central assumptions and limitations should be stated:

- ❖ A sea cable connecting the fish farm to land is assumed to be uneconomical and involve an unacceptably high grid loss. Thus, it is not considered as an option in this thesis.
- ❖ The electrical wires connecting the system are not modelled. This is due to the short distances that are present. Hence losses within the cables is neglected.
- ❖ An overall control scheme, which incorporates the whole system logic is not implemented, due to time considerations.
- ❖ In order to not gap too wide, economic analyses have been omitted in this project.

The above-mentioned assumptions and other aspects that could be further inspected are discussed in section «Shortcomings and further work».

It should be mentioned that the author had no previous knowledge within the field of variable-speed control when starting on this thesis. Thus, a substantial amount of time of this semester has been reserved to understand and create a functioning simulation model with respect to the control mechanisms, as these forms the foundation of the model. It should therefore be considered a preliminary study. Nevertheless, it is hoped to enhance the interest related to including renewable energy within the Norwegian fish farming industry.

## 1.4 Thesis Outline

The structure of this thesis aims to present the motivation, theoretical background and dynamic principles of a Hybrid Wind-Diesel System in a clear and perspicuous way. Another goal is to explain the more technical aspects and mathematical models, as simple as possible with the help of suitable illustrations. In this way, very particular prescience should not be a requirement to extract the essence.

Chapter 2 - *The Norwegian Fish Farming Industry* - gives an introduction to the Norwegian fish farming industry. Section 2.1 described the proposed fish to be analysed.

It also comprises an explanation of the basic components of a conventional offshore fish farm. Sections 2.2 and 2.3 covers the expected load profile and wind conditions at site.

Chapter 3 - *Hybrid Wind-Diesel Systems* - deals with the working principles and mathematical representation of the different components of the hybrid system. Based on the mathematical descriptions, control schemes are implemented to create a dynamic simulation model of the system.

Chapter 4 - *Model Validation* - investigates the validity of the different model implementations. Simulations are executed to assess the performance and feasibility of the VSC control, for the wind model and the battery model respectively. Also, a small simulation on the diesel generator behaviour is executed.

Chapter 5 - *Case Studies* - presents main results from the three case studies. These three cases represent some of the most frequent and critical situations that the system will have to endure on a day-to-day basis.

Chapter 6 - *Conclusions* - summarises the main features of this thesis. It also includes a section discussing shortcomings and further work possibilities.

## 1.5 Publications

The author held a presentation of the specialisation project at the EERA DeepWind Conference in Trondheim 19. January 2017. The PowerPoint slides that were used are included in Appendix K.

## 2 || The Proposed Fish Farm

*In this chapter, a conceptual contemplation of the proposed fish farm is given. Following the general description is a short section on the available wind conditions at site, before the load profile of the fleet is discussed at the end of the chapter.*

### 2.1 Description of the Farm

The fish farm discussed and analysed in this thesis is not yet realised as Pure Farming's application of concession still awaits to be processed by the Department of Fisheries. The application involves either three or six concessions, where each concession constitutes a yearly production volume of 780 tonnes. In this thesis, only the situation with six concessions will be investigated, as the specialisation project used this as its basis. This is also a more typical size for already existing conventional fish farms.

The location of the proposed farm is nearby Gråøya which is a tiny island just north of Smøla on the North-Western coast of Norway. This geographical area has excellent wind conditions, making it ideal for hybrid Wind-Diesel purposes. Irrespective of the application outcome, an almost energy neutral fish farm solution with treatment of sea lice might be of great interest to the industry in the years to come. The proposed fish farm is mainly similar to conventional offshore fish farms in design and structure. What sets it apart is its source of electrical power, and how excessive power from the wind turbine can be utilised.

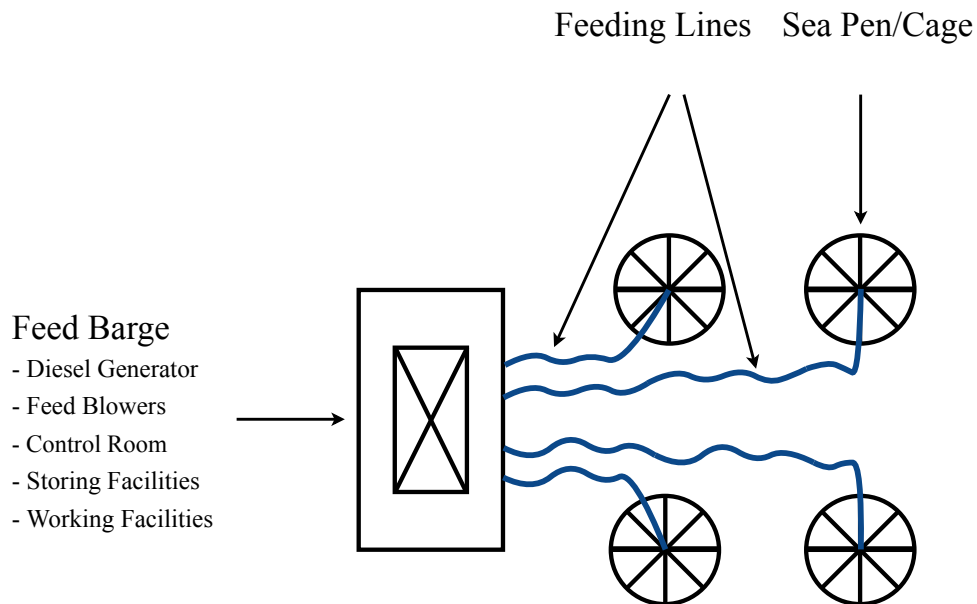


**Figure 2.1:** Typical Offshore Fish Farm Layout as Seen From Above

To get a better understanding of these farms, a conceptual contemplation of a conventional offshore fish farm layout is carried out in this section. Looking from the outside, the most conspicuous features of a fish farm are the feed barge and the surrounding sea pens of which the barge is connected to, as seen from Figure 2.1.

In rough terms, the feed barge consists of a control room, working facilities for the employees, a machine room with the diesel generators and feed blowers, and storage solutions for both feedstock and diesel fuel. It is the base station for the fish farm's employees. From the sea barge, feed lines stretch out to each of the cages. These cages are typically made of steel or plastic, depending on the surrounding environment and application. It should be clarified that the terms «sea pen» and «cages» are used interchangeably, but they represent the same. Normally, the sea pens are also equipped with lighting modules, which are used at nighttime to simulate daylight and by this stimulate growth. However, the author made a visit to Smøla 27. February 2017 to speak with participants from the fish farming industry directly. From these meetings, it became apparent that lightning of the cages, may not be as effective as previously believed. Therefore, there will not be any lightning of the cages in the fish farm discussed here.

One of the main features inside the barge is the feeding system. This consists of several components to make sure that the fish gets the right amount of food at the right time. It starts with the electrically driven feed blowers, which provides the desired air flow speed in the feeding pipes. These blowers are usually three-phase electrical induction motors (IMs), running at a nominal voltage of 400 V. Situated after these blowers there are dosage regulators to ensure that the right amount of feed from the silos are fed into the pipes. If there are several sea pens on the fleet that needs a supply of food, selective valves can be installed after the dosage regulators to disperse the pellets. All of these features are typically situated at the feed barge [11].

One of the features that sets this particular fish farm apart from other conventional farms is the source of electrical power. Instead of solely using diesel generators (DGs), a small wind turbine and a rechargeable battery will be included in a hybrid solution. The details of the hybrid Wind-Diesel system are elaborated in Chapter 3, but some main features should be mentioned first.

Wind is an intermittent source of power, which means that the wind conditions fluctuates continuously, and are almost impossible to predict with perfection. Even though good predictions can be made, there is no absolute certainty that the wind will blow when expected. Therefore, there will be times when the wind energy is able to cover the whole fish farm's load and times when there is no wind. The interesting case here occurs when there is excessive wind power compared to load available in the system. This surplus of wind energy can be used to run auxiliary which may help for improving the fish's health. Examples of such services may be the production of fresh water, oxygen and washers to remove sea lice. The machines of these auxiliary services have traditionally been run on diesel or other fossil fuels. Therefore, in this way, it is actually possible to reduce emissions while simultaneously improving the fish's health. Details about the processes of oxygen and fresh water production, together with the washers will be explained in further detail in Section 3.8.

## 2.2 Consumption Profile

The yearly energy consumption of the fleet's main load is expected to be around 470 000 kWh. In order to describe the consumption profile as precisely as possible, the load can be divided into two parts: one deterministic and one stochastic.

The deterministic part constitutes of the feed blowers since there are incorporated routines for operation of these within the industry. Throughout the year, the feed blowers are run at approximately 55% of nominal power as long as there is daylight. An explanation for why the blowers are operated at such sparse rating can be as follows: Fish feed normally consists of marine and vegetable oil that is compressed into pellets [12]. If the feed blower runs at too low power, the air pressure they create will be insufficient, which causes clogging of the feeding pipes. However, if the blowers operated at full power, the pellets may break into dust which may lead to clogging and more frequent cleaning of the pipes. Thus, they are normally operated at approximately half the rated power and only run at 100% during cleaning of the pipes (without any inlet of feed). It should be clarified that even though the blowers run as long as there is daylight, feed inlet is controlled independently by the dosage regulators to meet the fishes' demand.

There are proposed six feed blowers for the fleet, each with a nominal power rating of 27.5 kVA and power factor of 0.8. Thus, when in operation approximately 72.6 kW<sup>1</sup> and 18.2 kVAR<sup>2</sup> will be drawn by the blowers.

The stochastic load part relates to the feed barge's own consumption. This involves power to heating, lightning, the control system and other electrical facilities, in order for the barge to work on a day-to-day basis. A Gaussian distribution, with expectation of 9 kW and a standard deviation of 2 kW is found to reflect this consumption realistically.

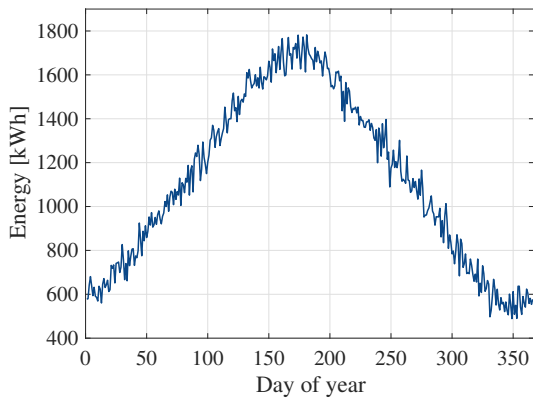
Adding the deterministic and stochastic parts together, every day for one year yields the fish farm's energy profile, as depicted in Figure 2.2. Here, the seasonal variations in daily energy consumption are shown to be substantial. During winter, with short periods of daylight the energy per day is approximately 600 kWh. On the other hand, in the summer, when the sun is up for a lot of hours, the energy demand is almost tripled with around 1760 kWh per day.

Figure 2.3 shows the active power consumed for one arbitrary week. Daily variations are clearly visible. When the blowers are in operation, the consumption lies around 80 kW ( $72.6 + 9 \approx 80$  kW). When the blowers are turned off, then the demand is only around 9 kW. Lastly, the significant difference in load between wintertime (represented by day 1 of the year) and summertime (day 140 of the year) are highlighted in Figure 2.4 and 2.5.

---

<sup>1</sup> $0.55 \cdot 6 \cdot 27.5 \cdot 0.8 = 72.6$  kW

<sup>2</sup> $0.55 \cdot 6 \cdot 27.5 \cdot 0.2 = 18.15$  kVAR



**Figure 2.2:** Yearly Variations in Daily Energy Consumption

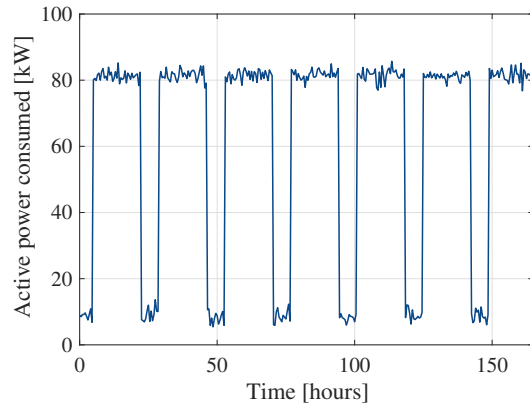


**Figure 2.3:** Consumption Profile for One Arbitrary Week

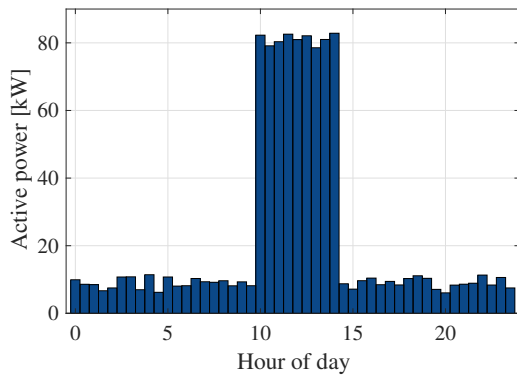


**Figure 2.4:** Load Profile for Day 1 of the Year

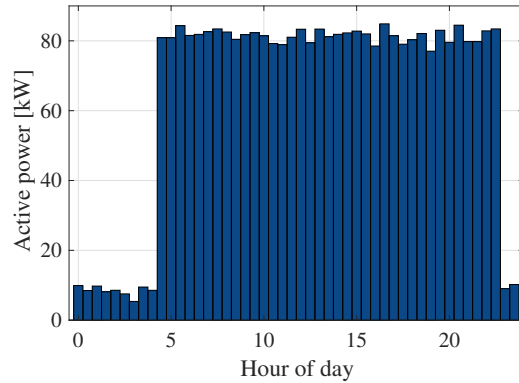


**Figure 2.5:** Load Profile for Day 140 of the Year

## 2.3 Wind Conditions at Site

This section briefly describes the wind conditions at Gråøya. Long time series with actual wind data has been collected from the measuring station at Veiholmen in the period 1994-2014. This is close to the intended location. The measurements have been performed on an hourly basis, at a height of 10 meters. As the wind turbine hub is expected to be situated at around 50 meters, a wind transformation had to be performed.

A software called WAsP have been used to estimate average wind speed at hub height. WAsP is widely used in the industry in applications for vertical and horizontal transformation of wind. Briefly put, it is a set of physical models that combines an atlas of so-called geostrophic wind (wind at high altitude), together with topographic maps, vegetation information, and other parameters to transform wind speeds from one location to another [13]. The disadvantage with WAsP is that it only provide summarised numbers and not time series. Therefore WAsP at the turbine site has been used in

combination with actual time series of wind from Veiholmen [14]. Wind speeds can usually be estimated from a Weibull distribution. This is also the case here as Figure 2.6 shows the fitted Weibull distribution at the turbine location. A scale factor,  $c$  of 9.8 and a shape factor,  $k$ , of 1.86 represents the wind distribution.

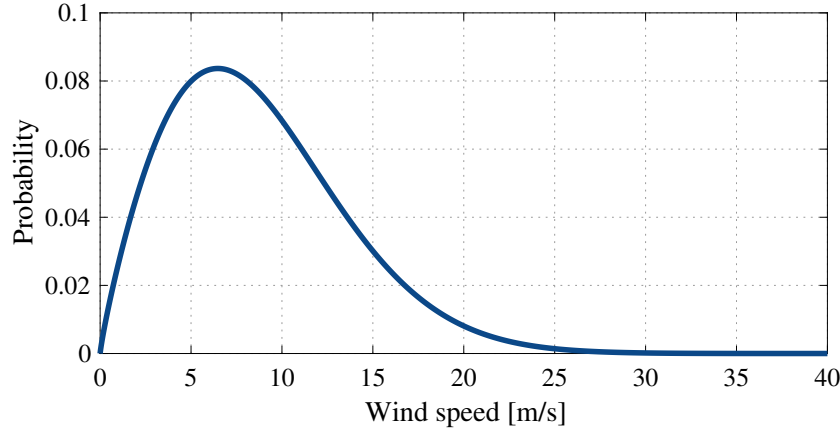


**Figure 2.6:** Fitted Weibull Distribution with  $c = 9.8$  and  $k = 1.86$

During the 21 year period with measurements, the average wind speed has been 7.37 m/s. Figure 2.7 shows the mean and standard deviation in wind speed for each for during this entire period. From this, it is clear that seasonal variations are present. In the period from May to about August, the wind speeds are lower and calmer than the rest of the year. A comparison between Figures 2.2 and 2.7 reveals that there is a negative correlation between the energy consumption and the expected wind resources over a year. Thus the wind speeds are expected lower during the summertime, when the energy demand is higher.

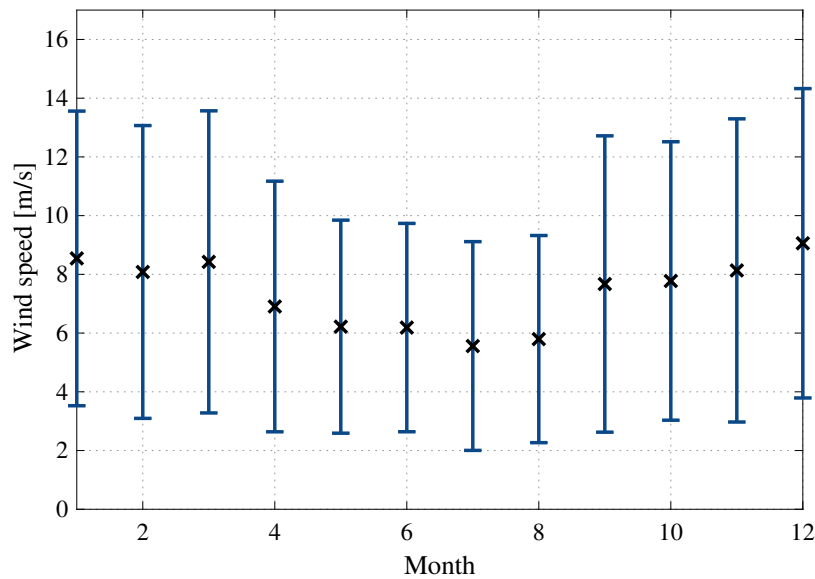


**Figure 2.7:** Mean Wind Speed with Standard Deviation (1994-2014)





# 3 || Hybrid Wind-Diesel Systems

*This chapter deals with the working principles and mathematical representation of the different components of the hybrid system. Based on the mathematical descriptions, control schemes are implemented to create a dynamic simulation model of the system.*

## 3.1 System Description

During the last decades, awareness of fossil fuel's impact on global warming has led to new energy solutions. An emerging trend is to use renewable sources in combination with conventional energy production based on fossil fuel. Such kind of systems, which exploits more than one power source are called hybrid systems.

There are several different hybrid system topologies existing today. Examples can be wind energy and diesel together (Wind-Diesel), solar energy from photovoltaic cells (PV) and diesel (PV-Diesel) or both of them together with diesel (Wind-PV-Diesel). Regardless of which renewable combination that is used, most of the hybrid systems have in common that they incorporate an energy storing system. Batteries, flywheels, large capacitors and compressed air are all examples of energy storing solutions, which may lead to increased renewable penetration<sup>1</sup>.

The reason for this is based on the intermittent nature of wind and solar power. E.g. it would be undesirable to implement a system solely based on wind energy and diesel generators (DGs), as this will likely lead to a smaller renewable penetration. Another problem this brings with it is the undesirable way of operating the DGs. Wind and sun conditions are hard to predict. Thus unforeseen shortfall of the renewable resources leads to frequent and aperiodic starting- and stopping of the DGs. This way of operating them causes increased wear and tear which ultimately reduces their lifetime. The energy storing unit can smooth these mismatches between renewable generation and load. Hence, starting and stopping of the DGs can be optimised with respect to wear, tear and cost.

The hybrid system discussed in this project is a Wind-Diesel configuration with a battery as the storage unit. The reason for using wind energy is based on the excellent wind resources that are present along the Norwegian coast. The choice of using a battery as energy storage is linked to its scalability regarding energy capacity, excellent efficiency and affordability. Batteries are applicable for both long-term and short-term storage, making them ideal for use in small-scale electrical grids with renewable

---

<sup>1</sup>Renewable penetration: How much of the load is covered by renewable sources.

penetration. Improved focus on research and development of new battery technology has led to higher competition in the market and also a reduction in cost.

A simplified single-line diagram of the proposed system is shown in Figure 3.1. To provide the reader with an extensive understanding of the system's working principles, an introduction to the different components of the studied system is given in the next sections.

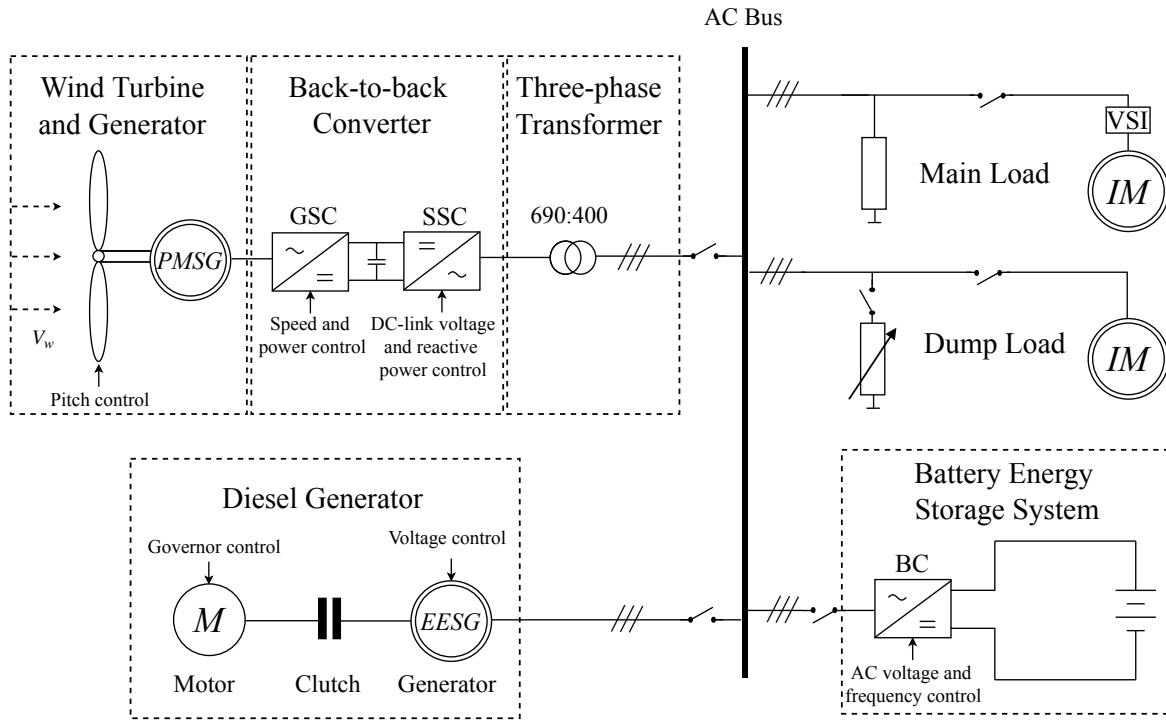


**Figure 3.1:** Schematic of the System Layout

The fundamental background and control of power electronic converters is explained in Section 3.2 and 3.3. There are three converters present in the system: Two converters in a back-to-back configuration for the wind turbine, and one VSC connected between the battery and the AC bus bar. These converters form the foundation of the hybrid system, as they facilitate control of the wind turbine generator and battery.

Further, the wind turbine system is thoroughly discussed in Section 3.4. This consists of a turbine with a Permanent Magnet Synchronous Generator (PMSG) connected to the AC bus bar through a back-to-back converter. The objective of the wind turbine is to extract as much power from the available wind as possible, and hence convert it into electrical energy. This requires several steps to explain. First, the aerodynamics are covered, before models of the pitch control, the mechanical drive train and the PMSG are all derived. The end of this section relates to the specific control of the converters.

The turbine is connected to a 400 V AC bus bar through a step-down transformer. The purpose of the transformer is to convert the wind turbine voltage of 690 V to 400 V line-to-line. It also has other advantages: e.g. it acts as a filtering component for harmonics, and it provides galvanic isolation. This might protect the wind turbine and its converters from potential over-currents and over-voltages.

Section 3.5 presents the battery system. This involves general concepts, modelling of the particular Lithium-ion (Li-ion) battery together with a control scheme of the battery converter.

The Diesel Generator (DG) principles have been covered in Section 3.6. The entire aggregate consists of a diesel engine, an electromechanical clutch and an Electrically Excited Synchronous Generator (EESG). Models for these are derived. Besides, controls for the engine's speed regulator and the generator's voltage regulator are implemented.

The last two sections of this chapter, 3.7 and 3.8, describes the main load and the dump load respectively. The main load involves the feed blowers and the required electrical power to run the barge. The feed blowers are compressors, ran on asynchronous motors. The dump load comprises the electrical components used for production of oxygen and freshwater, in addition to running washer for lice removal. These are only in operation when there is a surplus of wind energy compared to the main load in the system.

## 3.2 Voltage Source Converters

The theory covered in this section summarises some of the central aspects regarding switch-based power electronics. [15] is an excellent book on power electronics, and serves as the reference for the material presented here. A more detailed description can be found in this book.

One of the most important components of the hybrid system is the power electronic converter. A power electronic converter is in its simplest manner an electrical circuit consisting of different passive elements, composed in a way which facilitates converting and controlling of the electric circuit characteristics. They have several applications in the electric power industry today, as they can integrate AC and DC components while maintaining good efficiency. They also play a major role in renewable systems, with e.g. batteries and wind turbines - such as the one discussed in this thesis. There are a wide variety of converters existing today. One of the most common three-phase converter topologies is the two-level Voltage Source Converter (VSC). The term Voltage Source Converter originates from the ideal behaviour of a VSC. Under ideal conditions, the switching frequency is infinite. Thus, the output of the converter will be either perfect DC or perfectly sinusoidal AC. In this way, the VSC can be treated as a controllable voltage source, hence its name. Moreover, it is denoted as «two-level» because the output of the converter changes between two discrete values, either 0 or  $V_{dc}$ .

This type of VSC consists of six transistors situated with antiparallel diodes as shown in Figure 3.2. The transistors act like switches that can be in either on state or off state. A control technique called Pulse-Width Modulation (PWM) can be used to trigger the switches at specific instants in order to obtain the desired output signal. How often the switches are turned on and off is denoted as the switching frequency of the converter,  $f_s$ . Usually, this is many times higher than the system frequency. Therefore, the transistors have to provide rapid switching at low losses. Metal Oxide Semiconductor Field Effect Transistors (MOSFETs) and Insulated Gate Bipolar Transistors (IGBTs)

are the most commonly used transistors at present. MOSFET has the advantage of a very rapid switching characteristic. However, they are not suitable for high power applications. IGBTs, on the other hand, has slightly slower switching characteristics, but can handle higher power than MOSFETs. Therefore, from this point, only two-level VSCs with IGBT switches are considered. It should also be noted that they will be referred to as solely VSCs henceforth.

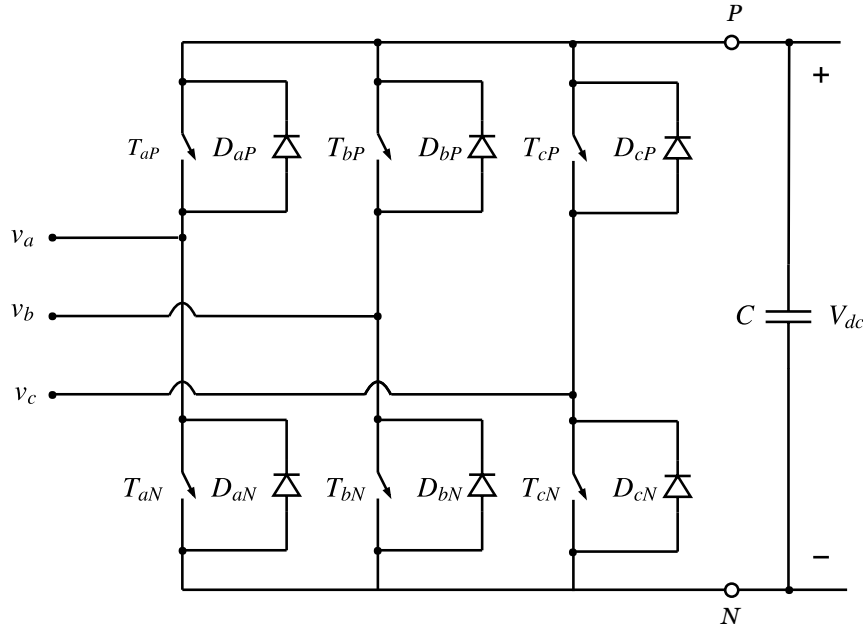


**Figure 3.2:** Two-level Voltage Source Converter

In Figure 3.2,  $v_a$ ,  $v_b$ ,  $v_c$  denotes the phase voltages,  $T_{ij}$  represents the transistors in phase  $i \in \{a, b, c\}$  connected to DC-pole  $j \in \{P, N\}$ ,  $D_{ij}$  represents the same only for the diodes and  $V_{dc}$  is the DC voltage between the positive pole  $P$  and the negative pole  $N$ . At the DC side, a large capacitor is connected to smooth the voltage waveform.

A central simplification considering the VSCs involves that the IGBT switches are treated as ideal, thus switching losses are neglected. In a real converter the switching losses increases proportionally with the switching frequency.

#### 3.2.1 Pulse-Width Modulation

Pulse-Width Modulation (PWM) is simply put a strategy describing when to trigger the different switches in a power electronic converter. Based on a comparison between two signals, the transistors are turned on and off. One of the signals is a triangular voltage pulse,  $v_{tri}$  with high frequency. This frequency is called the *switching frequency* of the converter, and is usually many times higher than the fundamental system frequency,  $f_1$ .

In this context, it is important to explain what is meant by the fundamental system frequency: In a system with power electronic converters, there will be some level of harmonic components. Simply put, this means that the voltage and current waveforms

are not perfect sinusoids. Instead, they are somewhat skewed, because they are a sum of voltages with different frequencies. Thus, the fundamental frequency of the system is the frequency of the imaginary perfect sinusoid which would have been if there were no harmonics. Another commonly used term related to this is the *frequency modulation ratio*,  $m_f$ . This describes the ratio between switching frequency and fundamental system frequency,  $m_f = \frac{f_s}{f_1}$ . In [15],  $m_f$  is defined as large if larger than 21 and small if not. Furthermore, [15] suggest that for small  $m_f$ , the frequency modulation ratio should be an odd integer and also a multiple of 3. This will minimise the harmonic components in the line-to-line voltage.

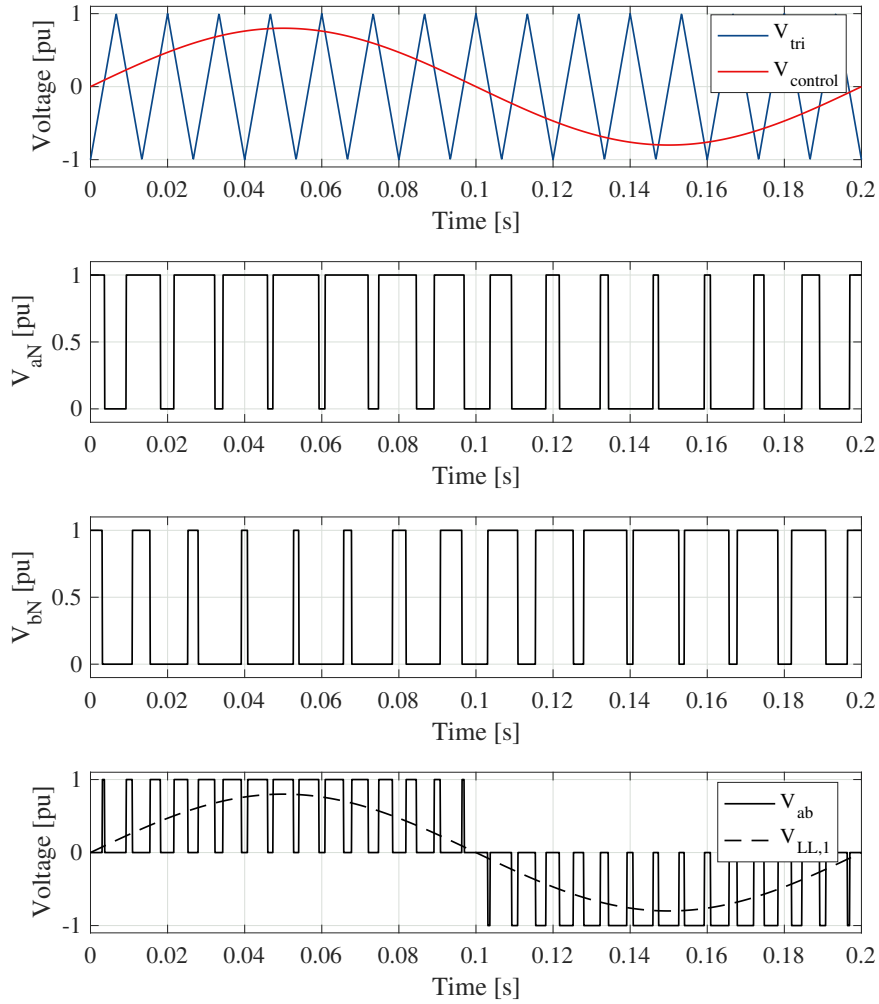


**Figure 3.3:** Pulse-Width Modulation (Single-Phase)

The other signal is called the control voltage pulse,  $v_{control}$ . This is chosen based on the desirable output waveform. In this context, a sinusoidal output waveform is desirable. Thus, the control voltage is a sinusoid and also has the fundamental frequency. The amplitude of  $v_{control}$ , denoted  $\hat{V}_{control}$ , is usually less than the peak of the triangular voltage,  $\hat{V}_{tri}$ . This ratio is called the amplitude modulation ratio,  $m_a = \frac{\hat{V}_{control}}{\hat{V}_{tri}}$ .

There are several PWM switching strategies. Two of the most discussed in literature is unipolar and bipolar switching scheme. In Figure 3.3, unipolar PWM is shown with  $f_1 = 50$  Hz,  $m_f = 15$  and  $m_a = 0.8$ . Here,  $v_{aN}$  denotes the voltage between the AC phase  $a$  and the negative DC-pole  $N$ , as seen in Figure 3.2.  $v_{bn}$  represents the same for phase  $b$ ,  $v_{ab}$  is the instantaneous line-to-line voltage and  $v_{LL,1}$  is the fundamental frequency component of the line-to-line voltage. A further explanation of PWM and details regarding the different switching schemes are found in [15].

It should be noted that the figure only shows PWM for a single-phase case. Nevertheless, the principle is directly applicable for three-phase converters. For these, the only difference is that there are three control voltages instead of one. Each of these is  $120^\circ$  out of phase as a normal balanced three-phase system.

### 3.3 Generic Control Model for VSCs

There are three bi-directional converters present in this system. Even though all of these three are VSCs, they differ in what objectives they are controlling. This is why a generic control method is described in this section. It was proposed in [16], based on [17], and is very convenient as it covers the main control features of all the three VSCs, irrespective of their application. In order to present this in a precise manner, the theoretical background of the method is explained in this section, while the specific implementation of the three converters is covered in separate sections.

The backbone of the generic method relies on the well-known Park Transformation. In steady state analysis, the  $abc$  reference frame is the most common way to describe the state of a three-phase electrical machine or system. E.g. if  $i_a$ ,  $i_b$  and  $i_c$  denotes the current in each of the phases. Then, for a balanced system,  $i_a + i_b + i_c = 0$ , as the phase difference between the phases is  $120^\circ$ . This makes it possible to do calculations on a per-phase basis. However, during transient and dynamic situations, the flux linkages between the rotor and the stator circuit becomes time dependent. This makes the coefficients of the differential equations describing the machine time-varying as well. Thus, solving these equations becomes much more complex than in steady state, and in many cases it is impossible to obtain a closed form solution.

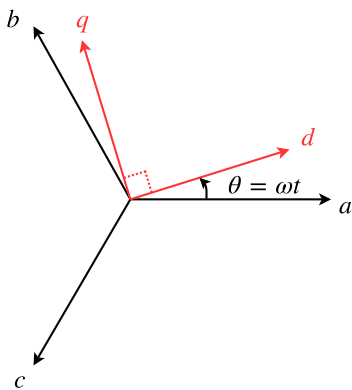


**Figure 3.4:** Park Transformation Principle

Therefore, Blondel, Doherty, Nickle and Park came up with an alternative method in the 1920's [18], [19], [20]. Instead of using the stationary  $abc$  frame, a transformation to an equivalent and rotating two-axis reference frame was proposed - called the  $dq0$  frame. Here  $d$  denotes the «direct axis»,  $q$  denotes the «quadrature axis» and  $0$  is the «zero component»<sup>2</sup>. In this way, the reference frame rotates with the system frequency. Hence time-varying variables can be treated as constants in steady state. Put in other words, in steady state the sinusoidal AC waveforms are transformed into equivalent DC quantities. This is of great use when modelling the control models of the converters, as the computational speed is expected to increase significantly [21]. Another important feature of this transformation is that it gives two degrees of freedom for control of the VSC. Because the  $d$ - and  $q$ -axis can be controlled independently, two variables of the VSC can be controlled independently as well. A mathematical description and derivation of the Park Transformation are both found in Appendix A, while a graphical illustration of the transformation frame is shown in Figure 3.4.

The fundamental structure of the VSC control is equal in all three VSCs in the system. Therefore, a general description as the one described here seems practical to avoid unnecessary repetition. The control is based on a cascaded block formation as shown in Figure 3.5. In this figure, the full block diagram for a current controller is depicted; involving the control system, the converter physics and the electrical system. The ideas behind this figure will now be outlined. Please note that the superscript '\*' denotes a variable's reference value.

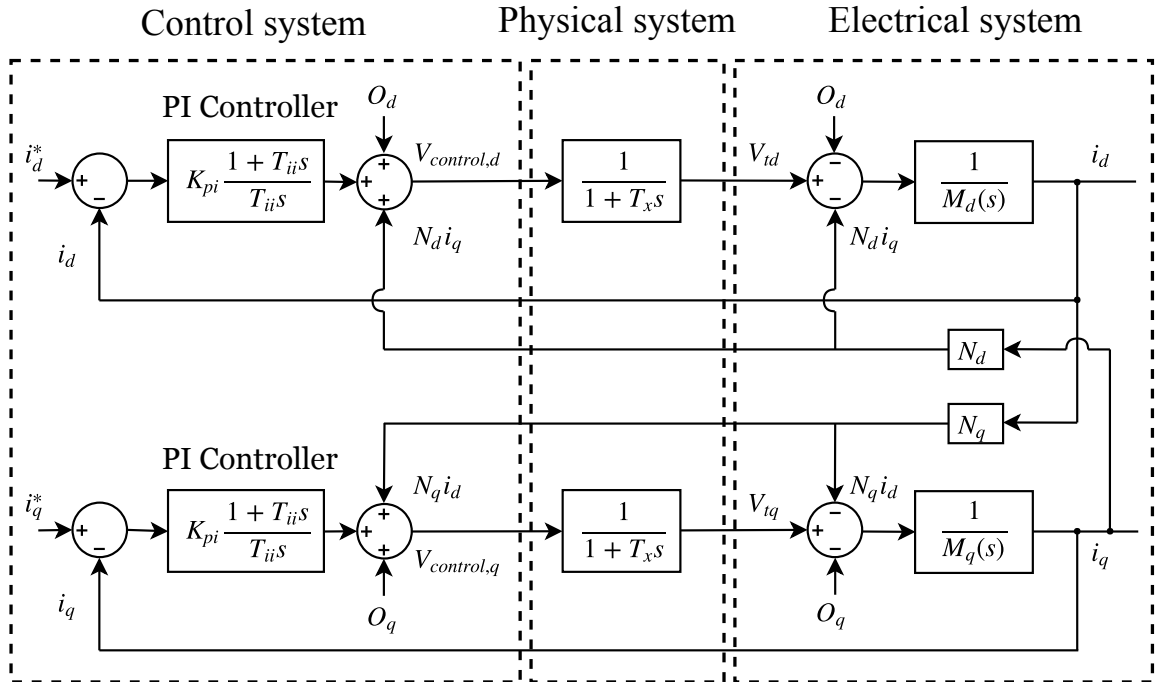


**Figure 3.5:** Complete Generic Current Controller

<sup>2</sup>The zero component is zero during balanced conditions, and will therefore not be treated further in this work. The transformation will thus be referred to solely as the  $dq$  transform.

In the controller section, the difference between the reference value and the real feedback value is fed through a PI controller. Then, the two voltages of  $N_{dq}i_{dq}$  and  $O_{dq}$  are added to the PI controller output in order to create the desired control voltage of the VSC. This is denoted  $V_{control,dq}$ .

The voltage signal will appear at the converter terminals after a time delay of  $T_x = \frac{1}{2f_s}$ , where  $f_s$  is the switching frequency [17]. Thus the time-delay related to the converter physics can be described in the Laplace domain by:

$$\begin{aligned} V_{td} &= \frac{1}{1 + T_x s} \cdot V_{control,d} \\ V_{tq} &= \frac{1}{1 + T_x s} \cdot V_{control,q} \end{aligned} \quad (3.1)$$

By using Kirchhoff's Voltage Law (KVL), the following general equations can be presented for the electrical system in the Laplace domain [16].

$$\begin{aligned} V_{td} &= M_d(s) \cdot i_{sd} + N_d \cdot i_{sq} + O_d \\ V_{tq} &= M_q(s) \cdot i_{sq} + N_q \cdot i_{sd} + O_q \end{aligned} \quad (3.2)$$

Here,  $V_{t,dq}$  is the output terminal voltage of the converter,  $i_{s,dq}$  is the line current,  $M_{dq}(s)$  is a general impedance,  $N_{dq}$  denotes the impedance link between the d- and q-axes, and  $O_{dq}$  represents a general voltage. The subscripts  $d$  and  $q$  denotes the direct- and quadrature components respectively<sup>3</sup>. A generic, electric circuit model describing equation (3.2) is established in Figure 3.6.

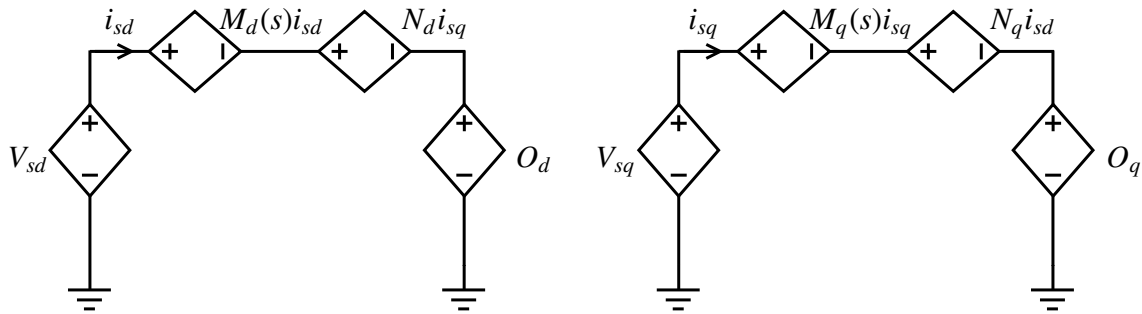


**Figure 3.6:** Electric Equivalent of the Generic Equations

---

<sup>3</sup>In the rest of this thesis the subscripts  $d$  and  $q$  represents the  $d$ - and  $q$ -component, unless stated otherwise. In addition,  $x_{dq}$  represents the general complex variable  $\vec{x}_{dq} = x_d + jx_q$ .



## 3.4 The Wind Turbine System

The type of turbine investigated in this project, and also the most common wind turbine design today, is the three bladed Horizontal Axis Wind Turbine (HAWT) [22]. In this kind of turbine, the axis of rotation is parallel to the ground. Within this category there are four main types of HAWT generators according to IEC 61400-27 [23]:

- ❖ Type 1: Asynchronous generator (usually squirrel cage) directly connected to the grid.
- ❖ Type 2: Wounded asynchronous generator with variable rotor resistance directly connected to the grid.
- ❖ Type 3: Doubly-Fed Induction Generator (DFIG). This is a wound asynchronous generator where the rotor is excited via slip rings and carbon brushes. The rotor circuit is decoupled from the grid through a power electronic converter.
- ❖ Type 4: Full-converter generators. This can be either synchronous or asynchronous generators that are decoupled from the grid by means of a power electronic converter.

During the last years, most of the new turbines on the market are either Type 3 or Type 4. The reason for this may be that both Type 3 and Type 4 generators facilitate variable-speed operation of the turbine. This is desirable as the turbine can operate at its optimal output power for a broad range of wind speeds.

The particular wind turbine assessed in this thesis is a 250 kW turbine of Type 4. It is equipped with a synchronous generator with permanent magnet rotor, and it is directly driven. The term «directly driven» implies that it does not have any gearbox. In these kinds of turbines, the generator rotor rotates at the same speed as the turbine blades, which is typically between 10-60 rounds per minute (rpm) depending on the size. The advantage of this is the increased reliability of supply, as the need of gearbox repair and maintenance of the gearbox is eliminated. Malfunctions in the gearbox have traditionally been the most frequent problem in wind turbines [9]. Several studies have been carried out on using a Permanent Magnet Synchronous Generator (PMSG), as this has higher flux density than electrically excited synchronous generators, and therefore can be made smaller [24]. This has made them economically interesting in offshore wind applications. A summary of the actual wind turbine features is shown in Table 3.1.

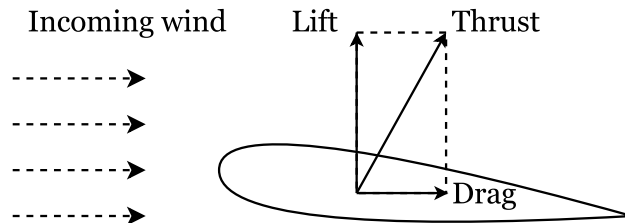
**Table 3.1:** Summary of Turbine Features

Parameter	Value/Explanation
Nominal output power	250 kW
Rotor diameter	52 m
Rotor speed range	12-26 rpm
Hub height	50 m
Cut-in wind speed	2.5 m/s
Cut-out wind speed	25 m/s
Rated wind speed	8 m/s
Generator	PMSG
Power electronic converter	Two-level VSCs, IGBT switches

The complete wind turbine model includes models for both the aerodynamic and mechanical part, in addition to an electrical system description and the control of this. The concept of pitch control is elaborated and coordinated control of the two VSCs are implemented, with a deduction of the underlying mathematical expressions.

### 3.4.1 Wind Turbine Aerodynamic Model

A detailed explanation of wind turbine aerodynamic principles will not be discussed in this thesis, as they are highly complex and a whole scientific area of its own. Nevertheless, some of the key points are emphasised in this section.

**Figure 3.7:** Forces Acting on the Blades

The fundamental principle of the turbine is to convert wind energy into electrical energy. When wind flows across the rotor blades, drag, lift and thrust forces are acting on the blades as seen from Figure 3.7. These are creating a torque which makes the turbine rotate. A method called the Blade Element Method (BEM) calculates the resulting forces acting on small blade elements. The sum of these forces describes the theoretical mechanical power that can be extracted from the wind. This is described by equation (3.3) [25].

$$P_{mech} = \tau_{mech} \cdot \omega_{mech} = \frac{1}{2} \cdot \rho \cdot A \cdot C_p(\lambda, \beta) \cdot V_W^3 \quad (3.3)$$

Here,  $\tau_{mech}$  [Nm] is the mechanical torque developed,  $\omega_{mech}$  [rad/s] is the rotational speed of the turbine,  $\rho$  [kg/m<sup>3</sup>] is the air density<sup>4</sup>,  $A$  [m<sup>2</sup>] is the effective area swept

<sup>4</sup>The air density is normally assumed to be 1.225 kg/m<sup>3</sup>, which is valid at 15°C and sea level [26].

by the rotor blades,  $C_p$  is the power coefficient and  $V_W$  is the wind speed in m/s. The effective area swept by the rotor blades can be represented by  $A = \pi \cdot R^2$ , when  $R$  is the rotor blade length, and the incoming wind is perpendicular to the rotor blades. The power coefficient describes how much power that actually is extracted from the air to the theoretically maximum power extracted [27]. It is a function of  $\lambda$  and  $\beta$ , where  $\lambda$  denotes the tip-speed ratio and  $\beta$  denotes the pitch angle of the turbine blades. The tip-speed ratio is further a function of the wind speed, rotor radius and rotational speed of the rotor shaft which is seen from equation (3.4).

$$\lambda = \frac{\omega_{mech} \cdot R}{V_W} \quad (3.4)$$

The power coefficient has a theoretical maximum limit of  $C_p \approx 0.593$ , called the Betz' limit [27]. However, modern turbines typically have  $C_p$  between 0.40-0.5. From Figure 3.8 it is seen that the maximum power coefficient for this particular turbine is around 0.41 for a tip-speed ratio of 7.95. In many cases,  $C_p$  can be difficult to measure, so a numerical approximation is often used instead [28].

$$C_p = \frac{1}{2} \cdot \left( \frac{116}{\lambda_i} - 0.4\beta - 5 \right) \cdot e^{-\frac{21}{\lambda_i}} \quad (3.5)$$

$$\frac{1}{\lambda_i} = \frac{1}{\lambda + 0.08\beta} - \frac{0.035}{1 + \beta^3} \quad (3.6)$$

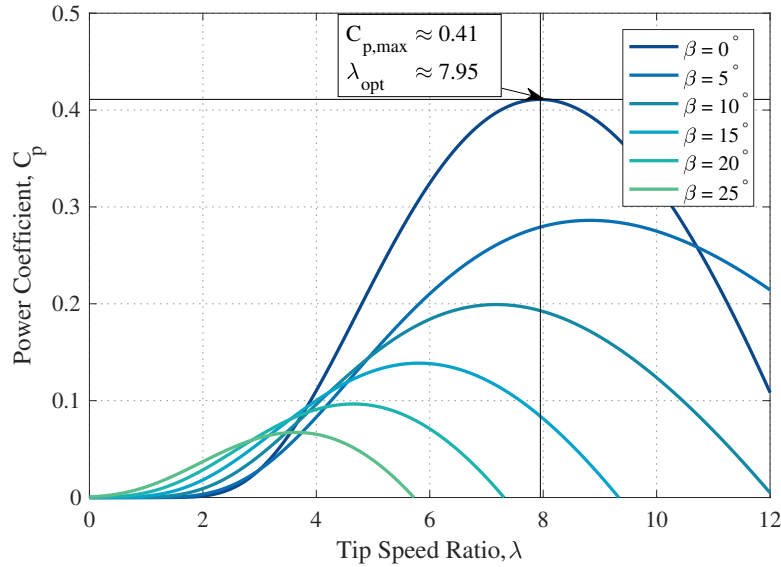


**Figure 3.8:**  $C_p$  vs  $\lambda$  Plot for Different Pitch Angles

The purpose of discussing some of the aerodynamic factors is to show that turbine output power can be manipulated in many ways. From equation (3.3) it is seen that by changing either the pitching angle, the tip-speed ratio or the effective area, output power can be adjusted. It also facilitates why variable-speed turbines are desirable. By using a variable-speed turbine, it is possible to adjust the rotational speed of the turbine in order to optimise the tip-speed ratio, and thus maximise output power. This is illustrated by the black dotted line and crosses in Figure 3.9.

### 3.4.2 Wind Turbine Pitch Control

The two main control mechanisms used for controlling wind turbine output power are pitch control and stall control. The common principle of these is to protect the turbine from mechanical stress and damage when the wind speeds are high. It is also possible to control the power by means of using the yaw mechanism. This involves rotating the whole nacelle, which manipulates the attack angle of the wind compared to the rotor blades, and thus affects the effective rotor blade area. Power control by using the yaw mechanism will not be discussed further in this thesis. Thus, a key assumption is that the rotor blades always are perpendicular to the incoming wind, hence the effective rotor area is maximised.

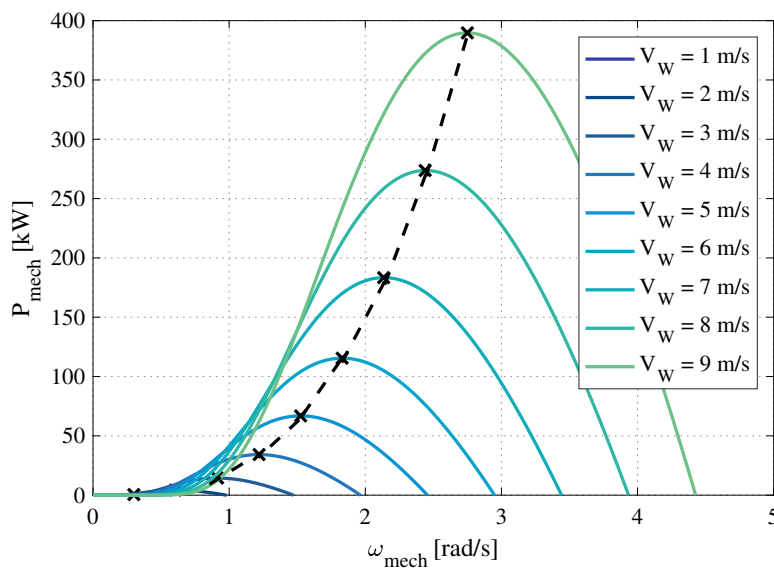


**Figure 3.9:**  $P_{mech}$  vs  $\omega_{mech}$  For Different Wind Speeds

*Pitch control* is an active form of control which involves rotating each of the rotor blades around their longitudinal axis, in order to manipulate the drag, lift and thrust forces acting on the blades. This is the most used form of control in modern wind turbines. Normally  $\beta$  is kept at  $0^\circ$  for wind speeds up to almost nominal value, because increasing the pitch angle yields lower  $C_p$  which is seen from Figure 3.8. As the wind speeds approach the nominal value of 8 m/s, the pitch angle is increased so that the electrical output power is constant at nominal value of 250 kW until cut-out speed is reached. Here, *cut-out speed* denotes the maximum wind speed that can occur before the turbine will stop producing power. On the other hand, there is also a *cut-in speed*, which describes the minimum wind speed that has to occur before the wind turbine starts to operate. This results in the power curve in Figure 3.10.

In order to avoid confusion, it is important to relate the turbine features in Table 3.1 to Figure 3.9. From the table it is stated that nominal output power from the turbine is 250 kW. This should occur at the rated wind speed of 8 m/s, and the rotor speed should be at the nominal value of 22 rpm - or  $\approx 2.3$  rad/s. However, from the figure it looks like the output power from the turbine is about 270 kW at  $\omega_{mech} = 2.3$  rad/s and  $V_W = 8$  m/s. The reason for this is the important difference between electrical

and mechanical power. In Figure 3.9 the power shown is the *mechanical* power that is possible to extract from the wind, while the rated power given in Table 3.1 is the *electrical* power delivered by the turbine generator. Thus, the figure presented seems reasonable as there will be some losses in the PMSG. This elaboration was done to stress the difference between electrical and mechanical parameters, which easily can be interchanged and misunderstood in these kinds of analyses. Another point is to account for the unhealthy trend in many papers, that present these plots without stating the underlying assumptions and units.

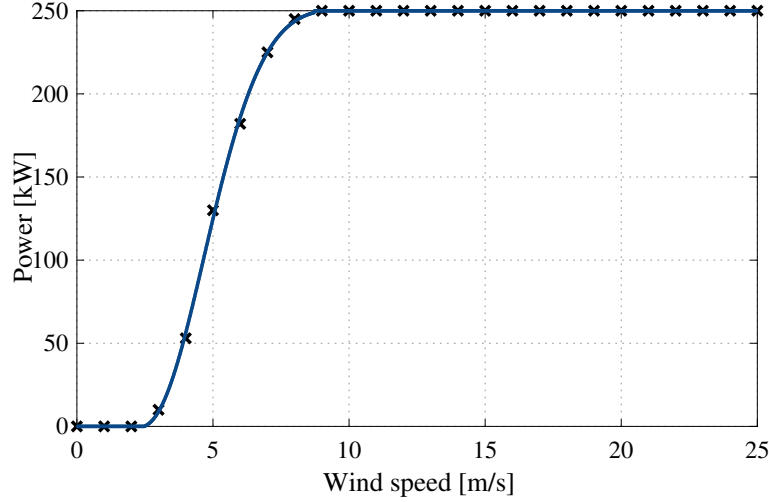


**Figure 3.10:** Fitted vs Discrete Power Curve

*Stall control* can either be an active or passive form of control. The active stall control is very similar to the regular pitch control, but with a smaller pitching interval, typically 0-4°. Turbines that use passive stall control have rotor blades that are designed such that they prevent laminar flow for too high wind speeds. This implies that for sufficiently high wind speeds, the thrust on the blades will no longer increase anymore, yielding constant rotational speed and nominal output power until the cut-off speed is reached.

Most modern turbines use pitch control adjust the output power. This is also the case for the turbine used in this thesis, which uses electrical drives to rotate the blades into the desired position. The speed of the pitching mechanism differ between the different turbine manufacturers, but most of them lie within the range of 3-10°/s. There are multiple ways of implementing a control structure for the pitch block [29]. A method using the deviation in generator power compared to the rated power is chosen here, as this is simple yet effective. The block diagram for the proposed pitch angle strategy is depicted in Figure 3.11.

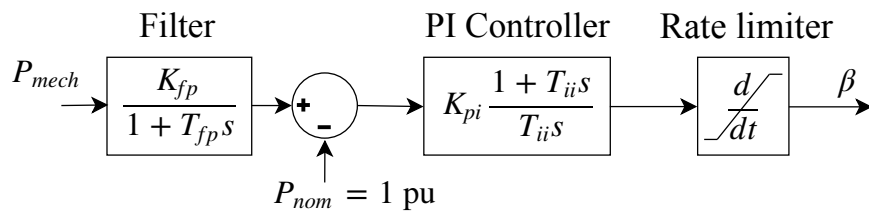


**Figure 3.11:** Pitch Angle Controller

A filter which acts as a delay is used on the input power in order to prevent the pitch controller to react on small and sudden wind gusts. The difference between the filtered  $P_{mech}$  and  $P_{nom}$  is then fed through a PI controller, which is active whenever  $P_{mech}$  is greater than  $P_{nom}$ . Further, a rate limiter restricts the rate of change in  $\beta$ . Here, this is chosen to be  $4^\circ/\text{s}$ , which is a conservative value. A closed loop branch representing the mechanical delay of pitching the blades could have been included. However, for the purpose of the analyses carried out in this work, this has been found unnecessary.

#### 3.4.3 Wind Turbine Mechanical Model

Modelling of the turbine mechanical properties can be performed in several ways, and the complexity varies widely from a highly detailed six-mass model to a simple one-mass model [30]. E.g. in [31] and [32] a two-mass model to represent the drive train is proposed. This model involves one mass representing the turbine rotor inertia,  $J_{rot}$ , and one mass representing the generator rotor inertia,  $J_{gen}$ . These two masses are connected by a flexible shaft that is characterised by a shaft stiffness,  $K$ , and a damping constant,  $D$ . The shaft is then modelled as a spring with stiffness  $K$  in parallel with a damping  $D$ .

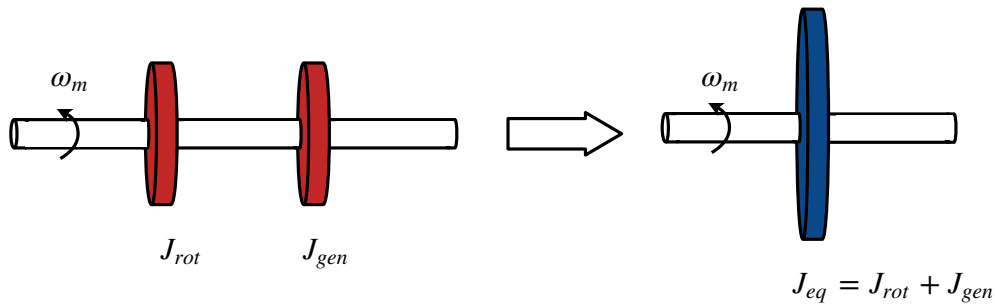


**Figure 3.12:** One-Mass Drive Train Model

However, according to [33] a lumped one-mass model should be sufficient when assessing variable speed turbine dynamics. This relies on experimental results which show that due to the decoupling effect of the power electronic converters, the dynamics of the shaft properties are hardly reflected at the grid connection point. It thus seems reasonable to represent the mechanical system by means of a one-mass model for the purpose of this work. This involves lumping the inertial constants of the turbine rotor and the generator rotor into one equivalent, rotating mass  $J_{eq} = J_{rot} + J_{gen}$ . Based on these factors, the one-mass model is assumed to retain a sufficient balance between the accurate response from the generator and the complexity of the model. A graphical illustration of the one-mass model is shown in Figure 3.12.

### 3.4.4 Synchronous Generator Model

The  $dq$ -frame introduced in Section 3.3 is chosen to model the Permanent Magnet Synchronous Generator (PMSG). A mathematical model is presented because the equations developed forms the basis for the controllers of the PMSG. The convention that is used treats current and power as positive variables when they are fed *into the generator from the grid*. Starting out with the stator circuit voltage equations from [21]:

$$\begin{aligned} v_{sd} &= R_s i_{sd} - \omega_e \lambda_{sq} + \dot{\lambda}_{sd} \\ v_{sq} &= R_s i_{sq} + \omega_e \lambda_{sd} + \dot{\lambda}_{sq} \end{aligned} \quad (3.7)$$

where  $v$  is the voltage [V],  $R$  the resistance [ $\Omega$ ],  $i$  the current [A] and  $\omega_e$  the electrical angular velocity of the generator in rad/s. Please note that in this setting,  $\lambda$  denotes the flux linkage [V·s] and not the tip-speed ratio. The subscripts  $d$  and  $q$  represents the d- and q-axis components respectively, while  $s$  denotes the stator variables. The flux linkages are further expressed as [21]:

$$\begin{aligned} \lambda_{sd} &= (L_{sd} + L_{md}) i_{sd} + \Phi_{PM} \\ \lambda_{sq} &= (L_{sq} + L_{mq}) i_{sq} \end{aligned} \quad (3.8)$$

From equation (3.8),  $L_{s,dq}$  is the stator leakage inductance [H],  $L_{m,dq}$  the mutual inductance and  $\Phi_{PM}$  [Wb] is the fixed flux created by the permanent magnets. It should also be noted that the units [V·s] and [Wb] are equivalent. Further, the active and reactive power of the PMSG are [34]:

$$\begin{aligned} P_s &= v_{sd} i_{sd} + v_{sq} i_{sq} \\ Q_s &= v_{sq} i_{sd} - v_{sd} i_{sq} \end{aligned} \quad (3.9)$$

Finally, the electromagnetic torque is given by equation (3.10), where  $P$  is the number of poles [34]:

$$\tau_e = \frac{1}{2} \cdot P \cdot i_{sq} [(L_{sd} + L_{md}) i_{sd} - (L_{sq} + L_{mq}) i_{sd} + \Phi_{PM}] \quad (3.10)$$

#### 3.4.4.1 Model Simplification

In order to reduce the complexity of the PMSG model slightly, a reasonable assumption is made: The permanent magnets are assumed to be surface mounted. Thus, the rotor is treated as non-salient due to the large number of poles in the rotor [35]. This implies that  $L_{sd} = L_{sq} = L_s$  and  $L_{md} = L_{mq} = L_m$ . The effect of saliency could be included, however, the objective of this thesis is not to implement an optimal model of all the components, but rather explore the dynamics on how they interact during different situations.

### 3.4.4.2 Simplified PMSG Model

Incorporating the mentioned simplification results in the following mathematical model:

$$\begin{aligned} v_{sd} &= R_s i_{sd} - \omega_e \lambda_{sq} + \dot{\lambda}_{sd} \\ v_{sq} &= R_s i_{sq} + \omega_e \lambda_{sd} + \dot{\lambda}_{sq} \end{aligned} \quad (3.11)$$

Here it is seen that equation (3.7) is the same as equation (3.11), thus the voltage equations remain unchanged. The flux linkage equations are on the other hand reduced to:

$$\begin{aligned} \lambda_{sd} &= L_s i_{sd} + \Phi_{PM} \\ \lambda_{sq} &= L_s i_{sq} \end{aligned} \quad (3.12)$$

This gives a simplified expression for the electromagnetic torque developed:

$$\tau_e \approx \frac{P}{2} \cdot i_{sq} \cdot \Phi_{PM} \quad (3.13)$$

Further, the rotational motion of the generator is governed by the following equation:

$$J_{eq} \frac{d\omega_{mech}}{dt} = \tau_{mech} + \tau_e \quad (3.14)$$

with  $J_{eq} = J_{rot} + J_{gen}$  [kg·m<sup>2</sup>], where  $J_{rot}$  is the turbine inertia and  $J_{gen}$  is the generator inertia. Thus,  $J_{eq}$  is the total equivalent inertia of both the turbine and the generator. In addition,  $\omega_{mech}$  [rad/s] is the drive train mechanical speed and  $\tau_{mech}$  [Nm] is the mechanical torque. Two important observations are made from the equation (3.13) and (3.14): Firstly, when a non-salient rotor is assumed, then the electromechanical torque is independent on  $i_{sd}$ . Secondly, the plus sign before  $\tau_e$  in (3.14) is caused by the convention used. In generator operation the current flows out of the stator, so then  $i_{sq}$  is negative with the convention and thus also  $\tau_e$ . A summary of the relevant variables used in the derivations is shown in Table 3.2.

**Table 3.2:** Overview of PMSG Variables and Parameters

$v_s$	Stator Voltage	$\tau_e$	Electromagnetic Torque
$R_s$	Stator Resistance	$L_s$	Stator Leakage Inductance
$i_s$	Stator Current	$L_m$	Mutual Inductance
$\omega_e$	Electrical Speed	$P$	Number of Poles
$\Phi_{PM}$	Permanent Flux	$J_{eq}$	Total Turbine Inertia
$\tau_{mech}$	Mechanical Torque	$\omega_{mech}$	Mechanical Speed

The flux linkages of equation (3.12) can be inserted into the stator voltages in equation (3.11). Then these can be transformed into the Laplace domain and further rearranged in order to match the generic form of equation.



$$\begin{aligned}
 v_{sd} &= \underbrace{(R_s + sL_s)}_{M_d(s)} i_{sd} - \underbrace{\omega_e L_s}_{N_d} i_{sq} + \underbrace{0}_{O_d} \\
 v_{sq} &= \underbrace{(R_s + sL_s)}_{M_q(s)} i_{sq} + \underbrace{\omega_e L_s}_{N_q} i_{sd} + \underbrace{\omega_e \Phi_{PM}}_{O_q}
 \end{aligned} \tag{3.15}$$

The electric equivalent is then as shown in Figure 3.13.

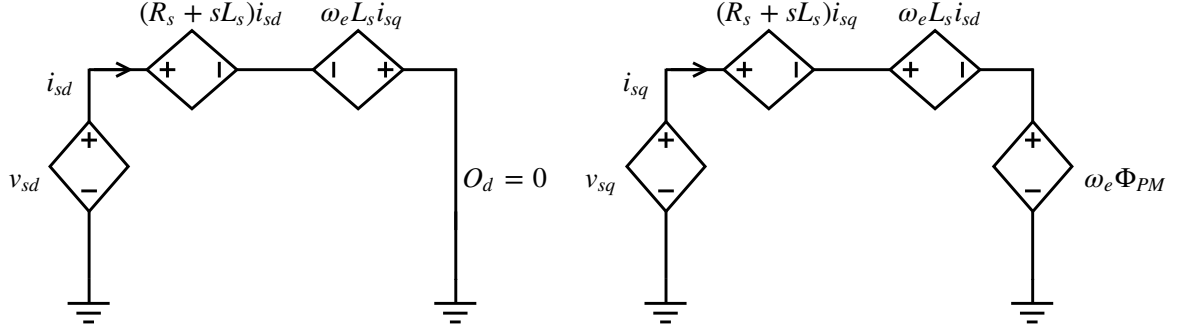


**Figure 3.13:** Equivalent Circuit for SG in the dq frame

### 3.4.5 Synchronous Generator Control

In the next few sections, a control strategy for the two converters connected to the SG will be carried out. The converter directly connected to the SG is denoted the Generator Side Converter (GSC), while the converter connected to the system is called the System Side Converter (SSC). A DC-link with capacitor separates the two converters. This capacitor decouples the two converters, making independent converter control possible. It should be mentioned that protection circuits such as snubbers and crowbars are neglected in this analysis. There are multiple control strategies applicable for both the GSC and the SSC [32]. For the GSC, active power, generator speed or DC-link voltage can be controlled by the q-component, while generator reactive power or stator voltage can be controlled through the d-component. For the SSC, DC-link voltage or active power can be controlled by the d-component, while the reactive power flow to the grid is usually governed through the q-component. Here, the following controller strategies have been chosen:

- ❖ GSC: The rotational speed is controlled through the q-component and the generator reactive power through the d-component.
- ❖ SSC: The d-component governs DC-link voltage, and the q-component controls the reactive power flow to the rest of the system.

### 3.4.6 Control of Generator Side Converter

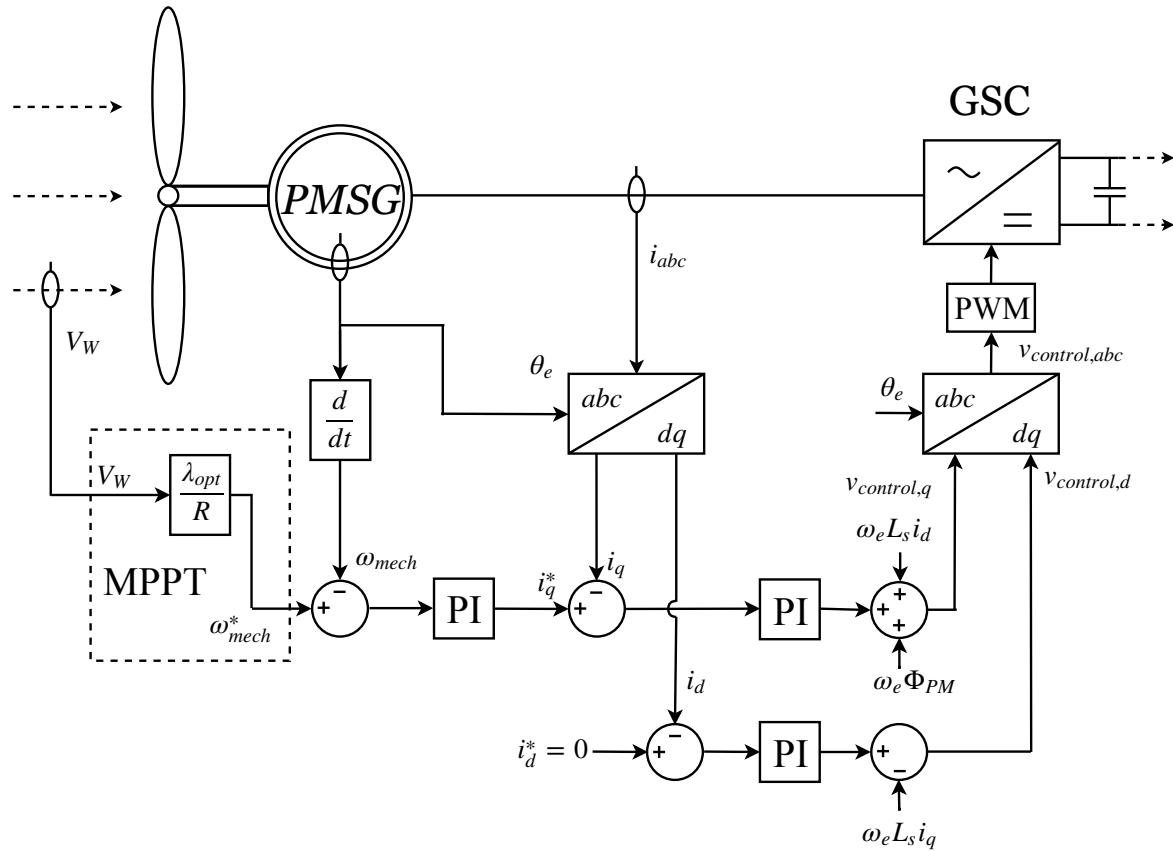


**Figure 3.14:** Grid Side Converter Control Overview

The main objective of the GSC is to extract as much power as possible from the wind. This principle is called Maximum Power Point Tracking (MPPT) and involves dynamically changing the rotor mechanical speed to extract maximum power for each wind speed, as explained in Section 3.4.1. This requires three variables to be known: The optimal tip-speed ratio, the wind speed and the rotor speed. The optimal tip-speed ratio,  $\lambda_{opt}$  can be found from the  $C_p$ - $\lambda$  curve, and the rotor speed is a relatively easy task to measure. However, in practice the wind speed is hard to measure, so sensorless estimators are often used instead [36]. Therefore, a key assumption here is that the wind speed estimation is assumed perfect, implying that it is equivalent to measuring the wind speed.

The block diagram for the GSC is shown in Figure 3.14 and the control method can be explained as follows: The MPPT controller calculates the optimal rotor speed for the measured wind speed, from the relationship  $\omega_{mech}^* = \lambda_{opt} \cdot \frac{V_W}{R}$ . This is compared with the actual speed of the turbine shaft, and the deviation is fed through a PI controller to create a reference value for the  $q$ -component of the stator current. Recalling from equation (3.13) that regulating  $i_{sq}$  controls the electromagnetic torque of the turbine. Now the output of the MPPT controller is used as input for the  $q$ -component in the GSC current controller. The current controller measures the stator currents,  $i_{abc}$ , and the electrical phase angle  $\theta$ . The angle is used in the Park Transformation in order to ensure that the rotor flux is aligned with the  $d$ -axis. Then the stator currents are transformed

into their respective d- and q-components. The reference of the d-component is set to zero because this results in the minimum stator current and therefore to minimise the resistive losses in the stator [37]. The rest of the current controller follows the procedure explained in Section 3.3, with the expressions for  $M_{dq}$ ,  $N_{dq}$  and  $O_{dq}$  from equation (3.15) inserted. In this way, the output voltages of the controller can be transformed into  $abc$ -quantities and thus be used as control voltages in the PWM scheme of the converter.

### 3.4.7 Control of System Side Converter

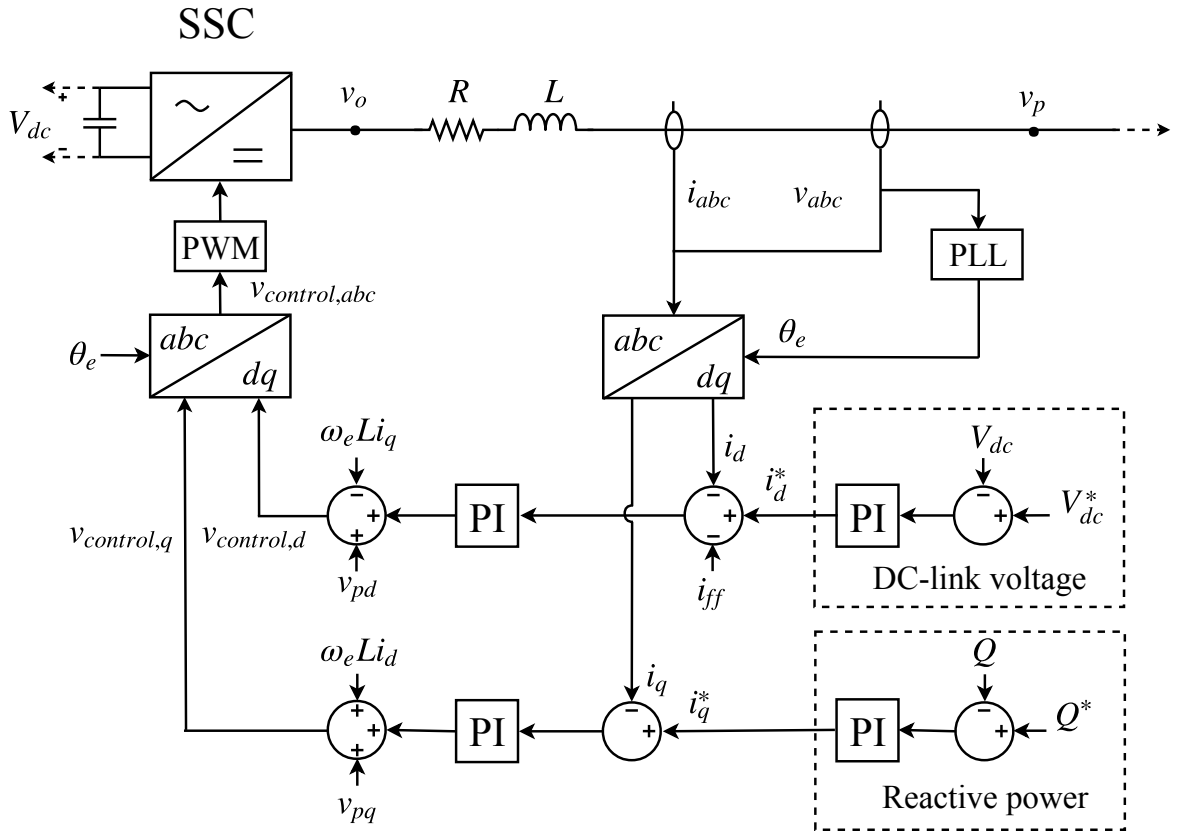


**Figure 3.15:** System Side Converter Control Overview

There are two main control objectives for the SSC, namely to control the voltage in the DC-link and the reactive power exchanged with the rest of the system. A complete block diagram of the SSC control is depicted in Figure 3.15. From this figure it is seen that a RL-filter is included between the converter output and the Point of Common Coupling (PCC). The purpose of this is to filter out the high-order harmonics produced by the VSC. Sometimes the transformer can provide sufficient filtering alone, but the author has chosen to include the RL-filter either way [38]. Applying KVL on the RL-circuit, and reorganising the equations to fit the generic form in Section 3.3, gives the following model of the converter interaction with the rest of the system:

$$\begin{aligned} v_{od} &= \underbrace{(R + sL)}_{M_d(s)} i_{od} - \underbrace{\omega_e L}_{N_d} i_{oq} + \underbrace{v_{pd}}_{O_d} \\ v_{oq} &= \underbrace{(R + sL)}_{M_q(s)} i_{oq} + \underbrace{\omega_e L}_{N_q} i_{od} + \underbrace{v_{pq}}_{O_q} \end{aligned} \quad (3.16)$$

Here,  $v_{o,dq}$  is the voltage at the converter output,  $v_{p,dq}$  the voltage at point and  $i_{o,dq}$  is the current out of the SSC.  $R$  and  $L$  is the filter's resistance and inductance respectively. The electrical equivalent of equation (3.16) is illustrated in Figure 3.16.

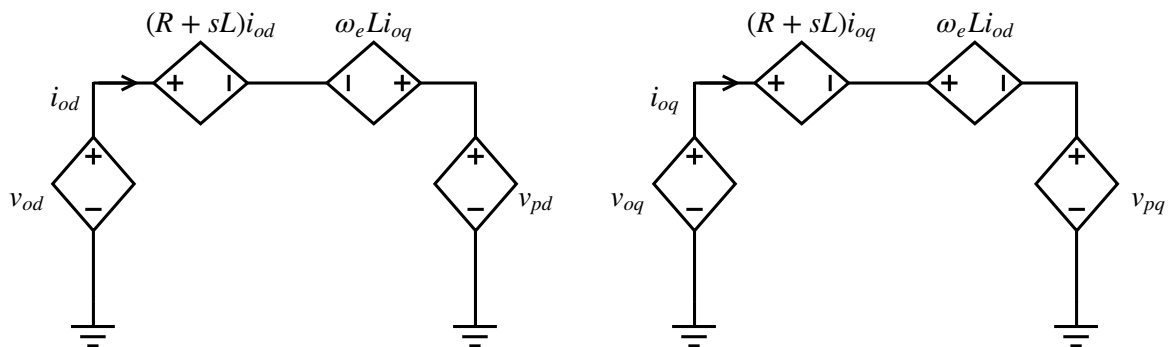


**Figure 3.16:** Equivalent Circuit for SSC in the dq frame

Another key point in the SSC control is the Phase Locked Loop (PLL). This is a simple control structure which provides the Park Transformation with the desired transformation angle,  $\theta$ . It takes the line voltages as input and produces  $\theta$  as output. Normally the PLL is designed such that the  $dq$ -frame is phase-locked with phase  $a$  of the line voltage at point P. This results in  $v_{pq} = 0$  and  $v_{oq} = v_a$ . Put in other words, the PLL facilitates synchronisation of the  $abc$ - and the  $dq$ -frame in the desired manner.

#### 3.4.7.1 Control of DC-link Voltage

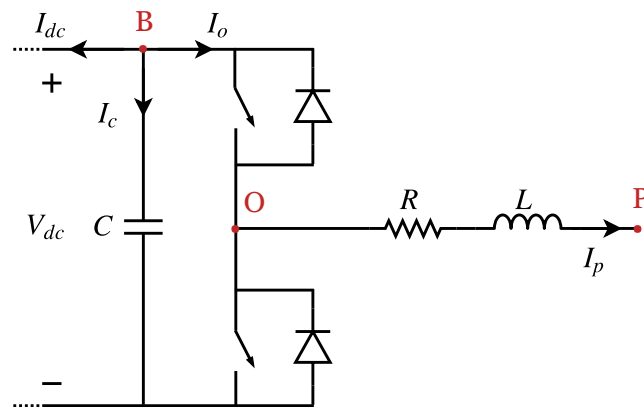


**Figure 3.17:** Per-unit Equivalent of VSC

The mathematical expressions leading to the DC-link voltage control are shown in this section. They are based on [17] and [39], however, they are modified to a per-unit equivalent. During the derivation, it should be noticed that different domains are used to present it in a pedagogical manner. Lowercase letters indicate variables in the time domain - except from DC quantities, whereas uppercase letters are used for phasors and variables in the Laplace domain. It will be clearly stated what is used where to avoid confusion. The per-unit circuit equivalent of the SSC is shown in Figure 3.17. The red letters B, O and P indicates fictional points. Based on this figure, the following mathematical relations are established in the phasor domain:

$$S_p = V_{p,dq} I_{p,dq}^* = (V_{pd} + j \underbrace{V_{pq}}_{=0}) (I_{pd} + j I_{pq})^* = V_{pd} I_{pd} - j (V_{pd} I_{pq}) \quad (3.17)$$

Please note that the superscript '\*' represents the complex conjugate in equation (3.17) and not the reference value. Hence,

$$\begin{aligned} P_p &= \text{Re}\{S_p\} = V_{pd} I_{pd} \\ Q_p &= \text{Im}\{S_p\} = -V_{pd} I_{pq} \end{aligned} \quad (3.18)$$

Further Kirchhoff's Current Law (KCL) can be applied to the point B in Figure 3.17, giving:

$$I_o + I_c + I_{dc} = 0 \quad (3.19)$$

Assuming that the voltage drop across the filter resistance  $R$  is negligible implies that the active power from point O to the system can be treated as equal to the power from point P to the grid, thus  $P_o \approx P_p$ . Further, the DC power and the capacitor power is governed by:

$$\begin{aligned} P_{dc} &= V_{dc} \cdot I_{dc} \\ P_c &= V_{dc} \cdot I_c \end{aligned} \quad (3.20)$$

Multiplying equation (3.19) with the respective voltages yields the power balance of  $p_p + p_c + p_{dc} = 0$ . Thus, using that in the time domain  $i_c = C \cdot \frac{dV_{dc}}{dt}$  and inserting the expressions deducted above results in:

$$v_{pd} i_{pd} + V_{dc} \cdot C \frac{dV_{dc}}{dt} + I_{dc} V_{dc} = 0 \quad (3.21)$$

It is possible to make a linearisation of this expression by means of Taylor series expansion, and further transform it into the Laplace domain [39]:

$$V_{dc}(s) = \frac{1}{sC} \cdot \frac{v_{pd}}{V_{dc}^*} \cdot i_{pd} \quad (3.22)$$

The purpose of deducting these mathematical expressions is to show that control of active power and the DC-link voltage correlates with  $i_{pd}$ , while the reactive power correlates with  $i_{pq}$ . This is also seen from the control structure in Figure 3.15, where the difference between  $V_{dc}^*$  and  $V_{dc}$  is fed through a PI controller to produce the reference

current in the  $d$ -axis. Another term that should be noted is  $I_{ff}$ . This is subtracted from the usual reference current to compensate for possible slow dynamics in the cascaded control. According to [39], including a feed-forward term can reduce load variation and also reduce the gain of the voltage controller, which is desirable from a stability point of view. The value of the compensating term is calculated through the assumption of balanced conditions, meaning  $I_c = 0$  and  $I_{pd} = I_{dc}$ . Hence,  $I_{ff} = \frac{V_{dc}}{v_{pd}} I_{dc}$ , and subtracting this from the PI controller output produces the appropriate reference current  $i_{pd}^*$ .

### 3.4.7.2 Control of Reactive Power

One of the main advantages of an EESG is the property of regulating reactive power. However, in a PMSG the rotor flux is constant, making the reactive power regulation less flexible. Despite this, using a synchronous generator instead of a reactive power consuming induction generator may eliminate the need for additional and expensive reactive components, such as STATCOMs and SVCs. In strong grids, dynamic control of reactive power in the SSC is not required in most cases as these systems often have large reserves of reactive power compensating units. However, in a small and autonomous system like the one assessed here, reactive power control becomes a necessity for system stability.

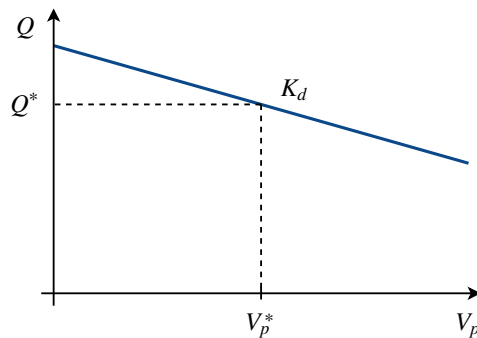


**Figure 3.18:** Typical Voltage-Droop Curve

There are multiple ways of implement the reactive power controller, and the strategy must be chosen carefully as there may be several reactive sources operating in parallel. The synchronous generator in the Diesel Generator is equipped with an Automatic Voltage Regulator (AVR). This adjusts the reactive power in the machine through regulating the magnetisation of the rotor circuit. However, the diesel generator does not run continuously, so the SSC requires reactive power control. Additionally, the AVR has a considerably slower response than the VSCs due to the time delay linked to regulating the field winding. This is the main motivation behind implementing reactive power control in the SSC.

The control scheme depicted in Figure 3.16 may be improved by including a voltage-droop branch in the reactive power control. Voltage-droop involves changing the reactive power based on deviations in the system voltage [40]. A plot showing a typical voltage-droop characteristic is illustrated in Figure 3.18. The slope of the curve is

denoted  $K_d$ . The main advantage with this simple mechanism is that during low voltage periods, the reactive power drawn from the SSC increases and vice versa in high voltage situations. This may reduce the voltage fluctuations which is desirable from a weak power system perspective. However, for the purpose of this work, the voltage droop mechanism have been omitted.

### 3.5 The Battery Energy Storing System

The battery energy storage system (BESS) plays a major role in the hybrid system. As wind is an unpredictable source of power, solely using Wind-Diesel without an energy storage device will lead to a lower renewable penetration than with an energy storage. This is because the diesel generators have to run more frequently in this situation, due to the increased risk of inadequate generated power. Incorporating a BESS enables the opportunity of smoothing the short-term fluctuations in wind energy as well as long-term variations in the load. This results in better utilisation of the available wind resources [41].

Activated by the increased focus on renewable energy, the battery industry is going through a rapid development, leading to continuously cheaper and better batteries. Multiple technologies are available on the market, and all have their specific strengths and weaknesses. The capacities range from kWhs to MWhs, while their discharge time varies from seconds to several hours. Other notable features are the desired depth of discharge (DoD)<sup>5</sup>, voltage level and maintenance frequency. Together, these factors affect the lifetime of the diesel engines. Starting and stopping the engines too frequent causes increased wear and tear, and eventually a shorter operational lifetime before needing maintenance.

A BESS is not only a battery; it is a composite system consisting of several other components as well, including cooling, monitoring and control solutions, DC switch, AC breaker and usually a power converter. A battery stores and delivers DC current, while the wind turbine and the loads are connected to an AC bus. Therefore a switch-mode power converter must be included. Section 3.5.3 covers the control of this converter.

A substantial part of the former specialisation project [10] dealt with a comparison between different battery technologies. The most important criteria for the proposed fish farm were defined as:

- ❖ The system is placed in a fragile, maritime environment. Thus, the battery should either contain a small amount of toxic components or have a safety system preventing a potential effluent to the surroundings.
- ❖ The remote location makes transportation complex and costly, as it most likely will have to be transported by ship. Hence, a long battery cycle life is desirable.

---

<sup>5</sup>DoD describes the fraction of energy which can be drawn from the battery. It is expressed as a percentage of the nominal battery capacity. The larger the DoD, the shorter the cycle life [42].

- ❖ As the temperatures at the location may vary between  $-20^{\circ}\text{C}$  and  $+30^{\circ}\text{C}$ , the battery must be able to withstand these temperature changes. If not, it must come with a cooling/heating system.
- ❖ Superior reliability and low maintenance should be a priority because of the defiant accessibility.
- ❖ Off-grid hybrid systems are typically subject to highly variable charging powers, deep cycling, partial cycling and infrequent full charge [43], [44]. Thus, the appropriate battery has to endure these challenges.

There are several battery technologies commercially available today; from the traditional Lead-Acid, Sodium-Sulphur (NaS) and Nickel Cadmium (NiCd) to more modern and advanced technologies as Lithium-ion (Li-ion), Nickel Metal Hydride (NiMH), Flow and Advanced Lead-Acid. Investigation of the dynamics in all of these technologies has been found too time-consuming to be covered in this work. Therefore, the author has made a choice of assessing the dynamics of a special type of Li-ion battery, namely the Lithium Iron Phosphate (LFP) battery. This decision is based on several factors: Firstly, LFP has shown very promising response related to power performance and voltage stability during cycling. Also, partial cycling and pulse charging seems to have a minuscule impact on the degradation on Li-ion batteries in general [43]. Among the Li-ion batteries, LFP is considered the safest technology due to high thermal runaway temperature [45]. Secondly, one of the main results from the specialisation project showed that the diesel fuel consumption could be reduced by around 85 % solely by integrating a wind turbine to the system. This implies that a large and expensive battery may not be needed. Thus, choosing a Li-ion battery which has higher investment cost than conventional battery technologies, e.g. Lead-Acid, actually may be a better economical solution in the long run.

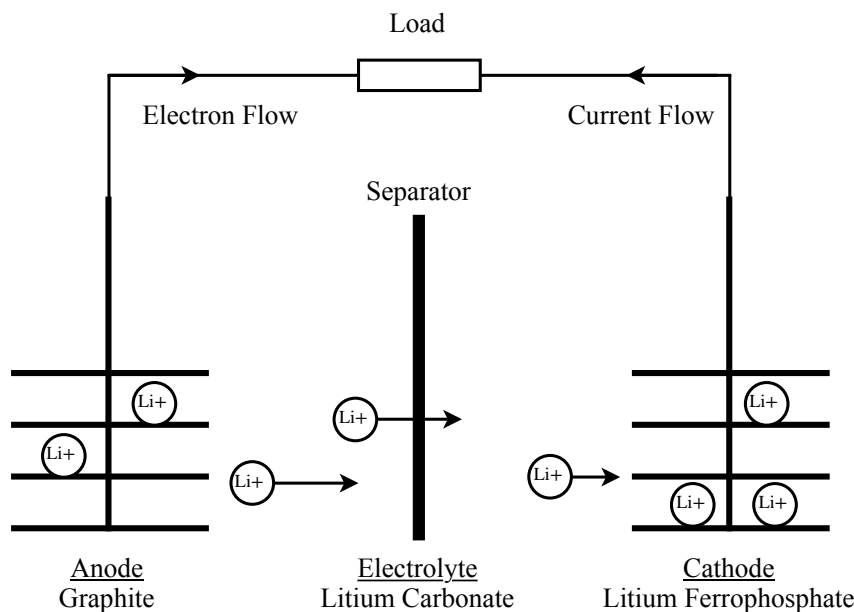


**Figure 3.19:** Principle of a LFP Battery During Discharge



### 3.5.1 Lithium-ion Batteries

Lithium-ion batteries have been widely used in consumer electronics for the last couple of decades [46]. Now, due to extensive research and reduced cost, this technology is also becoming cost-effective in larger systems [47]. There are multiple compositions of Li-ion batteries, which all have different characteristics. Their nominal voltage may vary from approximately 2.4-4 V depending on the chemistry. Similar for all is that during charging lithium ions flows from the positive cathode and to the negative anode. Figure 3.19 is inspired by [48] and illustrates a simplified schematic of a single LFP cell during discharge. Examples of different Li-ion technologies and some of their features are shown in Table 3.3, based on [42].

**Table 3.3:** Lithium-ion Battery Types

Name	Cathode material	Anode material	Electrolyte	Energy density [Wh/kg]
Lithium Iron Phosphate	Lithium Ferrophosphate (LFP)	Graphite	Lithium Carbonate	200-2000
Lithium Manganese Spinel	Lithium Manganese Dioxide (LMO)	Graphite	Lithium Carbonate	800-2000
Lithium Titanate	Lithium Manganese Dioxide (LMO)	Lithium Titanate	Lithium Carbonate	2000-25000
Lithium Cobalt Oxide	Lithium Cobalt Oxide (LCO)	Graphite	Lithium Polymer	300-800
Lithium Nickel Cobalt Aluminium	Nickel Cobalt Aluminium (NCA)	Graphite	Lithium Carbonate	800-5000
Lithium Nickel Manganese Cobalt	Nickel Manganese Cobalt (NMC)	Graphite and Silicone	Lithium Carbonate	800-2000

From this table it is observed that almost all the chemistries use graphite as anode material, while the cathode material varies. There are many different types to choose between, but the technology is still relatively young, hence, there is still a lack of knowledge considering long-term performance in hybrid systems. Regardless of the chemistry, Li-ion batteries have many features that makes them attractive for hybrid system applications:

- ❖ They have high energy and power density, which means that they use less physical space than other batteries.
- ❖ Charging and discharging ratings are relatively high, making it capable of covering large load fluctuations.
- ❖ They are practically maintenance-free.
- ❖ They have excellent charging and discharging efficiency (80% to almost 100% [42],[49], even at very high DoD.
- ❖ They can handle the stress connected to infrequent full charging, without suffering from significant degradation [43].
- ❖ They have relatively long cycle life even at high DoD (around 3000 cycles at 80% DoD [49]).

Even though Li-ion batteries appear as well-suited for Hybrid Wind-Diesel Systems, there are some challenges to overcome. High investment cost compared to other solutions is still a barrier. However, the price is continuously decreasing, leading to increased deployment all over the world. High investment cost may also compensate for no maintenance cost, long lifespan and high energy density. Another obstacle concerns safety. Li-ion batteries require sophisticated monitoring and control, to avoid over-charging/over-discharging [50]. If this is not handled properly, internal heat may develop, and in the worst case scenario a thermal runaway can occur, leading to fire and total damage of the system.

#### 3.5.2 Lithium Iron Phosphate Model

In this section, the underlying assumptions and considerations when implementing a model of the LFP battery are elaborated. When a battery is charged or discharged, the terminal voltage of the battery varies with the State of Charge (SOC) through a nonlinear relationship, as illustrated in Figure 3.20. SOC is another central battery concept which describes the energy stored in or depleted from the battery at a given time. The SOC unit is typically [%] or [Ah]. It can be seen that the voltage decays with the depletion of the battery. Additionally, the voltage increases rapidly when it is close to full. This is called the exponential area [51]. One of the key points in the dynamic model is to include this nonlinearity in order to reflect a realistic battery behaviour.

Modelling of Li-ion batteries can be divided into three broad categories: electrochemical, mathematical, and electrical [52]. The electrochemical models are highly complex and accurate, but involves solving large systems with partial differential equations, which is time-consuming. These models are mainly used to optimise the physical design of batteries. The mathematical models are based on empiric or stochastic relationships. These are significantly less complex than the electrochemical models, and therefore lacks some realism. Nevertheless, they can prove to be sufficient in some analyses. The main problem with mathematical models is that they cannot incorporate

the nonlinear relationship between SOC and terminal voltage. So instead, an electrical model with complexity that lies between the two aforementioned, can be applied [53]. These kinds of models use a combination of a controllable voltage source in series with resistors and capacitors connected in parallel branches. There are several possible ways to implement the electric battery model. In [54] and [55] detailed electric modes are used, which takes into considerations the effect of temperature and capacity fade. Here the electric equivalent is a controllable voltage source in series with a single resistance and two parallel branches with resistance and capacitor. However, this is unnecessarily complex and the parameter values are tricky to conduct without experimental or manufacturer data.

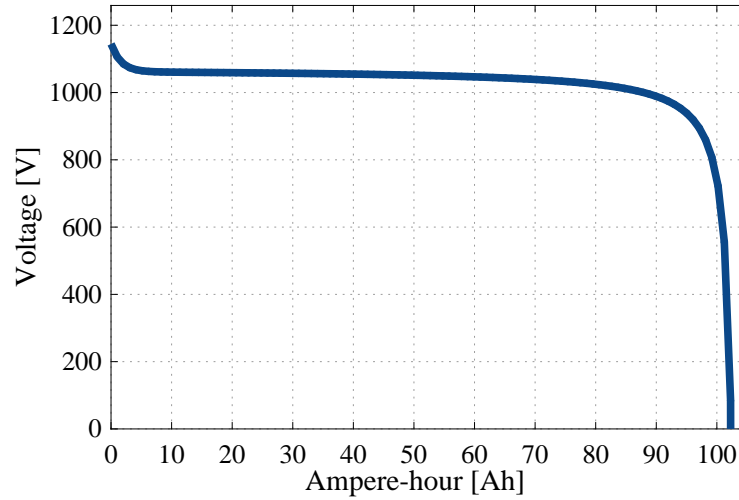


**Figure 3.20:** Battery Voltage vs Depleted Energy at 50 A Discharge Current

Therefore, a more direct approach is chosen here. The model is based on the workings in [56] and [57], and neglects the parallel RC-branches. Instead the battery open-circuit voltage,  $V_{OC}$ , is calculated as a function of the SOC and the battery current filtered through a low-pass filter. The equations describing  $V_{OC}$  during charge and discharge are given in (3.23) and (3.24). Further, a summary of the variable names are shown in Table 3.4. Appendix E includes a derivation and a more thorough explanation of the parameters of equations (3.23) and (3.24). Note that  $i_{fi}$  is defined as  $> 0$  during discharge and negative during charge.

$$V_{oc}^{di} = E_0 - \rho \cdot \left( \frac{\xi_{max}}{\xi_{max} - \xi} \right) \cdot \xi - \rho \cdot \left( \frac{\xi_{max}}{\xi_{max} - \xi} \right) \cdot i_{fi} + \mu_v \cdot e^{-\mu_c \cdot \xi} \quad (3.23)$$

$$V_{oc}^{ch} = E_0 - \rho \cdot \left( \frac{\xi_{max}}{\xi_{max} - \xi} \right) \cdot \xi - \rho \cdot \left( \frac{\xi_{max}}{\xi - 0.1\xi_{max}} \right) \cdot i_{fi} + \mu_v \cdot e^{-\mu_c \cdot \xi} \quad (3.24)$$

**Table 3.4:** Overview of Battery Variables and Parameters

$V_{oc}^{di}$	Open-circuit Voltage at Discharge	$\xi_{max}$	Battery Capacity
$V_{oc}^{ch}$	Open-circuit Voltage at Charge	$\xi$	Available Capacity
$E_0$	Constant Voltage	$\mu_v$	Exponential Voltage
$\rho$	Polarisation Constant	$\mu_c$	Exponential Capacity
$i_{fi}$	Filtered Battery Current		

### 3.5.3 Battery Control

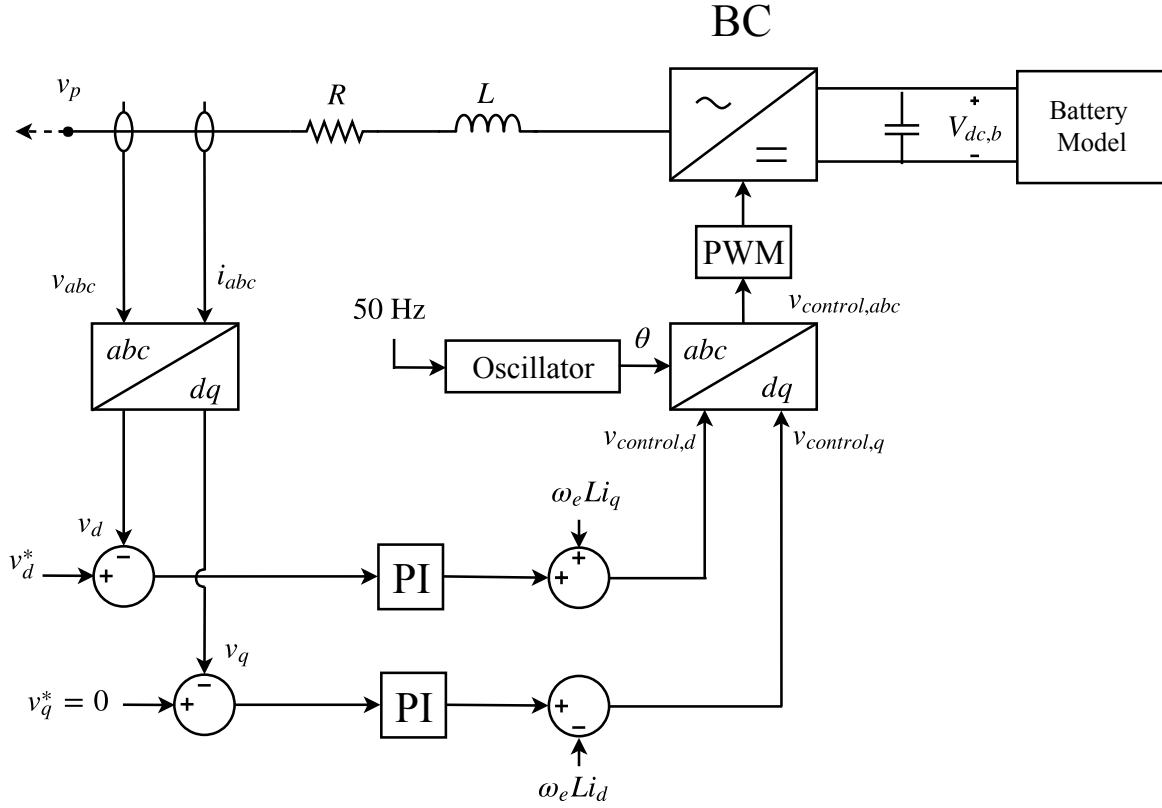


**Figure 3.21:** Battery Converter Control

The battery stores and delivers DC current and voltage, while the rest of the hybrid system runs on AC. Therefore a bi-directional power electronic converter is needed between the battery and the AC bus bar. The main purpose of the Battery Controller (BC) is to provide AC voltage and frequency support for the system. As no frequency controller has been implemented in the wind turbine system, this feature of the BC is inevitable for acquiring system stability whenever the turbine and battery are supplying the load alone.

There are several possible ways of implementing the BC. [58] and [59] uses cascaded control, similar to the ones in the GSC and SSC. However, a simple, yet very effective control structure is found in [60] and is implemented here. Figure 3.21 presents the structure for the converter control. It is evident that the voltage controller is analogous to the inner current controller of the GSC and SSC. The line voltages and currents are measured at the PCC and then converted to the dq-frame. The reference of  $v_d^*$  is set to 1.732 ( $\sim \sqrt{3}$ ) pu because the line voltage is  $\sqrt{3}$  times the phase voltage, and the reference of  $v_q^*$  is zero. The errors are fed through a PI controller (tuned in Appendix D.7). Then the cross-coupling terms are added/subtracted before the signals are transformed into pulses for the PWM scheme. As opposed to the structure of the SSC, no PLL is present in the BC. Instead, an internal oscillator with a constant frequency of 50 Hz, provides the abc/dq transformation with an angle. This constitutes the BC frequency support.

### 3.6 Diesel Generator System

The diesel aggregates in a hybrid system normally consist of diesel engines connected to synchronous generators through an electromechanical clutch. The whole aggregate is often referred to as a Diesel Generator (DG). The clutch is assumed to be either engaged or disengaged, depending on whether the aggregate should produce electrical power or not. When the clutch is engaged, the mechanical shaft of the engine and the alternator's rotor are mechanically coupled and rotates with the same speed.

On the engine side of the DG, there is a speed governor which regulates the fuel inlet to the motor through a comparison between a reference speed and the real mechanical speed. In this way, the speed and active power from the engine can be controlled. On the generator side, a voltage regulator controls the output voltage and reactive power, through adjustment of the rotor circuit excitation. A schematic of the diesel generator set is shown in Figure 3.22 and the specific modelling of the diesel engine and synchronous motor are explained in the next sections.

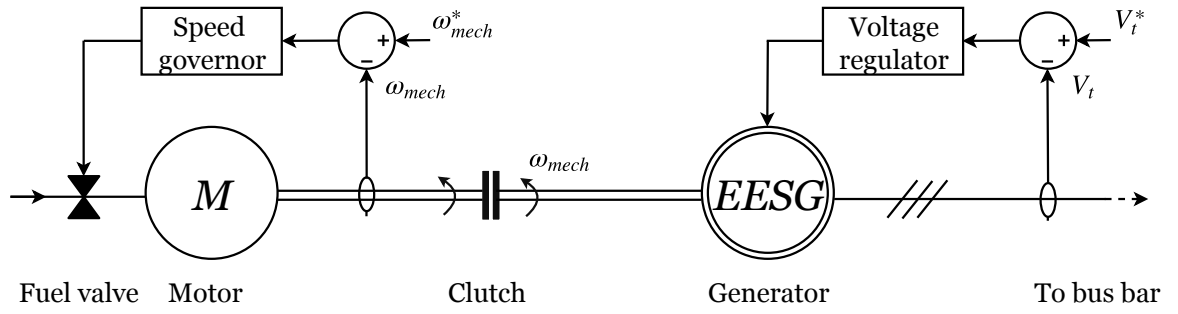


**Figure 3.22:** Diesel Generator Schematic

One challenge linked to diesel generators is that the machine efficiency drops drastically if run at lower than  $\sim 30\%$  of nominal power [61]. Therefore, it is often desirable to use several diesel aggregates with different power ratings in parallel. E.g. at low load a small generator can operate at decent efficiency instead of a large generator serving the load at a very low efficiency.

#### 3.6.1 Diesel Engine Model

The diesel engine model comprises of three main parts: A speed governor controller, engine dynamical physics and a mechanical system. Several studies report on the physical dynamics of diesel engines. Thus, choosing a model with appropriate complexity is a challenge. The PhD thesis in [62] uses a rather detailed representation, where a turbocharger model, a mechanical model and inter-cyclic torque variations are included. In [63], [64] and [65] the engine's transfer function is described by a first order time constant and a time delay, which represents the time elapsed from fuel injection to the new torque is established in all the cylinders. However, for the purpose of this thesis, another approach is proposed: The diesel engine mechanical model is incorporated in

the speed governor control. The motor is thus assumed to be stiffly coupled to the generator at any time. In other words, a key assumption is that the clutch is always engaged. This implies that the motor inertia is included in the synchronous generator model, while the speed governor control reflects the most relevant features of the engine from an electrical point of view.

### 3.6.2 Speed Governor Control

Diesel engine governor control plays a crucial role in the hybrid system, as it is responsible for the frequency and balance of active power whenever the DG have to run. The link between the governor and the physical engine can be described as follows: The deviation in measured mechanical speed from the reference speed is intercepted by a controller, called the speed governor. Based on the deviation, the governor sends a signal to a regulating valve - called the actuator - which adjusts the fuel flow rate of the engine. Depending on this, the developed motor torque will change accordingly after a certain time, determined by the time interval between cylinder firings. These are usually either mechanical or electromechanical components that act as valves. Typical governors are found in [66], [67]. In the workings of [68] and [69] the speed controller is modelled as a second order system and the actuator by a third order transfer function. This is the proposed control implementation for this thesis. A complete block diagram which describes this is shown in Figure 3.23.

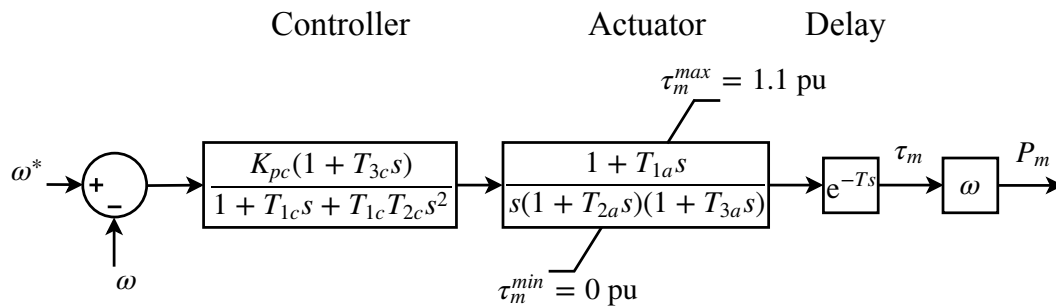


**Figure 3.23:** Diesel Engine Speed Governor Control

### 3.6.3 Synchronous Generator Model

In Section 3.4.4 some of the properties of a PMSG was elaborated. However, the section focused on the mathematical expressions relevant from a control point of view, rather than explaining the physical behaviour of a synchronous generator. Therefore, this section will cover a summary of synchronous machine theory. Synchronous machines (SMs) are common components in an electric power system. There are an abundance of papers and books explaining their working principles, varying from a system perspective to a very detailed electromagnetic level. See for example [70], [71] and [18]. In order to limit the theoretical part, only some of SM's features will be discussed in this section, as they facilitate relevant observations and findings related to Chapter 4 and 5.

Synchronous machines can operate in both generator and motor mode, depending on the applied torque's direction relative to the induced torque. In this thesis, only generator operation will be covered because this is relevant to the system under consideration, but some of the topics apply for both generator and motor operation.

The principle of a synchronous generator (SG) is to exploit an external mechanical torque on the rotor shaft to induce an electric voltage with a desired frequency in the stator. A DC current is applied to the rotor field circuit, and this produces a rotating magnetic field of  $\omega_m$  radians per second. The rotating magnetic field induces a voltage (emf) in the stator windings according to Faraday's Law [70]:

$$e_{ind} = (\vec{v} \times \vec{B}) \cdot \vec{l} \quad (3.25)$$

Here,  $\vec{v}$  is a vector describing the *relative* velocity between the stator winding and the flux density  $\vec{B}$ , and  $l$  is the effective length of the rotor field as seen from the stator. Further the length of  $\vec{v}$  is often expressed as  $v = \omega_m \cdot r$ , with  $r$  denoting the rotor radius. It should be noted that the synchronous machines discussed in this thesis are treated as round rotor types. This is a reasonable assumption as high-speed SMs - as the one discussed here - tend to have 2-4 poles in a cylindrical formation, as opposed to e.g. slow-rotating hydro turbines, which have salient pole rotors.

The stator windings can be connected to a load, so that a current may flow through them. In this way, the stator produces a magnetic field as well. Thus, in a SM two magnetic fields interact - one from the stator and one from the rotor. The interaction between these two fields, induces an electromagnetic torque given by equation (3.26).

$$\tau_{ind} = k \cdot (\vec{B}_R \times \vec{B}_S) = k \cdot B_R \cdot B_S \cdot \sin \delta \quad (3.26)$$

where  $\vec{B}_R$  is the rotor field,  $\vec{B}_S$  the stator field,  $k$  a machine constant and  $\delta$  represents the angle between the two fields. This is often called the *torque angle*. If the induced torque rotates in the same direction as the applied torque on the rotor shaft, then the machine is in motor operation. The opposite is the case if they rotate in different directions. One of the main features of a SM is that the electrical frequency of the machine is synchronised with the rotor's rotational speed [70]. Thus, for a given number of poles and a fixed frequency, the rotational speed will also be fixed.

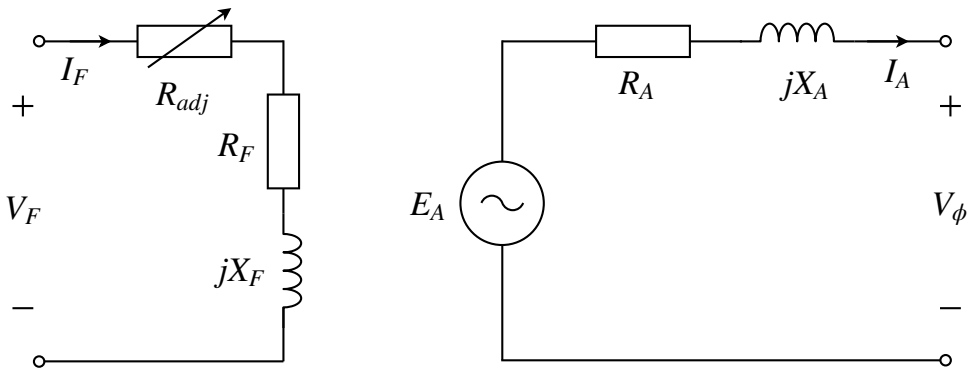


**Figure 3.24:** Per-phase SM Equivalent

The synchronous generator connected to the diesel engine differs from the wind turbine PMSG in the way that this is electrically excited. This implies that magnetisation of the field winding is adjustable, by varying the field current  $I_F$ . Increasing  $I_F$  leads to an increase in flux,  $\phi$ , produced by the rotor circuit, through a linear relationship as long as saturation is neglected. Saturation implies that there is a finite maximum value of the flux present in a given material. Thus, at some point increasing  $I_F$  will not lead to a proportional increase in flux. Figure 3.24 illustrates the per-phase equivalent of a SM with round rotor [70]. Here,  $E_A$  is the induced voltage in a given stator phase,  $R_{adj}$  an adjustable resistance representing variable field current,  $R_F + jX_F$  field winding impedance and  $R_A + jX_A$  the stator/armature winding resistance. The internal voltage relates to the air gap flux through equation (3.27).

$$E_A = K_A \cdot \phi \cdot \omega \quad (3.27)$$

with,  $K_A$  a machine constant. The main observation from equation (3.27) is that  $E_A \propto \phi$ , and  $\phi \propto I_F \implies E_A \propto I_F$  in the unsaturated region. Furthermore, KVL on the circuit in Figure 3.24 gives

$$E_A = I_A \cdot (R_s + jX_s) + V_\phi \quad (3.28)$$

$I_A$  is the phase current,  $R_s + jX_s$  the generator total internal impedance and  $V_\phi$  the phase voltage. If the generator is Y-coupled, then the terminal voltage of the generator,  $V_T = \sqrt{3}V_\phi$ .

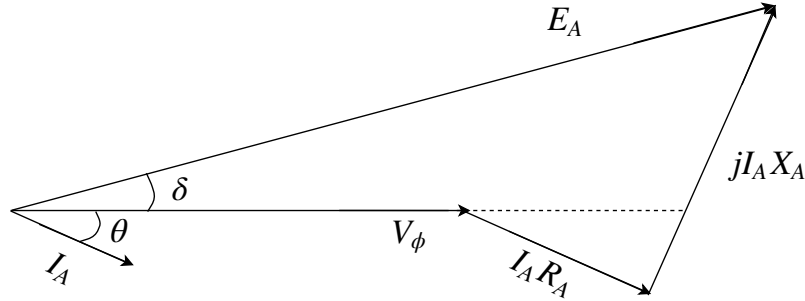


**Figure 3.25:** Phasor Diagram for Lagging Load

When the generator is connected to a lagging load, then  $I_A$  will lag  $V_\phi$ . This means that the magnitude of  $E_A$  has to be larger than  $V_\phi$  as there will be a resistive and inductive voltage drop across the generator impedance. The phasor diagram in Figure 3.25 illustrates this. An interesting case occurs when the generator load is increased with constant power factor. It is assumed that the load increases swiftly, hence the field current and  $E_A$  can be treated as fixed, due to the time delays associated with the excitation regulator. This is typically around 1 second [17]. Further,  $\omega$  is assumed constant. So, when the load increases the magnitude of  $I_A$  increases as well, but the phase angle between  $I_A$  and  $V_\phi$  remains the same. This means that if  $E_A$  is constant, and  $I_A$  increases, then  $V_\phi$  decreases because of  $|E_A| = \sqrt{V_\phi^2 + (R_s + X_s)^2 I_A^2}$ . So increasing a lagging load, will lead to a temporary voltage dip at the generator terminals until the field excitation is increased accordingly.



The last property of a SM to be discussed is the swing equation. Whenever a synchronous machine is exposed to a sudden disturbance, a transient response of the machine will occur because there is a temporary mismatch between the mechanically applied torque and the electromagnetic torque. This results in an oscillatory lapse described by the swing equation [72]. It should be noted that a term with damping torque is neglected in this equation and that it is given in per-unit.

$$\frac{2H}{\omega_s} \cdot \frac{d^2\delta}{dt^2} = \tau_a = \tau_m - \tau_{ind} \quad (3.29)$$

Here,  $H$  [s] is the per unit inertia constant,  $\omega_s$  [rad/s] the synchronous rotational frequency,  $\delta$  [rad] the torque angle,  $\tau_a$  [Nm] the accelerating torque,  $\tau_m$  the mechanical torque and  $\tau_{ind}$  the electromagnetic torque. For generator operation, both  $\tau_m$  and  $\tau_{ind}$  are positive. Thus, if  $\tau_m > \tau_{ind} \implies \tau_a > 0$  and the machine will accelerate. The opposite is the case if  $\tau_m < \tau_{ind}$ . If the disturbance is small enough, the machine's oscillations will die out eventually and a new stable operating point will be established. This explains the oscillatory system behaviour to be discussed in Chapter 5.

### 3.6.4 Automatic Voltage Regulator

The block diagram for the simplified field excitation control is adapted from [73] and a pre-built Simulink block facilitating this control is used. An AC5A brushless pilot exciter, according to [74] and [73], is assumed to supply the generator's rotor field current. A short description of the workings of this exciter is given: In a pilot exciter, permanent magnets mounted on the generator rotor create a flux. When the rotor rotates, time-varying flux induces AC currents in a small armature circuit on the stator. The AC current is fed through a three-phase rectifier and a variable resistor. A DC exciter field is established and this induces AC current in another exciter armature circuit on the rotor. This is rectified again and the main rotor field is established [70]. By using this kind of exciter, brushes and slip rings are avoided, which reduces the maintenance significantly. A block diagram of the AVR is illustrated in Figure 3.26.

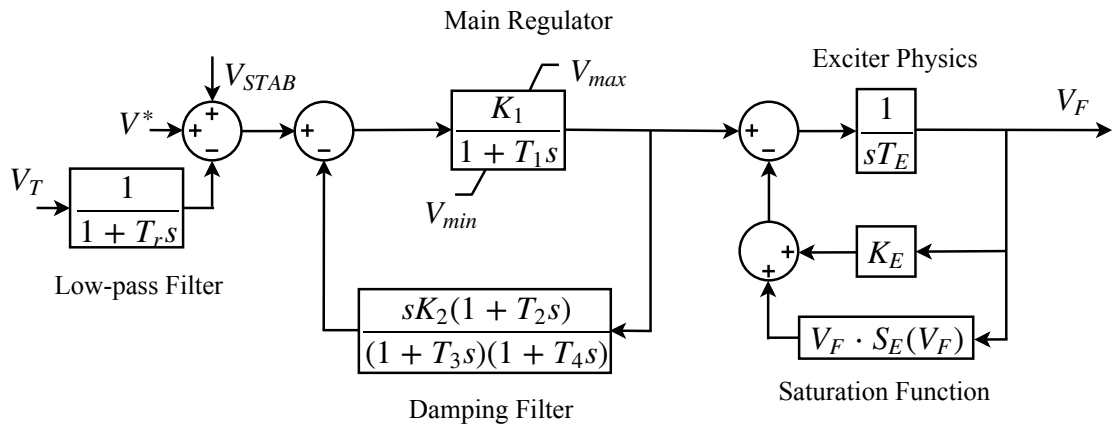


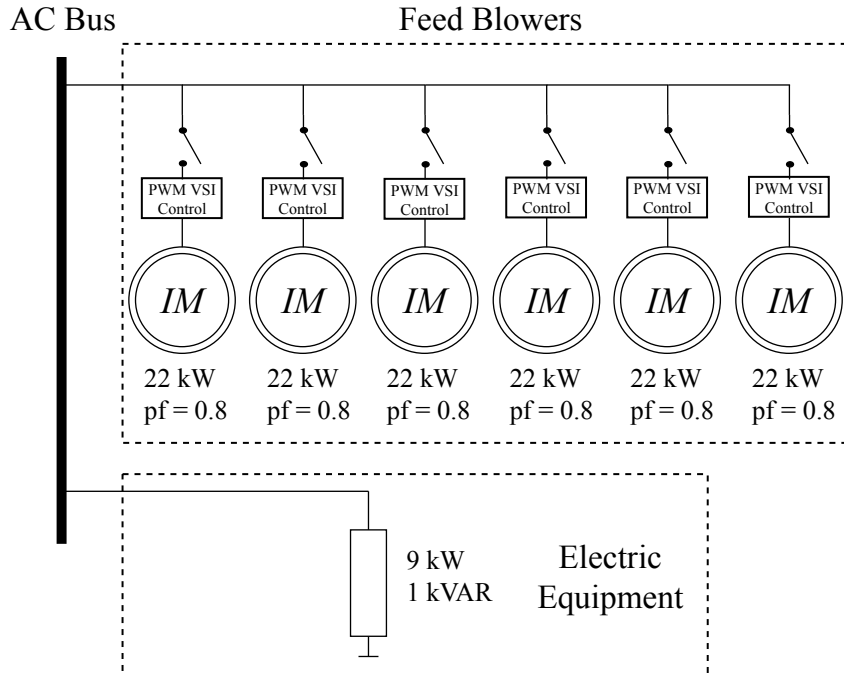
Figure 3.26: AC5A Exciter Block Diagram

**Table 3.5:** AC5A Parameters

$V_T$	Terminal Voltage	$K_2, T_{2-4}$	Damping Filter Constants
$V^*$	Reference Voltage	$K_E, T_E$	Exciter Constants
$V_{STAB}$	Stabilising Voltage	$V_F$	Field Voltage Applied to SG
$K_1, T_1$	Regulator Constants	$S_E(V_F)$	Exciter Saturation Function
$V_{min}, V_{max}$	Regulator Limits	$T_r$	Filter Time Constant

### 3.7 Main Load

The main load of the Hybrid Wind-Diesel System is the collection all energy consuming units needed for covering the core requirements of the system in a desirable manner. The units involved in the main load depends on the hybrid system's application. For usage in rural areas or islands, it may be a village or just a few houses. In the context of a fish farm application, the main load can involve the equipment on the feed barge used in the day-to-day operation. In specific, this includes the feed blowers and the power for running the electrical equipment on the barge, see Figure 3.27. The consumption profile of the barge was carried out in Section 2.2, however, a somewhat more technical description is required to understand the physical behaviour of the system. The main load is therefore divided into two parts: One covering the feed blowers and one describing the feed barge's own power demand.

**Figure 3.27:** Main Load Schematic

### 3.7.1 The Feed Blowers

There are to be six feed blowers situated on the fleet. These are in principal compressors driven by three-phase squirrel-cage induction motors (IMs) running at 400 V line voltage<sup>6</sup>. The IMs are variable speed controlled, which means that they connected to the AC bus bar through a circuit breaker and a power electronic converter. This converter differs from the battery and wind turbine VSCs because it is not bi-directional; Instead, it consists of a three-phase diode rectifier, a capacitor and one VSC connected to the IM terminals, which is seen from Figure 3.28. This configuration will be referred to as a Voltage Source Inverter, or VSI henceforth. It should be noted that the vector control used here is adopted from [75] and has not been made from scratch by the author. Nevertheless, the VSI's control objective is related to speed regulation of the IM. The decoupling effect of the DC-link is an advantageous property of this IM configuration compared to a directly-connected IM, because this will reduce the reactive power consumption during start-up considerably. The reason for this is because the reactive power is locally generated by the VSC and not imported from the grid. The simulations in Chapter 5 will confirm this benefit of variable-speed IMs, compared to fixed-speed IMs.

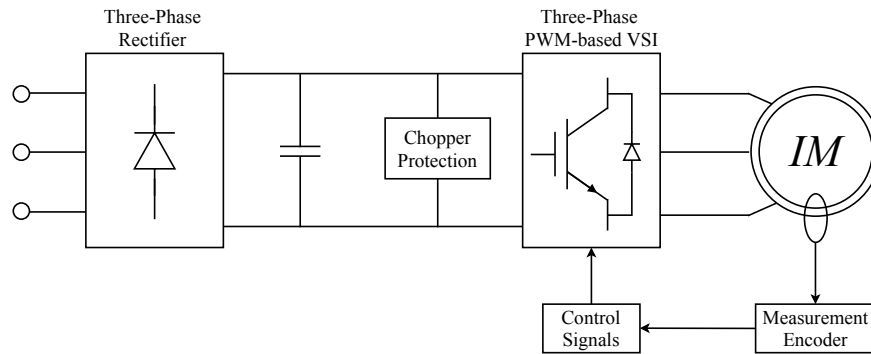


**Figure 3.28:** Variable Speed Induction Machine

Even though variable-speed IMs have smaller reactive power consumption during start-up, they will still draw high currents - up to several times more than 1 pu - in order to magnetise and speed up the machine. Several special-purpose IM starting circuits are available on the market, which aims to reduce the high start-up current, e.g. through reducing the line voltage [70]. However, direct on-line starting of the IMs will be used in the simulations, as it is the simplest and most economical solution.

Direct starting implies that a voltage dip may occur in the system unless it is accounted for [76]. In practice, capacitor banks can be applied in parallel to reduce this dip. Another option is to increase the system voltage slightly before connecting the IMs [16]. All these factors substantiates that starting the IMs will constitute a critical situation for the system.

<sup>6</sup>This is information obtained from the meeting at Smøla 27. February 2017.

Some, general principles of an IM should be mentioned because they facilitates the discussion sections of Chapter 4 and 5. One of the essential variables during start-up is the electrical torque that is induced in the IM. This is given by equation (3.30) [70]:

$$\tau_{ind} = \frac{3 \cdot V_{TH}^2 \cdot (R_2/s)}{\omega_{sync} \cdot [(R_{TH} + R_2/s)^2 + (X_{TH} + X_2)^2]} \quad (3.30)$$

Here,  $V_{TH}$ ,  $R_{TH}$  and  $X_{TH}$  is the IM's Thévenin voltage, resistance and reactance respectively.  $R_2$  and  $X_2$  is the rotor resistance and leakage reactance, and  $\omega_{sync}$  is the synchronous speed. In addition,  $s$  is called the *slip* as is governed by:

$$s = \frac{\omega_{sync} - \omega_m}{\omega_{sync}},$$

where,  $\omega_m$  is the rotor mechanical speed. Thus, it is seen that if  $\omega_m < \omega_{sync}$  then the slip is positive and the induction machine operates as a motor. In the opposite case, if  $\omega_m > \omega_{sync}$  then  $s < 0$  and the induction machine operates as a generator.

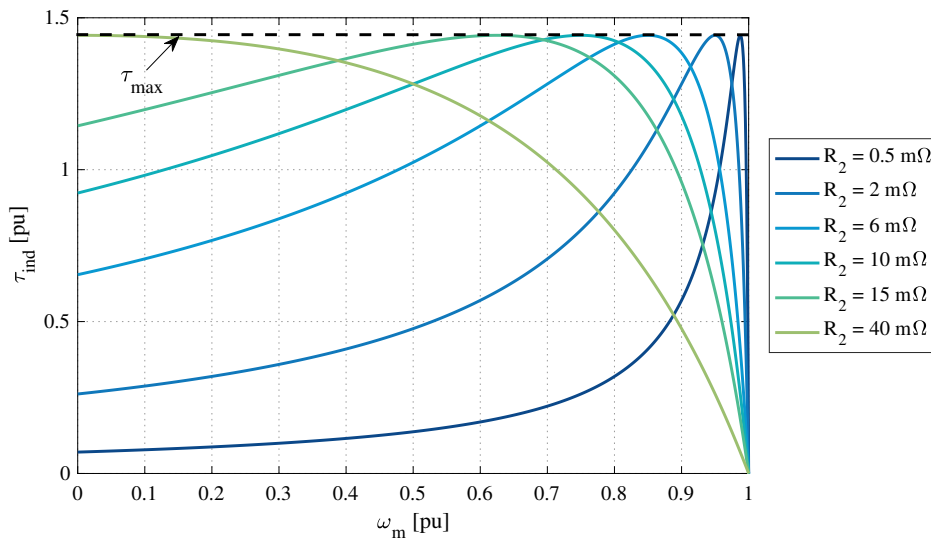


**Figure 3.29:** IM Torque-Speed Characteristic for Different  $R_2$

It is of great interest to have IMs with a high  $\tau_{ind}$ , because a larger induced torque will shorten the effective start-up time and hence obtain steady-state operation faster. From equation (3.30) it is seen that a higher Thévenin voltage or rotor resistance,  $R_2$ , can increase this torque. E.g. in IMs with wound rotor, this resistance can be varied in order to obtain the required starting torque [70]. This is illustrated in Figure 3.29. Note that even though  $R_2$  is varying, the maximum induced torque remains the same. However, increasing the resistance increases the copper losses in the rotor through the relationship  $P_{copper} = R_2 I_2^2$ . Moreover, wound IMs are more bulky, more costly and are more often prone to malfunctions than squirrel-cage IMs. Squirrel-cage IMs are the simplest and most robust version of IM, where the rotor solely consists of several metal bars that are short-circuited on each end of the rotor [70]. All the IMs considered in this thesis are assumed to have a squirrel-cage rotor. A high starting torque can be achieved through special configurations of the squirrel-cage IMs such as double-cage or deep-bar rotors [70], however, these will not be treated further in detail here.

Connected to the rotor, there is a torque linked with the compressor, called the load torque,  $\tau_{load}$ . The difference between the load torque and the induced torque determines the acceleration of the IM, and has thus great impact on the start-up transients. This implies that a smaller  $\tau_{load}$  will *decrease* the start-up time. According to [16], a centrifugal load profile reflects the behaviour of compressors in a good way. Hence the load torque can be expressed as:

$$\tau_{load} = a_1 + a_2 \omega_m^2, \quad (3.31)$$

where  $a_1$  and  $a_2$  are constants. A typical centrifugal load profile with  $a_1 = 0.15$  and  $a_2 = 0.85$  - arbitrarily chosen here - is shown in Figure 3.30. In steady-state operation,  $\tau_{load} = \tau_{ind}$ .

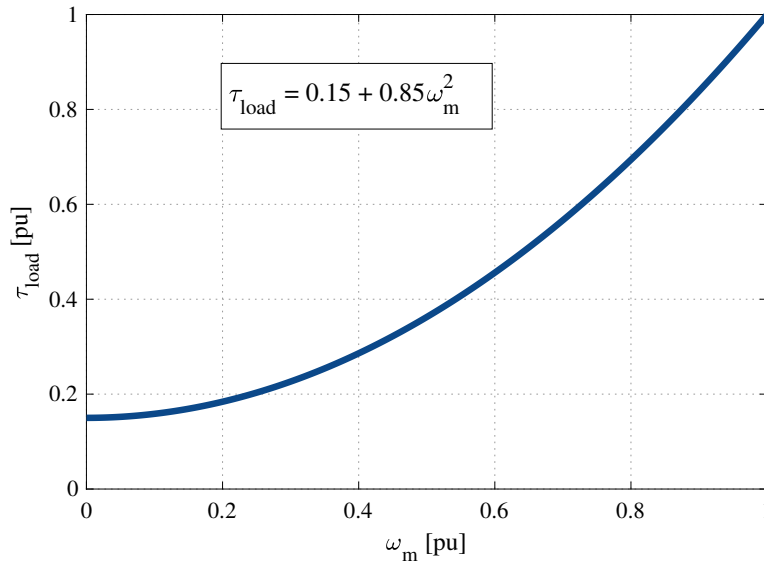


**Figure 3.30:** Centrifugal Load Torque-Speed Characteristic

As the parameters of equation (3.30) affects the IM dynamic behaviour significantly, typical values for squirrel-cage IMs from the Simulink library has been used in the simulations.

### 3.7.2 Feed Barge Electrical System

The electrical system of the fleet will use a TN-S configuration, as illustrated in Figure 3.31. TN-S stands for «Terra Neutral-Split» implying that the protective earth conductor (PE) and the neutral wire (N) are separated. In such a configuration the line-to-line voltage is 400 V, while the voltage between one phase and the neutral wire is 230 V. This makes it possible to connect both single-phase loads (230 V phase-to-neutral) and three-phase loads (400 V line-to-line) to the network.

All loads considered are three-phase loads, which implies the feed blowers covered in the previous section, and the feed barge's own power consumption. This is obviously a simplification, as not all of the barge's electrical equipment is three-phase. However, the difference is assumed to be small. The most relevant power consuming elements on the barge - apart from the feed blowers - may be heating and lighting of the barge together with power for the control system. As discussed in Section 2.2, these elements can be modelled as a lumped, stochastic load with an expectation of 9 kW and standard deviation of 2 kW. Compared to the rating of the PMSG, the DG and the IMs, 2 kW in standard deviation is very low and is treated as negligible in the simulations. Therefore, the three-phase loads have been treated as a fixed load of 9 kW. Additionally, 1 kVAR is included to simulate a lagging load.

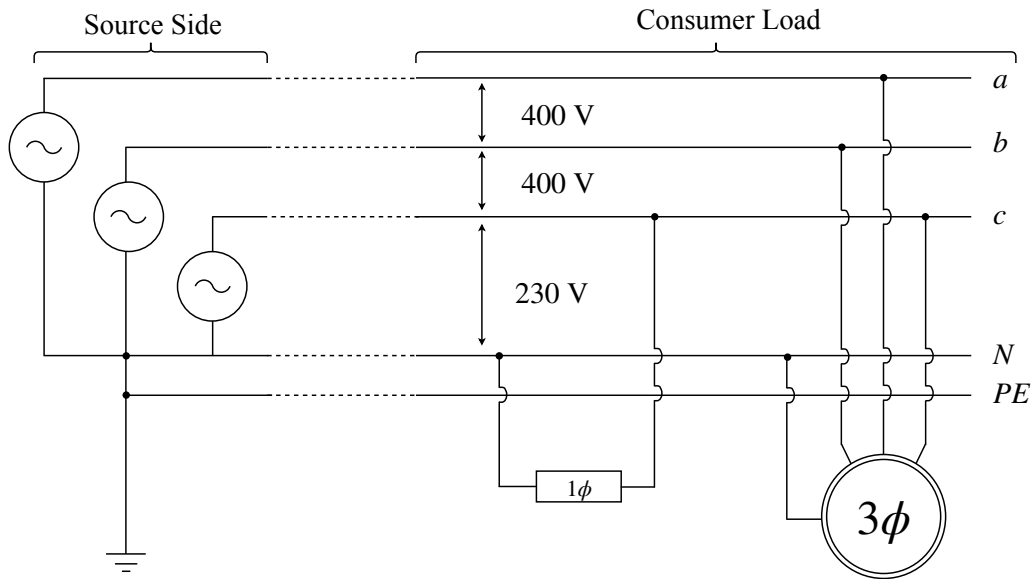


**Figure 3.31:** TN-S Configuration Schematic

### 3.8 Dump Load

Small and autonomous hybrid systems are weak grids, meaning that the total inertia present in the grid is relatively low compared to the load. Thus, the system frequency and power quality are more sensitive to variations in load. In the event of excess renewable energy, and with the energy storage fully charged, the surplus of energy will have to be dissipated to avoid a major increase in frequency. This is why a so-called dump load is needed. Traditionally, this have been based on variable resistors or power electronics. Another way of reducing the surplus of energy is through pitch control as discussed earlier.

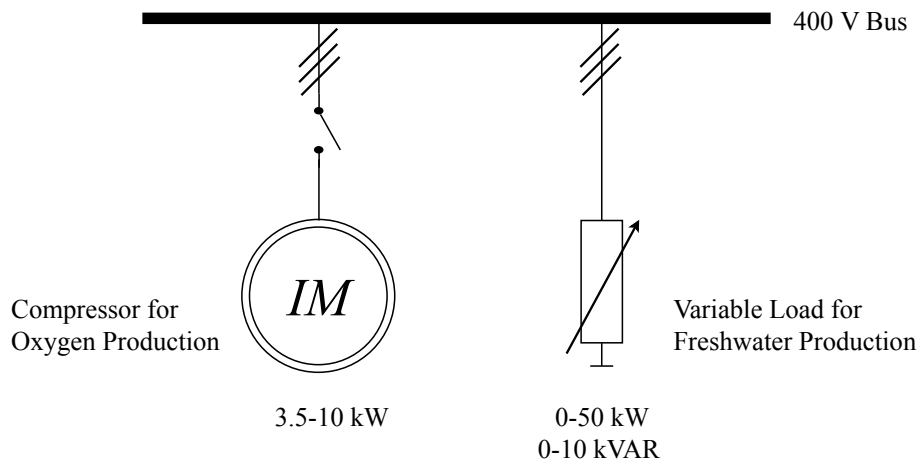


**Figure 3.32:** The Dump Load Investigated

However, all these methods waste available and renewable energy. Using the excessive energy to drive e.g. auxiliary equipment instead may be a better way of utilising the resources. It should be noted that the complexity of the system will increase by including new equipment, as a surplus of wind energy may arise and vanish in very short time. Hence, sophisticated control strategies have to be implemented to ensure safe operation of the auxiliary equipment. In this system, three different dump loads are mentioned:

#### Lice removal by means of washers

The farmed fish are fed through a lice removal system approximately 3-4 times a year. The system discussed here is delivered by Flatsetsund Engineering AS, which is one of the technology partners of WFF. The working principle is rather straightforward; A hose is placed in the cage that is to be cleaned. Then a pumping system pumps the fish into the hose, past a counting and weighing system. Then the lice are removed by low-pressure washers before they are ejected into an empty cage. The whole process only takes about 2 seconds per fish and is considered as very safe for the fish as the washing pressure is low and sea water is the only medium for transport and treatment. Each washing line has a capacity of around 30-40 tonnes per hour and is expected to use ~80 kW.

Two washing lines are proposed for this system. This implies that with six concessions (each of 780 tonnes) and an average capacity of 80 tonnes/hour for the two lines combined, it will take almost 60 hours or about seven days with eight working hours a day to clean the whole fleet. As mentioned, this procedure is carried out 3-4 times per year. The specific time for cleaning is rather flexible and (unless there is a lice crisis) can be chosen anytime the weather forecast predicts good wind conditions. It should be noted, however, that this lice treatment is not performed in practice if the wind speed exceeds 13-14 m/s.

Due to the rare operation of lice removal, it is a rather inflexible dump load. It is therefore of limited interest in this thesis and has ultimately been considered out of scope.

#### **Production and warming of freshwater**

Freshwater can be used both for the employees on the barge and the fish. Production is made through a reverse osmosis installation and is stored in a tank with a capacity of 3000-4000 m<sup>3</sup>. This production and the warming of the water is highly flexible, both with respect to timing and power consumption. Thus, this can be treated as a variable inductive load in the simulations. The power factor is assumed constant at 0.8.

#### **Oxygen production**

Oxygen production contains two main stages: First, screw compressors driven by directly coupled three-phase IMs compresses air into metallic cans where they can be stored. Multiple oxygen tanks can then be filled, constituting an oxygen bank for the fleet. The oxygen level in each cage is monitored, because this has a major impact on the fishes' health and growth. If the oxygen level in a cage is low, this will be supplied to the cage through special purpose diffusers situated at the barge. These are connected to an oxygen tank and spreads the oxygen evenly within the cage.

In the modelling process, a single three-phase IM directly coupled to the 400 V AC bus bar through a breaker, represents the oxygen production. This is seen from Figure 3.32. The IM power rating is varied through the simulations, in order to assess different scenarios.



# 4 || Model Validation

*This chapter investigates the validity of the different model implementations. Simulations are executed to evaluate the performance and feasibility of the VSC control, for the wind model and the battery model respectively. These involve the main challenges when implementing the system model, due to the power electronic interfaces. Also, a small simulation on the diesel generator behaviour is executed. Each of these three sub-systems is simulated separately, to emphasise their own features.*

## 4.1 Wind System Validation

### 4.1.1 Numerical Parameters

The rated power, voltage and frequency of Table 4.1 are obtained on the wind turbine assessed in [10], while the stator impedance and inertia are based on [58] and [77]. Additional PMSG parameters can be found in Appendix F. It should also be stated that all the per-unit values are scaled according to the procedure in Appendix B.

**Table 4.1:** PMSG and Wind System Parameters

Parameter	Symbol	Value
Nominal Electric Power	$P_n$	250 kW
Terminal Voltage	$V_1$	690 V
Frequency	$f_n$	50 Hz
Generator Stator Resistance	$R_s$	0.005 pu
Generator Stator Reactance	$X_s$	0.8 pu
Total Inertia	$H$	2 s
Converter Switching Frequency	$f_{sw}$	5000 Hz

### 4.1.2 System Response During Wind Fluctuations

This section presents the main results from validation of the wind turbine system during wind fluctuations. The focus is directed towards evaluation of the control mechanisms implemented.

A variable wind profile, which covers wind speeds between approximately 4.5-10.5 m/s is applied. A MATLAB<sup>®</sup> script producing this wind profile is presented in Appendix I. The simulation duration has been set to 37 seconds, which should be sufficient to cover system performance during changing conditions. The wind model is connected to a programmable voltage source of 690 V and 50 Hz during the whole simulation. This represents connection to a stiff grid even though the micro-grid discussed in this thesis

cannot be assumed to be stiff. Therefore, it is important to realise that the simulation results do not necessarily reflect real system behaviour, but rather explores the control performance of the wind system itself. Figure 4.1 displays the simulation results.

### Turbine Start-up

At  $t = 0$  s, the turbine is connected to the grid, resulting in a transient response in both turbine speed and electromagnetic power. The electrical turbine power increases from 0 to around 0.4 pu during the first two seconds. This coincides with the mechanical power expected at a wind speed of  $\sim 5.8$  m/s when inserting values in equation (3.3):

$$P_{mech} = \frac{1}{2} \cdot 1.225 \cdot \pi \cdot 26^2 \cdot 0.41 \cdot 5.8^3 = 98.77 \text{ kW}$$

Dividing this by the system power base of 250 kW gives a per-unit value of 0.41, which indicates that the turbine losses are small. A slight overshoot is observed for the generator speed during start-up, before it settles around the reference value after about 4 seconds.

### Wind Speed Below Rated

After the turbine is brought to normal operation, the speed reference follows the wind profile and the speed controller tries to minimise the speed deviation. Due to the turbine inertia, no sudden changes are observed for  $\omega_m$ . This is particularly visible during the wind gust (7.5-12-5 s) where the wind speed suddenly drops before it increases to around 5.8 m/s again. The wind speed is falling and so also  $\omega_m^*$ . Thus, the rotor decelerates with a small time-delay, but the electromagnetic torque is kept somewhat constant to minimise the speed error. When the wind speed recovers to pre-gust value, the rotor accelerates again, and the electromagnetic power regains its previous value, but with a slight delay caused by the inertia. It is seen that the speed control is able to follow changes in the reference fast. However, the major drawback with this is that it leads to increased power fluctuations to the grid. This trade-off is elaborated in Appendix D.4.

Figure 4.1 proves the pitch angle controller to be inactive and thus kept at 0 degrees during low wind speeds. The DC-link voltage is also observed to be maintained constant, and with little variance around its reference value of 1 pu.

### Wind Speed Above Rated

The wind speed increases steadily during the last 20 seconds of the simulation. After around 27.5 seconds the rated wind speed of 8 m/s is reached, and the pitch angle controller is active. It is seen that the pitch controller works as intended since both turbine speed and power are limited to 1 pu as the wind grows stronger. Almost no overshoot is observed for either  $\omega_m$ , nor  $P_{mech}$ . The DC-link voltage remains steady throughout the high wind speed period as well.

It should also be mentioned that the current controllers of the GSC and SSC proves to be fast and follows their respective references with high precision throughout the whole simulation. Appendix G.1 and G.2 provides the actual current curves.

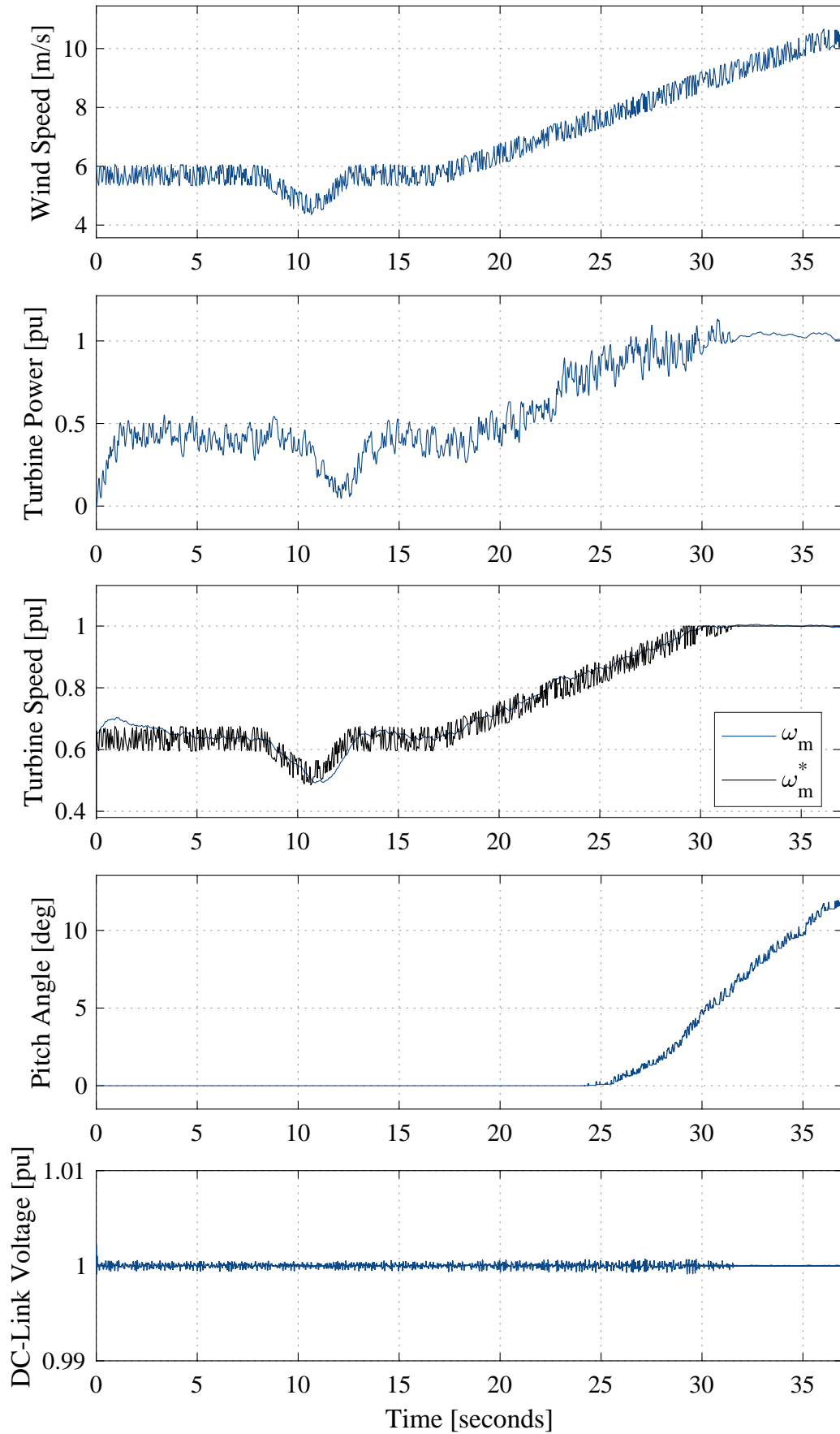
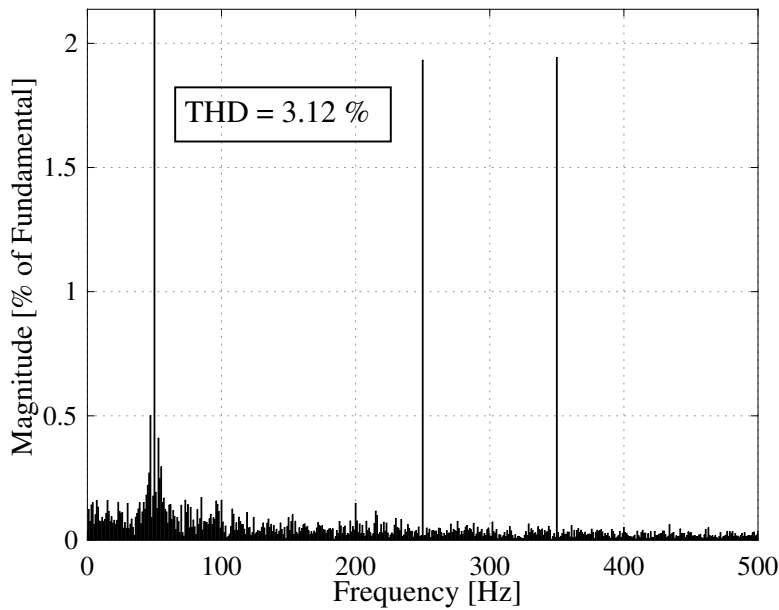


Figure 4.1: Wind System Behaviour

Power electronic pieces of equipment are highly nonlinear loads and are thus sources of harmonics. Power quality is not the main topic of this thesis, but it has become increasingly important during the last decades as the amount of power electronic equipment has boomed. A Fast Fourier Transform (FFT) Analysis have therefore been carried out, to examine the harmonic components of the line current at the PCC. Total Harmonic Distortion (THD) is a power quality measurement, which indicates the amount of harmonics that is present relative to the fundamental component. THD in current is defined as [15]:

$$THD_i = \frac{\sqrt{\sum_{h=2}^{\infty} I_h^2}}{I_1} \quad (4.1)$$

where  $I_h$  is the  $h$ th harmonic of the fundamental  $I_1$ . The same relationship applies for voltage, but this is not representative for the wind system as it is connected to a controllable voltage source at the PCC. The FFT analysis result is shown in Figure 4.2 for frequencies up to 500 Hz. Here, three significant spikes are visible at 50 Hz, 250 Hz and 350 Hz. These are all integer multiples of the fundamental frequency (50 Hz). Moreover, it is also observed that the harmonic contents at and around the fundamental frequency dominate the harmonic spectrum. The FFT analysis finds the THD to be 3.12% for the wind system during rated conditions.



**Figure 4.2:** FFT Analysis of Current at PCC

## 4.2 Battery System Validation

### 4.2.1 Numerical Parameters

Table 4.2 contains the most relevant battery system parameters. These are based on [58] and [10]. Additional parameters are found in Appendix F.

**Table 4.2:** Battery Parameters

Parameter	Symbol	Value
Nominal Voltage	$V_b$	986 V
Rated Capacity	$A_b$	100 Ah
Frequency	$f_n$	50 Hz
RL Filter Resistance	$R_{filter,b}$	0.005 pu
RL Filter Reactance	$X_{filter,b}$	0.8 pu
Converter Switching Frequency	$f_{sw}$	5000 Hz

### 4.2.2 Battery Performance During Discharge

Similarly to the wind system validation, the main focus during tests on the battery system is investigating that the control objectives of the battery VSC are fulfilled. For the BC, this involves the ability to maintain a constant output voltage of 400 V and fixed frequency of 50 Hz at the PCC.

The «Electric Drives» library in Simulink has a pre-made battery block containing the features of the Li-ion model described in Section 3.5.2. This is used in the simulations. Even though this is a simplification of a real battery, simulations have proven the model to have 95% accuracy, for a SOC between 10-100% [51]. In addition, the chosen battery design incorporates the characteristic, nonlinear relationship between SOC and V as shown in Figure 3.20.

The simulation result is summarised in Figure 4.3. It is a short simulation of only 1.9 s duration. The battery is initially connected to a 10 kW resistive load. Then four identical and inductive loads of 30 kW and 10 kVAR are added in separate steps. The first load is connected to the system after 0.25 s, the second after 0.55 s, the third at 0.85 and the last at 1.15 s. From Figure 4.3 dips in frequency and voltage occurs whenever additional load is connected. Both the frequency and voltage regulation proves to be fast and settles within 0.2 s. It is also observed that the dips become increasingly severe as the total battery load gets heavier. When the last load is added, the voltage is not able to recover at 400 V as fast as before. This is due to overloading of the battery. At nominal voltage the rated continuous discharge current is approximately 90 A. However, inspecting the current from the battery reveals that almost 160 A is drawn. Li-ion batteries are capable of supplying high currents during short time intervals, but operating the battery above its continuous rating for longer periods than some seconds may lead to overheating, damage and in worst case a thermal runaway. Thus, the battery is capable of supplying currents above rated, but the voltage control

performance is proved to be significantly weakened. In practice, this situation should be avoided in order to prevent premature degradation and thermal damage.

Analyses show that the BC control system operates with satisfactory performance, and both the voltage controllers are swift and without steady-state error. Appendix G.3 includes two plots showing  $v_d$ ,  $v_q$  and their respective references confirming this.

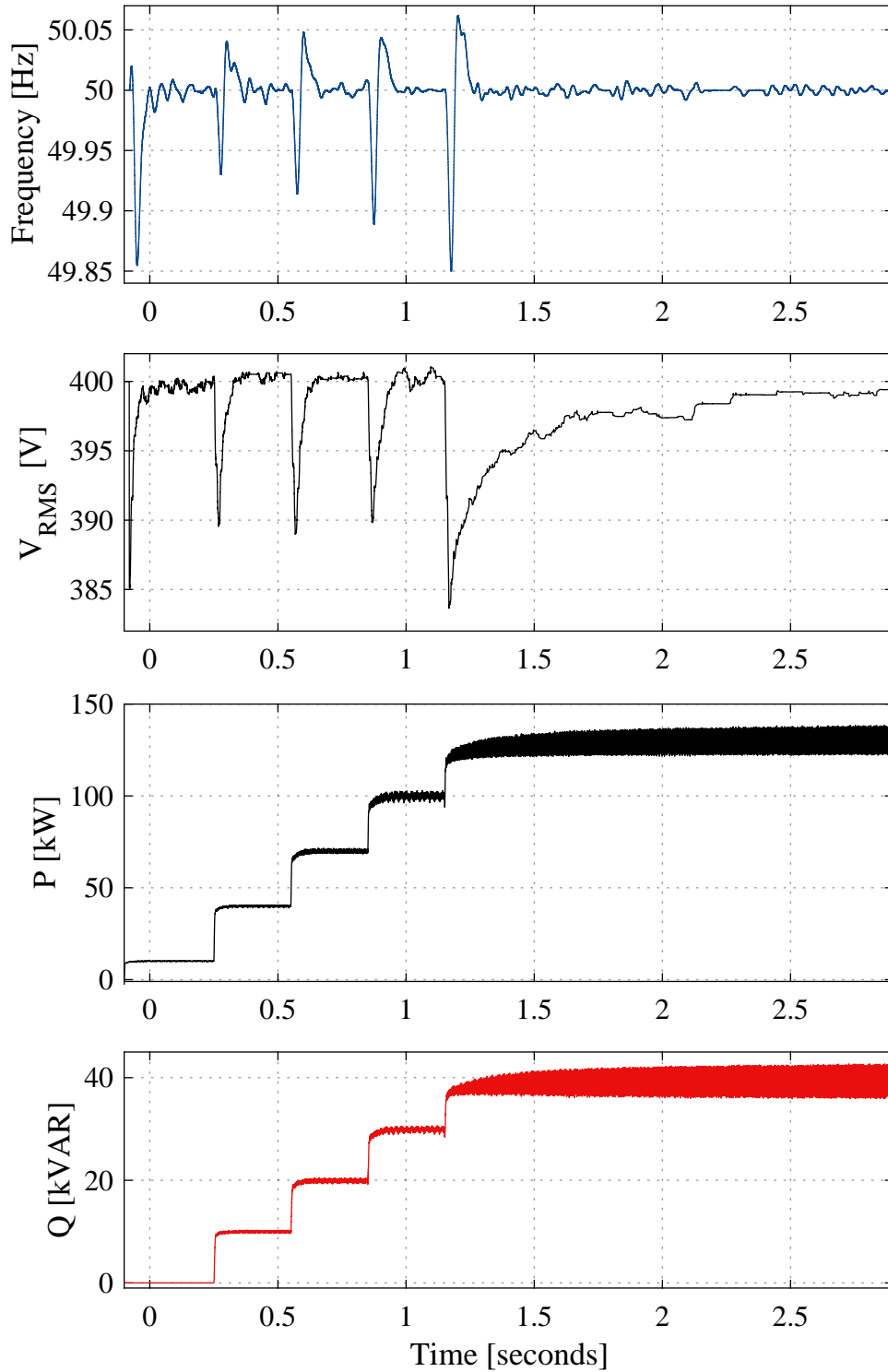


**Figure 4.3:** Battery System During Discharge

A FFT analysis is carried out for the battery system as well, and the resulting frequency spectrum is depicted in Figure 4.4. There are many similarities between this figure and the FFT analysis of the wind system. Significant spikes in magnitude occur at the fundamental frequency and its multiples, while the triplen harmonics<sup>1</sup> are cancelled out due to the three-wire system [15]. The THD is found to be 1.45% at the PCC.

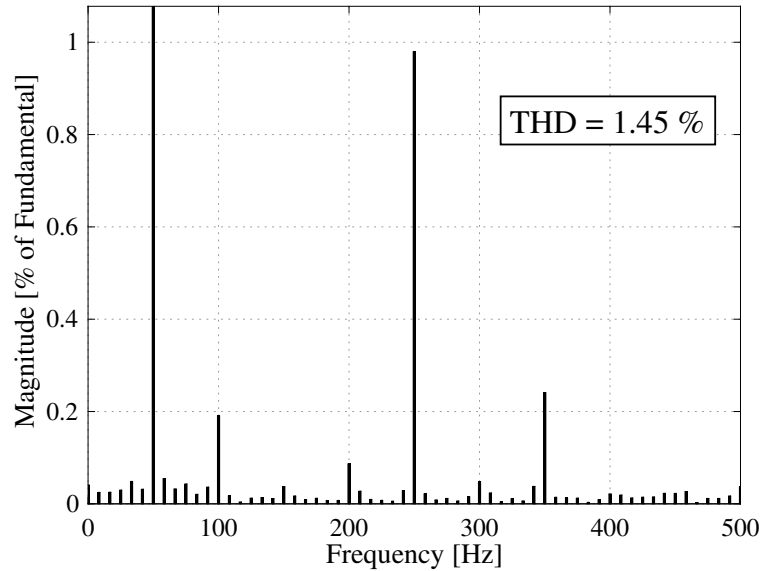


Figure 4.4: FFT Analysis of Battery Current at the PCC

## 4.3 Diesel Generator Validation

### 4.3.1 Numerical Parameters

The most relevant data for the diesel generator system are summarised in Table 4.3 below. Data sheet. Additional parameters are found in Appendix F.

Table 4.3: Diesel Generator Parameters

Parameter	Symbol	Value
Rated Power	$S_{dg}$	140 kVA
Nominal Voltage	$V_{dg}$	400 V
Frequency	$f_n$	50 Hz
Generator Stator Resistance	$R_s$	0.0317 pu
Generator Stator Reactance	$X_s$	0.114 pu

<sup>1</sup>Triplen harmonics involves the odd multiples of the 3rd harmonic i.e. 3rd, 9th, 15th, 21st and so on [78].

### 4.3.2 Test of Diesel Generator Control

The diesel generator system was explained in Section 3.6. It consists roughly of a synchronous generator, governor control facilitating the diesel engine behaviour and an AC5A excitation system. The Simulink model used for testing is shown in Appendix J. Both the synchronous generator and the AC5A model are standard components of the Simulink library, while the governor control block is adopted from [79].

The objective of the governor control is to adjust the power based on deviations in mechanical speed from its reference. As the rotational speed of the synchronous machine is locked with the electrical frequency, the goal is to keep  $\omega_m$  at 1 pu. Thus, if the load increases  $\omega_m$  will initially decrease, which creates a deviation from its reference. This error is detected and more fuel is fed into the diesel engine. Consequently, a larger torque will build up after a small time delay and the speed will increase to 1 pu.

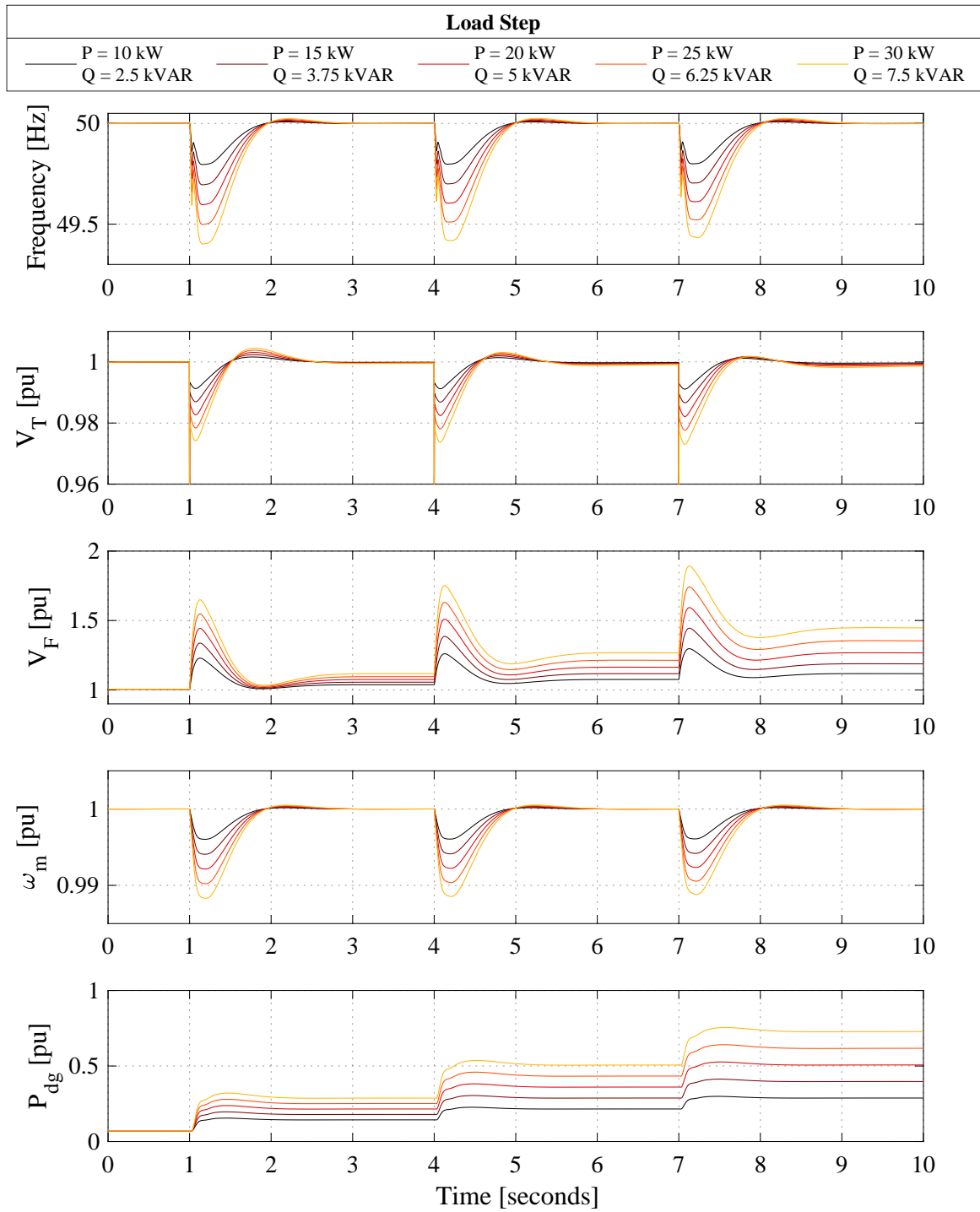
Recalling from Section 3.6.3, the excitation controller is devoted to keep the terminal voltage of the generator constant at its nominal value. Thus for an increasing load, the field voltage will have to increase to maintain a constant output voltage. This fact will be further looked into in the discussion section at the end of this chapter.

Figure 4.5 outlines the main results from the diesel system validation. Five similar simulations are carried out. In each simulation, there is initially a purely resistive load of 10 kW connected to the DG terminals. Then, three inductive loads are added successively with 3 seconds intervals between them. The value of these step-loads are increased with 5 kW for each simulation, but their power factor of 0.8 remains constant. For the first simulation the step load is then  $S_{L1} = 10 + j2.5$  kVA, for the second  $S_{L2} = 15 + j3.75$  kVA and so on. All of the step-load values are shown at the top of Figure 4.5.

The simulation results reveal dips in frequency, terminal voltage and rotational speed, while the field voltage rises at the load-step instants. It is observed that the dips and rises become more protruding as the load step increases. This is as expected from theory. Moreover, both the governor and excitation control works as intended, even at the heaviest load step, which yields a total load of  $S_L^{tot} = 100 + j22.5$  kVA or  $|S_L^{tot}| = \sqrt{100^2 + 22.5^2} = 102.5$  kVA in apparent power.

The rotational speed and terminal voltage recapture their reference values of 1 pu within  $\sim 1$  s after a load step, while the excitation system is slightly slower. Lastly, it should be mentioned that both  $f$  and  $V_{dg}$  are well within limits proposed in the IEC-61892 Standard (see Appendix H) for all the loads.



**Figure 4.5:** Diesel Generator Behaviour During Changing Load

## 4.4 Discussion

This section discusses some of the main findings from the model validation chapter.

### Wind System

The wind system controllers are performing satisfactorily according to the control objectives. The pitch controller is able to restrict the output power during high wind speed periods, and the speed controller tries to minimise the speed deviation continuously. Further investigation on the speed controller reveals that there is a trade-off between speed reference tracking and power fluctuations. Better and faster speed tracking implies improved ability to follow the optimal tip-speed,  $\lambda_{opt}$ , but is at the sacrifice of higher power fluctuations. This discussion is carried out in detail in Appendix D together with the tuning process of all the system converters.

The THD of 3.12% seems reasonable, as it is found to be around 4.2% in similar studies [80], [81]. This is also within acceptable limits of the IEEE 519 Standard for harmonics, where the strictest recommendation is a THD < 5% for this voltage level [82]. Although 3.12% clearly is below this limit, the THD at the PCC is expected to be somewhat larger in reality. This is because the wind system has been connected to a programmable voltage source during the simulation, which represents an ideal and stiff AC grid. A central simplification has been made and should be mentioned here. Cut-in and cut-out speed control for the turbine are not implemented. Even though these factors could have been included, they are not considered vital for the purpose of the analyses in this thesis, which is to validate the system controllers. Another simplification is the usage of a passive RL-filter to reduce the harmonics at the PCC. Many «Type 4» turbine producers delivers the turbine system as a package with a back-to-back converter and control system included, see for example [83] or [84]. Thus, the switching frequency and tuning process of each controller have been optimised by the producer. However, these are usually not publicly available.

### Battery System

The battery system is examined during discharge with variable load. The simulation unveils a small weakness in the control behaviour; When the discharge current exceeds the rated value, voltage control response slows down significantly. This is clearly unwanted, and real LFP batteries are normally able of sustaining discharge currents several times larger than the nominal value - at least for a second or two [43]. Further investigation of this has not been carried out due to time restrictions, but this is mentioned in the «Further Work» section. Apart from this observation, the controller response is found to be satisfactory. It is both swift and without steady-state error, due to the integrator of the PI controller. The settling time is within 0.15 s for both frequency and voltage. The tuning process, together with a step response plot are found in Appendix D.7. Figure 4.3 discloses that the frequency is able to recover quickly at 50 Hz after the last load is added, while the voltage needs several seconds. This is caused by the stiff frequency oscillator which provides the Park's Transformation angle.

The FFT analysis proved the THD to be 1.45% which is small. However, it is important

to be aware of the difference between this isolated simulation and performance when the whole system is connected. In this validation simulation, only voltage dependent resistive and inductive loads with grounded neutral are present, whilst loads in the total system include e.g. variable speed induction motors amongst others. These consists of variable speed inverters (VSIs) that includes three-phase, full-bridge diode rectifiers. The diode rectifiers are known to draw highly distorted currents from the system, which clearly is undesirable from a power quality point of view [15]. This paragraph is included - although power quality is not the main focus - in order to make the reader aware that the THD might be substantial in the real configuration, even though it appears as good in this simulation. A question may arise why it is even examined here, if it may not be representative for the whole system. The answer is that the THD can give an indication whether the control system is properly tuned or not. Moreover, another motivational factor is addressing the topic of power quality.

As mentioned in Section 4.2.2, a pre-made battery model from the Simulink library is used in the model. This incorporates measurement of SOC and the nonlinear relationship between SOC and battery terminal voltage. However, the simulations performed in this thesis has a duration of only a few seconds. Thus, these characteristic properties do not play a significant role as the SOC almost is constant and therefore also the battery voltage. If the simulation times had been made longer, these factors would have been of high interest. Additionally, temperature effects and ageing effects could have been included in the simulation model as well.

### Diesel Generator System

Simulations on the diesel generator system demonstrate acceptable behaviour for all the loading situations examined. The excitation system is observed from Figure 4.5 to have a slightly slower response than the speed governor controller. This is linked to the dominating time constants associated with the regulator and exciter of the AVR. A brief deduction of why the field voltage rises whenever more load is added should be given here: The main objective of the AVR is to adjust the field voltage of the SG such that the generator terminal voltage remains as constant as possible during load changes. Recalling from equation (3.28), this implies  $V_\phi$  to stay constant. Now, if an inductive (lagging) load increases, then the stator current  $I_A$  increases as well. The stator impedance  $R_s + jX_s$  is fixed, so if  $V_\phi = \text{constant}$  then  $E_A$  has to increase in magnitude. Equation (3.27) shows that  $E_A$  is proportional to the air gap flux, and the air gap flux is again proportional to the field current  $I_F$  in the unsaturated region. Hence, Ohms Law on the rotor-side equivalent of Figure 3.24 gives  $V_F = (R_{adj} + R_F + jX_F) \cdot I_F$ . Evidently,  $V_F$  must be increased.

To conclude the discussion on the diesel generator system, an interesting area of application of the synchronous machine could be addressed. The main goal of the proposed Hybrid Wind-Diesel System is to minimise usage of the diesel generator. In the analysis and previous discussion, the synchronous machine has only been considered in generator operation. However, the electromechanical clutch makes decoupling of the synchronous machine from the diesel engine possible. This enables the opportunity of operating the SM as a synchronous condenser. A synchronous condenser is a synchronous machine operated as a motor, but with no load. Hence it can be used as a power factor correcting unit, by changing the field excitation in the desired manner.

With overexcited field voltage, the SM will *produce*  $Q$ , while with underexcited field voltage  $Q$  will be *consumed*. This may be of great interest in a weak grid like the one discussed here, as both the SSC and BC has limited reactive power capacity. Further detail regarding the synchronous condenser can be found in e.g. [70]. Even though this is a highly propitious solution, it has not been implemented in this thesis due to time considerations.

# 5 || Case Studies

*This chapter presents main results from the three case studies. These three cases represents some of the most frequent and critical situations that the system will have to endure on a day-to-day basis.*

## 5.1 Case Study Introduction and Overview

The theoretical foundation from Chapter 2 and 3, together with the Simulink models of Chapter 4 accumulates into three case studies. They are chosen because they represents critical situations that the hybrid-system will have to frequently withstand. These are:

- ❖ Case 1 - Starting and Stopping the Feed Blowers
- ❖ Case 2 - Sudden Shortfall of Wind Power
- ❖ Case 3 - Starting the Dump Load

As no overall control structure for the system has been implemented, each case is tailor-made to enhance the challenges that may arise. The disadvantage of not having an overall control structure is discussed further in the «Discussion» section at the end of this chapter. The main motivation is not necessarily to simulate the system as accurate as possible, but rather make the reader observant on potentially crucial situations.

## 5.2 Case 1 - Starting and Stopping the Feed Blowers

The first case relates to start and stop of the feed blowers. Recalling from Chapter 2, these are expected to start around dawn and stop at sunset, every day throughout the year. The feed blowers are variable speed induction motors, connected to the AC bus bar through a PWM based VSI as described in Section 3.7.1. Six feed blowers are to be situated on the barge, but instead of using six identical IMs, only two are modelled: One with the regular feed blower size, and one equivalent representing the last five blowers (power rating  $5 \cdot 27.5 = 137.5$  kVA).

A 10 s simulation is carried out, and Figure 5.1 summarises the main results. This is found to be sufficient for the purpose of assessing the dynamics during start and stop. Instead of running two separate simulations on start and stop transients, both cases are included in the same simulation. This method is valid as long as steady-state is acquired between the two scenarios. In other words, one might think of the steady state interval as the compressed equivalent of the whole daytime.

The background for the simulation should be explained: First, the wind turbine is started and brought to steady state operation. For simplicity, the wind speed is low and treated as fixed at 4.7 m/s during the entire simulation interval. According to equation (3.3) a wind speed of 4.7 m/s implies an available mechanical power of around 55 kW. When the turbine reaches steady-state operation at this power, a switch connection the battery to the wind system is activated. At the same time, the fixed load representing the feed barge electrical consumption is connected as well. This requires 9 kW and 1 kVAR. Thus, another transient period occurs with the connected battery and fixed load before steady-state is reached again. This is where  $t = 0$  s in Figure 5.1. The transient lapse leading to the steady-state at  $t = 0$  is not included in the figure because in the real system the battery and fixed load remain connected at all times.

The wind turbine is initially delivering 55 kW and 6 kVAR dispersed between the battery and the fixed inductive load, while the frequency and RMS voltage at the PCC fluctuates with small deviation around their respective references of 50 Hz and 400 V. Here it is important to note the sign convention used for the powers, in order to avoid confusion. Wind turbine power is considered positive when power flows out from the PMSG and into the bus bar. Load power is positive when flowing from the bus bar and into the load. Battery power is considered positive when power flows into the battery (charge) and negative during discharge. This concerns both active and reactive power.

At  $t = 1.5$  s both the feed blowers are started, resulting in a rise in total load power. Both  $P_{LOAD}$  and  $Q_{LOAD}$  experiences an overshoot before settling at 77 kW and 20 kVAR after about 2 s. This is expected, due to the high inrush current of IMs as mentioned in Section 3.7.1. Another central observation here is that the wind turbine is delivering maximum available power at all times, while the battery response is swift and handles the required change in power in order to ensure power balance. Hence voltage and frequency remains stable. In coarse features, the battery power curves are the inverse of the load curves which confirms this. The starting results in a small deflection in both  $f$  and  $V_{RMS}$ , but the maximum transient frequency error is  $|\Delta f_{max}^t| = 0.8$  Hz and voltage error  $|\Delta V_{max}^t| = 16.7$  V. These are well within the transient IEC-61892 limits of  $\Delta f_{iec}^t = \pm 5$  Hz and  $\Delta V_{iec}^t = \pm 80$  V. The stationary limits are not violated either as  $|\Delta f_{max}^s| \approx 0.08$  Hz  $< \Delta f_{iec}^s = \pm 2.5$  Hz and  $|\Delta V_{max}^s| \approx 21$  V  $< \Delta V_{iec}^s \in [-40, 24]$

The feed blowers are shut off and disconnected at  $t = 6$  s. A similar, but opposite response to the starting procedure is observed. However, the transition between the two steady-states is prominently smoother. This is linked to the absence of the inrush current problem at shutdown. Apart from small oscillations in the wind turbine power, steady-state is reached within approximately 0.2 s - or around ten times faster than at start-up. The battery changes operation again from discharging to charging. Thus, stopping the feed blowers causes evidently much less stress and transients in the system than starting them. This is an important observation.

Lastly, the bottom curves of Figure 5.1 should be commented. These depicts the battery SOC and voltage, and have been included to substantiate the points mentioned in the «Discussion» section of Chapter 4 - Namely that the SOC and  $V_b$  almost are constant during the simulations due to the short simulation intervals. Initial SOC is set to around 60%. The SOC rises somewhat whenever the battery is charging and falls during discharge. When the full load is added, the SOC falls constantly with

about 0.007% per second. Assuming that the battery could be discharged until the SOC is 10% indicates that it will take  $\sim 3.57$  hours to drain the battery from SOC of 100% to 10% at the current wind conditions. The battery voltage falls slightly when it changes from charging to discharging state, but remains constant whenever steady-state is reached.

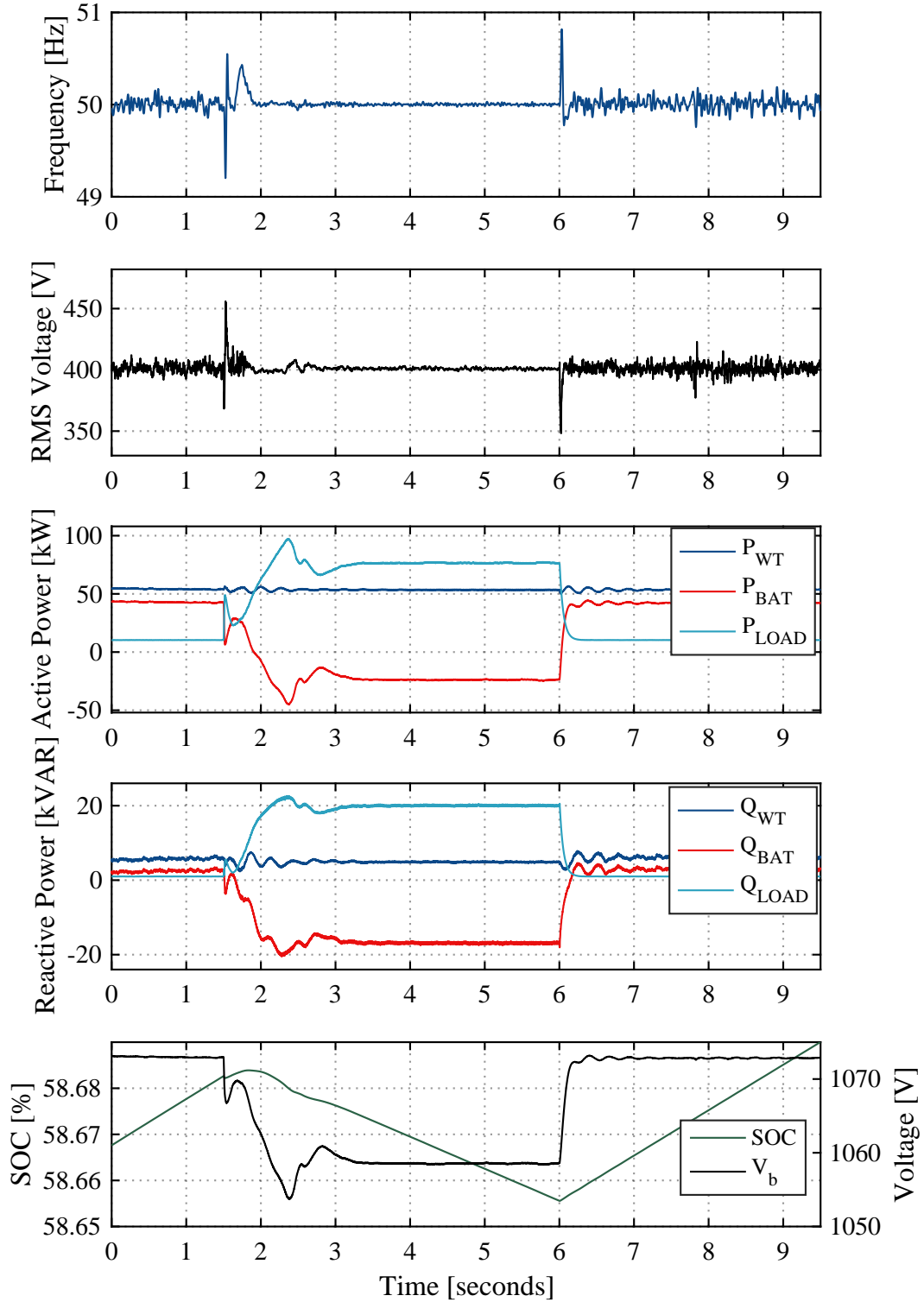


**Figure 5.1:** System Behaviour During Start of Feed Flows

### 5.3 Case 2 - Sudden Shortfall of Wind Power

The second case investigates the impact of a sudden shortfall in wind power. This may relate to a simple drop of wind power or more severe contingencies within the mechanical or electrical components of the system, resulting in disconnection of the turbine. If such a disconnection occurs, checking whether the battery is able to supply the load alone is the first priority. However, if the battery is close to completely drained, then the diesel generator have to be brought online. This is the situation assessed for the case. Hence a central assumption of this simulation is that the battery is almost empty.

Figure 5.2 summarises the system behaviour during disconnection of the wind system. The system is brought to steady-state for  $t < 0$  s. The wind conditions are assumed constant at 4.7 m/s throughout the simulation, similarly to Case 1. Observation on the figure confirms stable voltage and frequency at the PCC, during the initial steady-state  $t \in [0, 0.5)$ . The wind turbine supplies  $\sim 55$  kW and  $\sim 3.6$  kVAR initially - which is expected - while the total load demand, implying fixed load and all feed blowers running consumes around 77 kW and 20 kVAR. The battery supplies the offset between available wind power and load demand.

At  $t = 0.5$  s, the three-phase breaker which disconnects the wind system is activated. Only 0.05 s later, the diesel generator is brought online initially running at  $\omega_m = 1$  pu. The 0.05 s time difference is included to represent the time-delay associated with monitoring and overall control of the system. Both frequency and voltage experience significant dips shortly after this. The frequency drops to around 46 Hz while,  $|\Delta V_{max}^t| = 64.8$  V. Even though these values are within the IEC-61892 limits, they are considerable. It should be pointed out that the voltage curve of Figure 5.2 is filtered through a low-pass filter to reduce high-frequency noise. Thus, the real voltage dip is expected to be shorter, but also even deeper and more severe than the figure depicts.

An interesting observation is linked to the similarities between the frequency and the active power curves, and the relationship between the voltage and the reactive power curves. After the initial dip,  $f$  enters an oscillatory transient period of roughly 2 s before reaching a new and steady operation point. A similar transient can be seen for the diesel generator's active power. The reason for this behaviour is explained by the swing equation (3.29) presented in Section 3.6.3, as there is a mismatch between electromagnetic torque and mechanical torque during start-up. The oscillation peaks decline for each period, implying that the system is dynamically stable. Thus it will regain steady-state within finite time. The figure confirms this. The active power curve of the DG reveals a weakness in the model. Immediately after connection of the DG, the  $P_{DG} < 0$ , hence the DG starts in *motor operation*. This is obviously not a desirable situation because starting the DG as a motor is the primary cause of the severe voltage and frequency dip. A new simulation with improved generator starting is found in the next subsection, together with an explanation on how this problem is overcome.

The undesirable DG motor start brings with it other problems too; The large voltage dip causes a substantial increase in field voltage controlled by the DG AVR. This results in an enormous and sudden supply of reactive power in order to compensate for the



decline in voltage. Such a steep rise in  $V_F$  may cause the EESG to saturate. However, saturation effects are omitted in this simulation, due to the lack of a representative saturation curve. After the initial spike in  $V_F$  the PCC voltage rises above 400 V, leading to a reactive power consumption of the DG. The most protruding transient dies out after around 1 s followed by an oscillating period.

A few final comments to Figure 5.2 are needed. The battery endures the DG oscillations without trouble and smooths out the transients as intended. Parallel operation of battery and DG for supplying the full load proves redundant. When steady-state is attained again after  $\sim 2$  s, the DG supplies almost the entire load of around 77 kW and 20 kVAR. This yields a loading per cent of almost 57% for the 140 kVA motor.

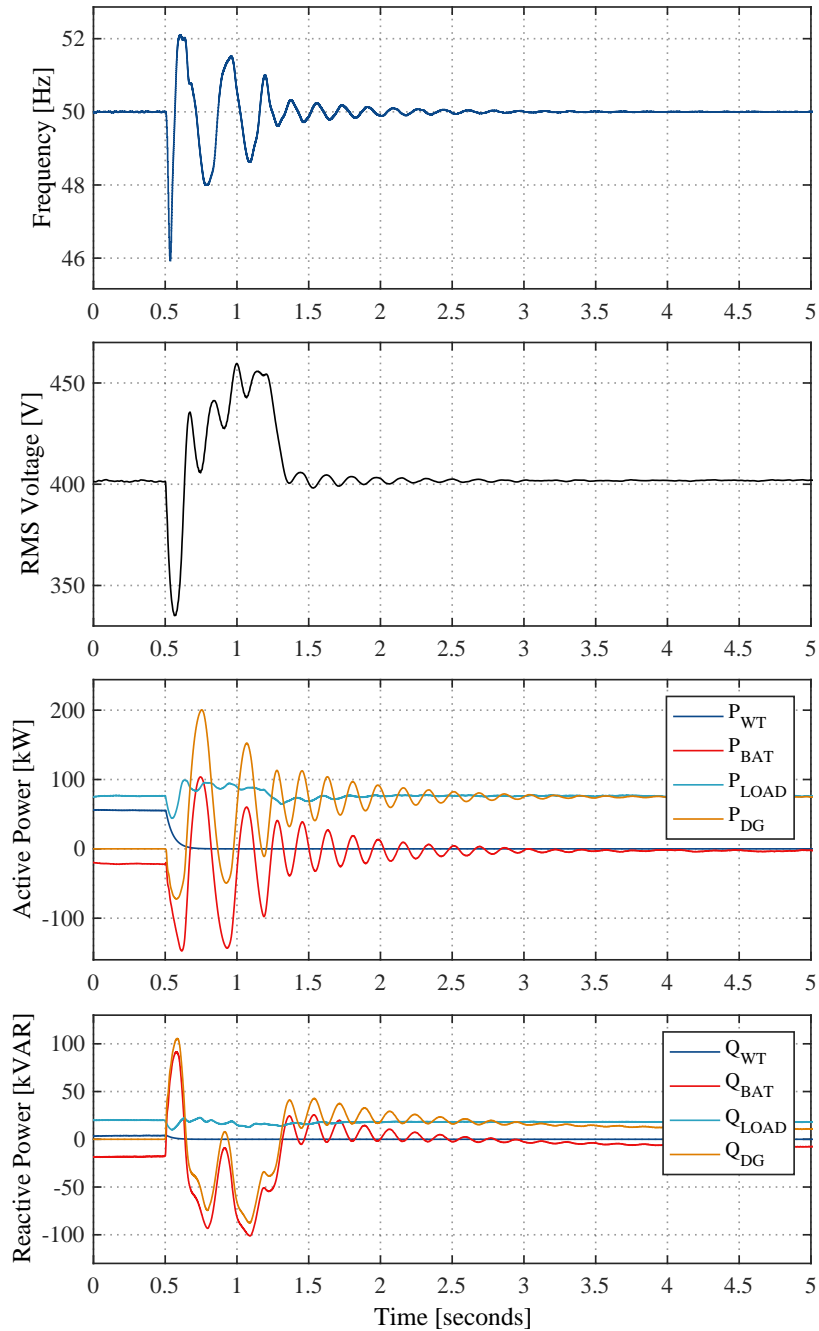


**Figure 5.2:** System Behaviour During Sudden Loss of Wind Power

Figure 5.3 shows the main DG variables during the simulation. These are included here to provide the reader with an extensive understanding of the generator dynamics occurring right after connection to the AC bus bar. As discussed above, the DG initially draws active power from the system. This causes the generator speed to increase, according to the swing equation. Please keep in mind that in motor operation  $\tau_{ind} < 0$  in equation (3.29). The mechanical torque is still positive, hence  $\tau_a > 0$  and the rotor accelerates. This speed deviation is intercepted by the governor control, which reduces the mechanical power. Additionally, the power flow changes polarity at  $t = 0.65$  s, enhancing deceleration of the machine. Thus the oscillating waveform of the speed curve of Figure 5.3 is a function of both governor control and the swing equation that describes the machine's physical behaviour. The oscillations have a frequency of around 5.5 Hz.

The terminal voltage of the diesel generator follows the voltage waveform of the PPC voltage in Figure 5.2, which is expected. However, it is exposed to high-frequency noise after the system connection. This may be due to harmonics induced by the BC and the feed blowers' VSIs. The field voltage plot is added to visualise the background for the large reactive power spike created by the DG. If the generator saturates, the increase in field voltage is limited. An insufficient increase in  $V_F$  leads to insufficient air gap flux and consequently a too low  $E_A$  to retain the terminal voltage. In the worst case, a complete voltage collapse might occur.

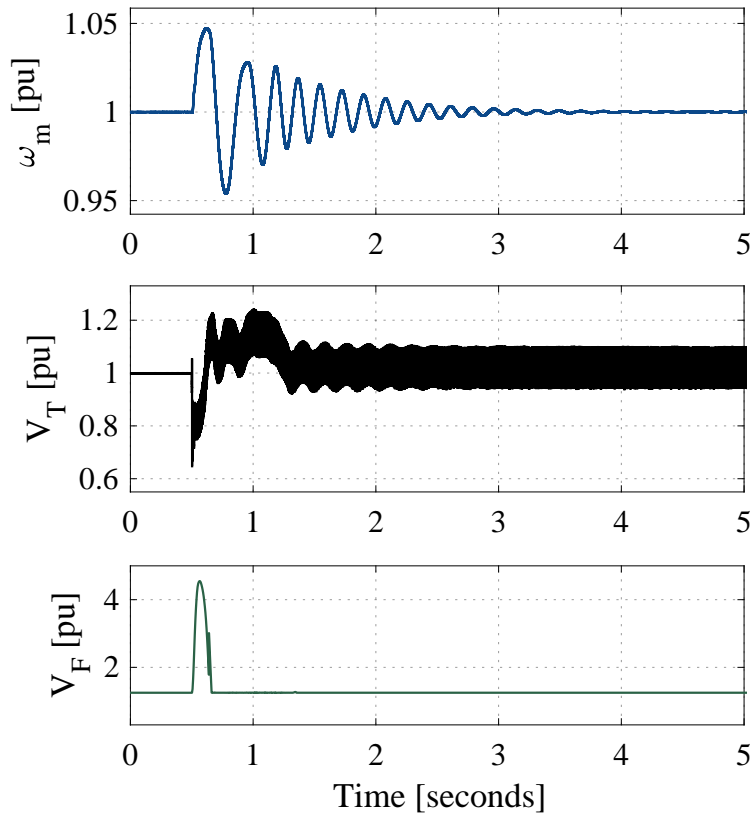


**Figure 5.3:** DG Speed, Terminal Voltage and Field Voltage

### 5.3.1 Improved Starting Procedure of the DG

Earlier in this case a problem regarding start of the DG in motor operation was seen. This is a well-known behaviour for generators with no-load frequency less than the system frequency at the instant of starting. Therefore many real generators are equipped with a reverse-power trip, which automatically disconnects the generator if it starts consuming power [70]. In order to cope with this problem, one may increase the on-coming generator's frequency above the system frequency, which will ensure that it comes on as a generator. This adjustment has been done, where  $\omega_m$  is increased from 1 pu to 1.08 pu for  $t \in [0.3, 0.9]$  s and then back to 1 pu again. Figure 5.4 and 5.5 displays the results.

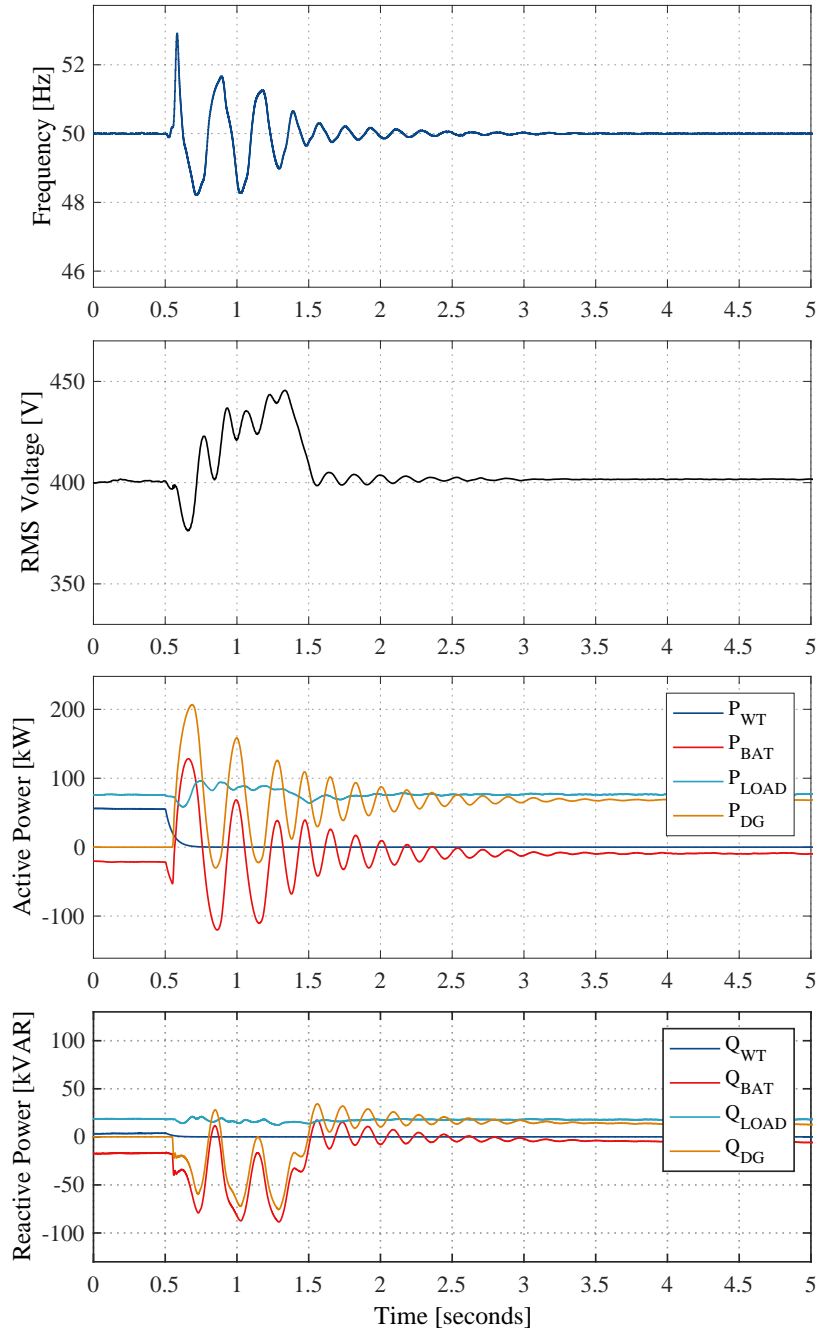


**Figure 5.4:** Improved System Behaviour During Sudden Loss of Wind Power

A comparison between Figure 5.2 and 5.4 reveals significantly improved system behaviour. First and foremost, the severe dips in voltage and frequency are substantially reduced. Instead of a frequency drop of more than 4 Hz, we now have a frequency overshoot of less than 3 Hz. The voltage dip is reduced by around 40 V, from 335.2 V to 376 V. A smaller voltage dip also eliminates the huge reactive power spike of >100 kVAR. The transient period is found to be almost equal in the two cases. Even though the improved DG starting procedure seems to be beneficial from a system perspective, it should be noted that the oscillations in active power during start-up is still large. It is actually seen that the curve of  $P_{DG}$  is below zero for the two first cycles, which may cause the generator to trip if it is equipped with a reverse-power tripping system.

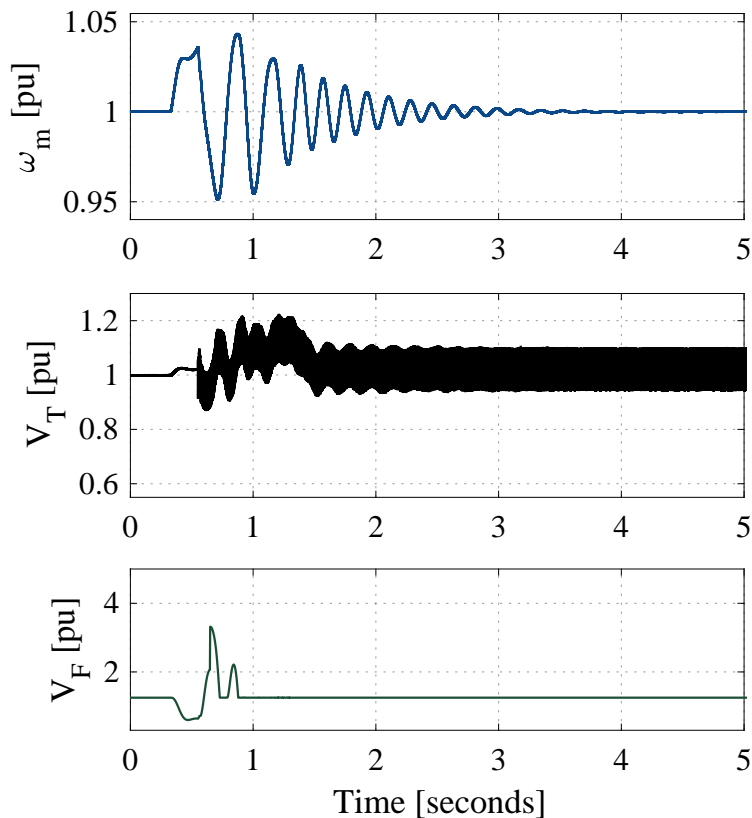


**Figure 5.5:** Improved DG Speed, Terminal Voltage and Field Voltage

Comparing Figure 5.3 and 5.5 confirms improved performance as well. This is especially seen in the terminal voltage, which is more stable and does not have a large dip. The maximum field voltage is reduced from  $\sim 4.5$  pu to around 3.5 pu. The mechanical speed curves are found almost similar in both cases.

## 5.4 Case 3 - Starting the Dump Load

The third and last case relates to starting of the dump load. In most cases, this occurs whenever there is a significant surplus of wind power compared to load, and the battery is full. Starting the dump load may be beneficial in other situations as well, e.g. if the battery is full, no wind power is available and the feed blowers are not running. In this case the DG supplies the small fixed load of 9 kW and 1 kVAR, yielding a very low operational efficiency of the DG. To elude this situation, the dump load could be started to increase this efficiency. Nevertheless, for the purpose of this case, only the former situation is looked into. This implies that the dump load starts due to excess wind power.

In conformity with the previous two cases, relevant data from the simulation is displayed in Figure 5.6. The wind speed is treated as constant at 6.3 m/s throughout the simulation, which yields a turbine power of around 126 kW. The  $P_{WT}$  curve confirms this, as the system initially is in steady-state. Moreover, all the feed blowers are running at 77 kW. The surplus of wind power yields a charging (active) power of  $126 - 77 = 49$  kW. The reactive power production of the wind system is zero. Thus the battery covers reactive power demand of the blowers.

At  $t = 1.3$  s, the dump load is started. This involves both the variable load linked with freshwater production and the compressors associated with oxygen production. As mentioned in Section 3.8, freshwater production can be represented by a variable load with  $P \in [0, 50]$  kW and  $Q \in [0, 10]$  kVAR. The heaviest situation is simulated here, hence  $P_{DUMP,1} = 50$  kW and  $Q_{DUMP,1} = 10$  kVAR. An instance with lighter variable load is also examined, but the only change is that the battery remains in charging mode after start-up instead of discharge as in Figure 5.6. The other dump load is the directly connected IM which represents one, or several compressors operating in parallel for oxygen production. The IM assessed here has a power rating of 5 kVA, while a larger IM of 10 kVAR will be evaluated later in this section.

A rather small deflection is observed in the PCC frequency after the dump loads are connected. On the contrary, the voltage transient proves substantial exceeding 500 V. This is outside the guidelines in IEC-61892 which recommends a maximal transient voltage of 480 V. The large voltage deviation also affects the loads significantly, which may damage the feed blowers. Nevertheless, the transient periods of the voltage, load and frequency are short - only around 0.5 s. Considering the reactive power curves reveals a huge overshoot in  $Q_{DUMP}$ . A closer inspection corroborates the IM to be the source of this. Such behaviour is not a surprise, referring to theory covered in Section 3.8. This phenomenon will be elaborated in further detail in the successive «Discussion» section. A similar, but smaller overshoot is also observed in  $P_{DUMP}$ .

Despite the undesired dump load deflections, the battery is capable of counteracting these transients - together with the successive oscillations in wind turbine power - effectively. The system is able to recover and relocate at a new and stable operating state.

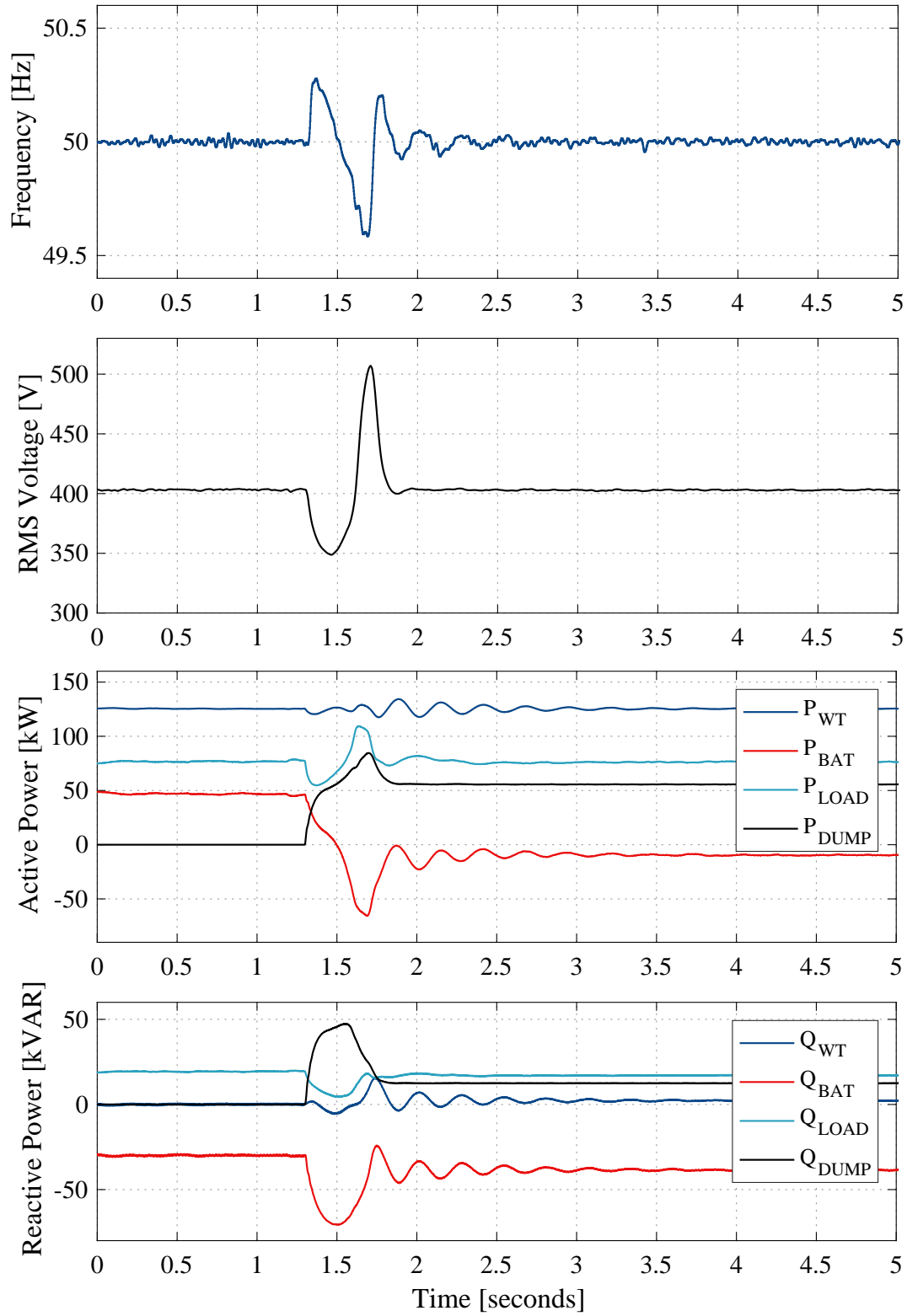


**Figure 5.6:** System Behaviour During Start of Dump Load

### 5.4.1 Voltage Collapse During Start of Large IM

The Hybrid Wind-Diesel System is far weaker than a land-based grid, making it more vulnerable to sudden changes such as contingencies or motor starting. These events may cause a permanent voltage collapse in the system. Directly connected induction motors are particularly exposed to voltage dips, because the induced torque is proportional to the voltage squared, referring to equation (3.30). The steady-state operating point of the IM is located where  $\tau_{ind} = \tau_{load}$  (see Figure 3.29 and 3.30). Thus, even a small decrease in voltage reduces the electromagnetic torque significantly. This leads to a shift in the IM's operating point to a lower mechanical speed, causing the slip to increase. A larger slip implies increased reactive power consumption. This is one of the major drawbacks of directly connected IMs, and it is presented in this subsection.

A larger (10 kVA) motor replaces the former 5 kVA IM unit for oxygen production. Figure 5.7 shows RMS voltage at the PCC and reactive power during start-up. The IM draws high current initially. This leads to a voltage dip at the PCC. The voltage dip reduces  $\tau_{ind}$  which slows down the starting procedure and the reactive power consumption increases. The battery, which is the prime regulating unit is not able to supply the required amount of reactive power. This leads to a chain reaction where the voltage continues to fall. Consequently, a point of no return is reached. The SSC reactive power controller stops working properly, and a permanent voltage collapse is attained.

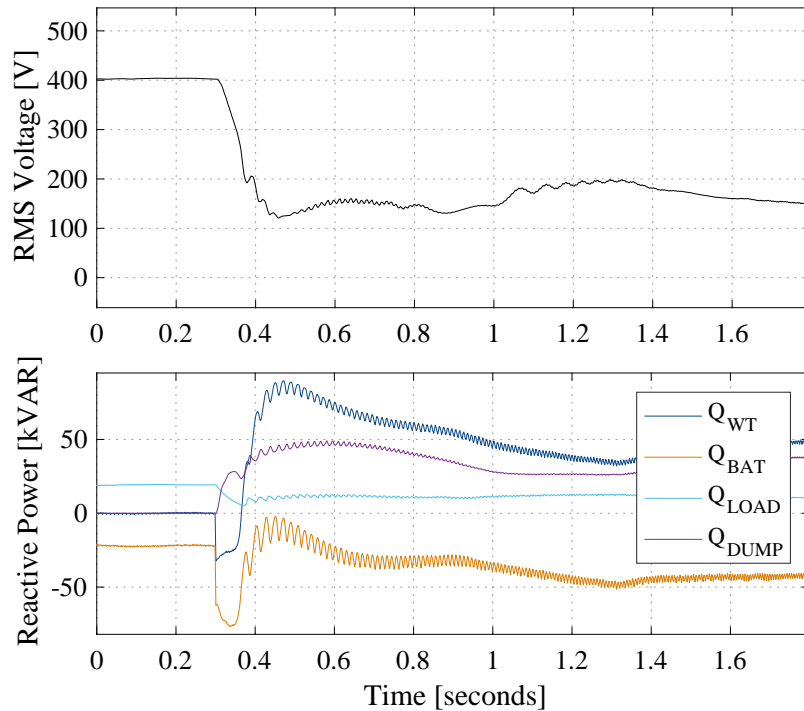


**Figure 5.7:** Voltage Collapse During Start of 10 kVA IM

## 5.5 Discussion

Three cases representing possible critical situations are investigated in this chapter. Choosing the appropriate cases is a challenge as there are numerous possible system states. E.g. during start-up of the feed blowers, the wind conditions could be higher or lower than the one assessed. The wind could also drop drastically right before the blowers starts, yielding an even more challenging situation. This may lead to start of the diesel generator if the battery is empty. This is only one example showing that complex situations may occur at any instant. It is thus important to be aware of the limitations of these simulations, as they do not take all possible system states into consideration. However, the aim of the case studies is to provide the reader with a feeling of the system dynamic feasibility, rather than assessing every possible situation that may occur.

A large improvement in the Simulink model is linked to implementation of an overall control scheme for the system. This is favourable as the need for tailoring of the various disturbances, and system states are eliminated. An overall control structure can continuously decide which components that should be delivering and consuming power, based on a hierarchy. The hierarchy will depend on whether there is a surplus or deficit of wind energy in the system. In the case of surplus, the hierarchy in descending priority is (1) wind turbine, (2) charge the battery, (3) dump load and (4) pitching the wind turbine to reduce output power. In the case of deficit, the priorities are (1) wind turbine, (2) discharging the battery and (3) using the diesel aggregates. In both cases, the top priority in the system is utilising as much of the wind power as possible. Then comes the battery, which is charged (when possible) during surplus and discharged (when possible) during deficit. Implementation of an overall control structure is considered as further work.

An interesting observation from the case studies is that the reactive power overshoot caused by starting of the feed blowers (see Figure 5.1) is noteworthy lower than start of the oxygen compressor (see Figure 5.6) - even though this has a much smaller power rating. This addresses the principal difference between fixed speed induction motors and variable-speed induction motors. In variable-speed IMs such as the feed blowers, the VSI decouples the motor from the grid due to the DC-Link capacitor, similar to the DC-Link of the wind turbine system. The decoupling effect prevents reactive power to flow from directly from the grid to the motor. Hence, the reactive power of a variable-speed IM is locally generated by the VSI. This reduces the voltage dip at PCC, compared to a fixed speed IM. Another solution may be replacing the diode rectifier of the VSI with a bi-directional VSC. Such a back-to-back VSC configuration could actually provide reactive power support during disturbances.

A final remark on Case 1 concerns the battery voltage of Figure 5.1, because it seems higher than the stated nominal battery voltage from Table 4.2. The reason for this is solely that the nominal battery voltage,  $V_b = 986$  V, is defined as the voltage present at the end of the linear zone of the discharge curve [51]. Figure 3.20 confirms this.



In Case 2 a problem regarding start of the DG in motor operation was seen. However, increasing the generator speed for a short time during start-up improved the system response considerably.

The third case revealed how vulnerable the system is to start-up of a directly connected IM. Even for a 10 kVA motor, the system experienced a permanent voltage collapse. The large initial reactive power requirement of the IM could as an example be counteracted by adding a shunt capacitor bank at the motor terminals. The effect of this was investigated in a separate simulation - which has not been included - and it was found that a capacitor bank of 25 kVAR was sufficient to prevent voltage collapse of the 10 kVAR motor. Instead of purchasing a capacitor bank solely for the oxygen production compressors, another possibility involves the DG to be operated as a synchronous condenser as mentioned in Section 4.4.

Overall, the system shows promising performance in all of the three cases. The VSC controllers are able to recover system stability after three for the most common disturbances, and both frequency and voltage remains within the grid code limits, except the voltage at dump load starting. Nevertheless, some improvements should be added to the model to represent a more realistic autonomous system. These are addressed in Section 6.1.

To round off this section, some of the results from the previous specialisation project should be linked to the results found here. Steady-state simulations in [10] showed that the wind turbine produces at maximum power for a substantial part of a (normal) year. This implies  $\sim 250$  kW from the turbine. When the feed blowers are running, the total main load will lie around 80 kW, meaning there is a surplus of 170 kW of wind compared to load. This has to be consumed by the dump load and the battery. The maximum dump load assessed here is 60 kW, implying that the battery will have to endure charging at approximately 110 kW to avoid de-rating of the turbine. Here, de-rating of the turbine involves pitching the blades in order to constrain output power. Hence, an important feature for the battery is that it should endure high charging and discharging powers. Furthermore, only one DG has been included in the model, while results from [10] indicate that the average power *per hour in operation* supplied by the DG is expected to lie around 50-55 kW. This yields a low expected load factor, hence two smaller DGs or one large and one small DG may be more beneficial from an efficiency point of view. Another, and simpler, solution concerns allowing the DG to charge the battery or run the dump load if running the DG is inevitable. This is a win-win situation as the load factor and efficiency of the DG increases, while the battery can be charged, oxygen compressors can be run and freshwater produced.



## 6 || Conclusions

Possibilities of including locally available renewable resources in conventional offshore fish farms have been explored in this thesis. This chapter contains the most important conclusions that can be drawn.

The system that has been investigated is a Hybrid Wind-Diesel System, equipped with a Lithium-ion battery energy storing unit. Chapter 2 gives an introduction to the offshore fish farm, its consumption profile and wind conditions. The concepts presented in Chapter 3 covers the necessary theory for implementing and understanding the dynamic simulation model. In other, words it serves as the cornerstone of the thesis.

From the model validation in Chapter 4 it is concluded that the VSC controls of the wind turbine and battery system performs satisfactorily. Despite this, an undesirable behaviour was revealed in the battery system: When the discharge current exceeded the rated value, voltage control response slowed down significantly. Another, more robust control scheme, with an outer control loop may be favourable for the battery converter. However, this behaviour was only seen during the heaviest loading in Chapter 4 and not in any of the case studies of Chapter 5. Thus, it appears redundant, at least for the most common system disturbances. The THD values from the FFT analyses in Chapter 4 were lower than the strictest recommendations in IEEE 519. Nevertheless, it should be noted that they are expected to be somewhat higher when all the system components are connected.

The diesel generator's speed governor control and AVR were tested thoroughly as well. Both control systems were swift - regulating within approximately 1 s - and able to preserve frequency and voltage stability for all the loading conditions examined. Saturation effects of the synchronous generator have been omitted in any of the simulations, due to the lack of a representative saturation curve.

Frequency and voltage values complied with the IEC-61892 grid code limits for all cases of Chapter 5, except for the high voltage spike during start of the directly connected IM in Case 3. Start-up of the fixed-speed IM in Case 3 also emphasised how vulnerable the system is to large and abrupt changes in reactive power. A too large IM may lead to a permanent voltage collapse. Additional reactive power compensating units may be placed in shunt at the IM terminals to cope with this problem. Another and perhaps more relevant option is to use the diesel generator as a synchronous condenser in such situations. In this way, purchasing new and expensive capacitor banks can be avoided.

The case study results of Chapter 5 indicate technical feasibility for the system. The battery serves successfully as a short-term regulating unit and smooths out the worst transients - which is intended. From a dynamic stability point of view, proper control by means of VSCs shows promising features in a weak electrical system such as this. However, several assumptions and simplifications have been made during the implementation process. Thus, this should be viewed as a preliminary study of system

feasibility, with the purpose of encouraging further work within the area of study. The main shortcomings and possibilities of improvement are elaborated in the next section.

Overall, both the steady-state analysis made in the specialisation project and the findings from this thesis indicates that a hybrid system of this sort may be of great interest to the fish farming industry in future years. Due to the extreme growth in both income and tonnes of fish exported, new governmental regulations may force participants of the industry to demarcate their emissions. Thus, reducing CO<sub>2</sub> emission, while simultaneously improving fish health seems like an attractive solution.

### 6.1 Shortcomings and Further Work

To round up this master thesis, some of its shortcomings and possibilities for further work are outlined here:

- ❖ A major improvement is linked to the implementation of an overall control scheme. This would greatly amend realistic system behaviour, as the need for tailoring specific case studies diminishes.
- ❖ The Simulink models should preferably be revised with respect to simulation speed. When several components are connected - as in the case studies in Chapter 5 - the simulations are very slow. Thus, obtaining results from the case studies have taken a substantial amount of time. Using an average model of the VSCs instead of a detailed PWM-based model which have been used here, may allow a longer time step and therefore increase simulation speed. Increased simulation speed can again marshal longer simulation runs and also encourage sensitivity analyses. This may serve as a foundation for optimising power and energy ratings of the system components.
- ❖ A more comprehensive data collection process is preferable. This is mainly linked towards specific machine data, which have been found challenging. Neglecting the EESG saturation effects is a result of this.
- ❖ Creating a scalable and more generic simulation model could be interesting. In this way, e.g. the effect of adding more diesel generators could be looked further into.
- ❖ More sophisticated control structures can be applied in order to optimise system behaviour. The cascaded control structure which has been used in this thesis is considered robust, but also rather slow.
- ❖ Investigation of transient stability issues, e.g. system behaviour during short-circuit conditions and other contingencies may be a natural extension to the dynamic system analyses.
- ❖ Other dump loads, such as hydrogen production can be considered.

- ❖ Assessing large offshore wind turbines, which can supply more than only one fish farm, may be of interest. This will, however, increase the complexity noticeably.
- ❖ A thorough economic study with cost predictions may form a sound decision basis. Also, economic feasibility is probably the main factor for this kind of system to be found attractive from the industry's point of view.



# Bibliography

- [1] SSB, “Oversikt over geografiske forhold.” <https://www.ssb.no/a/aarbok/kart/i.html>, 2013. Statistisk Sentralbyrå, Retrieved 20. January 2017.
- [2] SSB, “Aquaculture 2015 - final figures.” <https://www.ssb.no/en/jord-skog-jakt-og-fiskeri/statistikker/fiskeoppdrett/aar/2016-10-28>, 2016. Statistisk Sentralbyrå, Retrieved 20. January 2017.
- [3] FAO, *The State of World Fisheries and Aquaculture 2016 - Contributing to food security and nutrition for all*. Food and Agriculture Organization of the United Nations (FAO), 2016. Rome. ISBN 978-92-5-109185-2.
- [4] J. B. Malosh, R. Johnson, and S. Bubendorf, “Part-load economy of diesel-electric generators,” technical report, Department of Transportation and Public Facilities, Alaska, June 1985. [http://www.dot.state.ak.us/stwddes/research/assets/pdf/ak\\_rd\\_86\\_01.pdf](http://www.dot.state.ak.us/stwddes/research/assets/pdf/ak_rd_86_01.pdf), Retrieved 14. February 2017.
- [5] “Regjeringen lanserer havstrategi.” <https://www.regjeringen.no/no/aktuelt/regjeringen-lanserer-havstrategi/id2502018/>. Press release from regjeringen.no, Retrieved 14. February 2017.
- [6] “Høringsnotat – implementering av meld st. 16 (2014-2015),” June 2016. The Norwegian Ministry of Trade Industry Fisheries, Consultation document on Storting proposition no.16 (2014-2015). Accessible from <https://www.regjeringen.no/contentassets/c9a57b93b9a04cabb67665314dc3bbd6/horingsnotat.pdf>, Retrieved 30. January 2017.
- [7] “Vil ha fortgang i teknologiutviklingen.” <https://www.regjeringen.no/no/aktuelt/vil-ha-fortgang-i-teknologiutvikling/id2470187/>. Press release from regjeringen.no, Retrieved 20. April 2017.
- [8] E. R. Ystgård, “Småskala vindkraft i fiskeoppdrettsnæringen – en lønnsom løsning?,” 2015. Project report from Norges Miljø- og Biovitenskapelige Universitet.
- [9] M. Wirkola, G. Ngoc, and B. Træthaug, “Vindkraftdrevet oppdrettsanlegg,” 2015. Bachelor Thesis from Høgskolen i Bergen.
- [10] M. Holt, “A Hybrid Wind-Diesel Stand-Alone System for Fish Farming Applications,” December 2016. Specialization project, NTNU.
- [11] “Cage farming aquaculture.” <http://www.akvagroup.com/Downloads/Cage%20farming%20%20EN.pdf>. Akva Group, Retrieved 1. June 2017.
- [12] Laksefakta, “Hva er i fôret til laksen?.” <https://laksefakta.no/hva-spiser-laksen/hva-er-i-foret-til-laksen>. Laksefakta.no, Retrieved 15. May 2017.

- [13] P. P. Revheim, 24. October 2016. Email message.
- [14] P. P. Revheim, 12. December 2016. Email message.
- [15] N. Mohan, T. M. Undeland, and W. P. Robbins, *Power electronics*. Wiley, 1988.
- [16] A. R. Årdal, “Feasibility Studies on Integrating Offshore Wind Power with Oil Platforms,” Master Thesis, NTNU, June 2011.
- [17] T. M. Haileselassie, M. Molinas, T. Undeland, *et al.*, “Multi-terminal vsc-hvdc system for integration of offshore wind farms and green electrification of platforms in the north sea,” in *Nordic Workshop on Power and Industrial Electronics (NOR-PIE/2008)*, June 9-11, 2008, Espoo, Finland, Helsinki University of Technology, 2008.
- [18] H. Saadat, *Power System Analysis*. PSA Publishing, Third Edition ed., 2010. ISBN: 978-0-9845438-0-9.
- [19] R. E. Doherty and C. A. Nickle, *Synchronous Machines*, vol. Vol. 45. AIEE Trans., 1926. pp. 912-942.
- [20] R. H. Park, *Two Reaction Theory of Synchronous Machines - Generalized Method of Analysis*, vol. Vol. 48. AIEE Trans., 1929. pp. 716-729.
- [21] J. Pierik, J. Morren, E. Wiggelinkhuizen, S. de Haan, T. van Engelen, and J. Bozelie, “Electrical and control aspects of offshore wind farms ii (erao ii), volume 1: Dynamic models of wind farms,” tech. rep., Energy Research Centre of the Netherlands, June 2004. ECN project number: 7.4336.
- [22] J. Manwell, J. McGowan, and A. Rogers, *Wind Energy Explained: Theory, Design and Application*. John Wiley & Sons, Second Edition ed., 2009.
- [23] P. Sørensen, B. Andresen, J. Fortmann, and P. Pourbeik, “Modular structure of wind turbine models in iec 61400-27-1,” in *Power and Energy Society General Meeting. Vancouver, BC, Canada*, 2013.
- [24] S. B. Elghali, M. Benbouzid, J. F. Charpentier, T. Ahmed-Ali, and I. Munteanu, “High-order sliding mode control of a marine current turbine driven permanent magnet synchronous generator,” in *Electric Machines and Drives Conference, 2009. IEMDC’09. IEEE International*, pp. 1541–1546, IEEE, 2009.
- [25] M. Ragheb and A. M. Ragheb, *Wind turbines theory-the betz equation and optimal rotor tip speed ratio*. INTECH Open Access Publisher, 2011.
- [26] ICAO, *Manual of the ICAO Standard Atmosphere*. International Civil Aviation Organization, third ed., 1993. Doc 74488/3.
- [27] M. O. L. Hansen, *Aerodynamics of Wind Turbines*. Earthscan, Second Edition ed., 2008. ISBN: 978-1-84407-438-9.
- [28] B. Liu, X. Peng, and T. Undeland, “Centralized power control strategy of offshore



- wind farm with permanent magnetic generators,” in *Power Electronics and Motion Control Conference, 2009. IPEMC'09. IEEE 6th International*, pp. 1075–1079, IEEE, 2009.
- [29] J. Zhang, M. Cheng, Z. Chen, and X. Fu, “Pitch angle control for variable speed wind turbines,” in *Electric Utility Deregulation and Restructuring and Power Technologies, 2008. DRPT 2008. Third International Conference on*, pp. 2691–2696, IEEE, 2008.
  - [30] S. Mueen, J. Tamura, and T. Murata, *Stability augmentation of a grid-connected wind farm*. Springer Science & Business Media, 2008.
  - [31] G. Michalke, A. D. Hansen, and T. Hartkopf, “Control strategy of a variable speed wind turbine with multipole permanent magnet synchronous generator,” in *Proceedings of European Wind Energy Conference and Exhibition*, 2007.
  - [32] A. D. Hansen and G. Michalke, “Modelling and control of variable-speed multi-pole permanent magnet synchronous generator wind turbine,” *Wind Energy*, vol. 11, no. 5, pp. 537–554, 2008.
  - [33] J. Slootweg, S. De Haan, H. Polinder, and W. Kling, “General model for representing variable speed wind turbines in power system dynamics simulations,” *IEEE Transactions on power systems*, vol. 18, no. 1, pp. 144–151, 2003.
  - [34] M. Rosyadi, S. Mueen, R. Takahashi, and J. Tamura, “A design fuzzy logic controller for a permanent magnet wind generator to enhance the dynamic stability of wind farms,” *Applied Sciences*, vol. 2, no. 4, pp. 780–800, 2012.
  - [35] N. Mohan, *Advanced Electric Drives: analysis, control, and modeling using MATLAB/Simulink*. John Wiley & sons, 2014.
  - [36] J. Liu, H. Nian, J. Li, and R. Zeng, “Sensorless control of pmsg for wind turbines based on the on-line parameter identification,” in *Electrical Machines and Systems, 2009. ICEMS 2009. International Conference on*, pp. 1–6, IEEE, 2009.
  - [37] Z. Wu, X. Dou, J. Chu, and M. Hu, “Operation and control of a direct-driven pmsg-based wind turbine system with an auxiliary parallel grid-side converter,” *Energies*, vol. 6, no. 7, pp. 3405–3421, 2013.
  - [38] S. K. Chaudhary, *Control and protection of wind power plants with VSC-HVDC connection*. PhD thesis, Aalborg University, Aalborg, Denmark, 2011.
  - [39] C. Bajracharya, “Control of vsc-hvdc for wind power,” Master Thesis, NTNU, June 2008.
  - [40] F. Katiraei and M. R. Iravani, “Power management strategies for a microgrid with multiple distributed generation units,” *IEEE transactions on power systems*, vol. 21, no. 4, pp. 1821–1831, 2006.
  - [41] A. Joseph and M. Shahidehpour, “Battery storage systems in electric power sys-

- tems,” in *2006 IEEE Power Engineering Society General Meeting*, pp. 8–pp, IEEE, 2006.
- [42] J. M. Grothoff, “Battery storage for renewables: market status and technology outlook,” tech. rep., Technical Report January, International Renewable Energy Agency (IRENA), 2015.
  - [43] E. M. Krieger, J. Cannarella, and C. B. Arnold, “A comparison of lead-acid and lithium-based battery behavior and capacity fade in off-grid renewable charging applications,” *Energy*, vol. 60, pp. 492–500, 2013.
  - [44] V. Svoboda, H. Wenzl, R. Kaiser, A. Jossen, I. Baring-Gould, J. Manwell, P. Lundsager, H. Bindner, T. Cronin, P. Nørgård, *et al.*, “Operating conditions of batteries in off-grid renewable energy systems,” *Solar Energy*, vol. 81, no. 11, pp. 1409–1425, 2007.
  - [45] A. W. Golubkov, D. Fuchs, J. Wagner, H. Wiltsche, C. Stangl, G. Fauler, G. Voitic, A. Thaler, and V. Hacker, “Thermal-runaway experiments on consumer li-ion batteries with metal-oxide and olivin-type cathodes,” *RSC Advances*, vol. 4, no. 7, pp. 3633–3642, 2014.
  - [46] G. Fuchs, B. Lunz, M. Leuthold, and D. Sauer, “Technologischer überblick zur speicherung von elektrizität,” *Überblick zum Potenzial und zu Perspektiven des Einsatzes elektrischer Speichertechnologien*, Stuttgart, 2012.
  - [47] IEA, “Technology roadmap: Energy storage.” <https://www.iea.org/publications/freepublications/publication/TechnologyRoadmapEnergyStorage.pdf>. International Energy Agency, Retrieved 12. March 2017.
  - [48] B. Marshall, “How lithium-ion batteries work.” <http://electronics.howstuffworks.com/everyday-tech/lithium-ion-battery.htm>, November 2006. HowStuffWorks, Retrieved 24. May 2017.
  - [49] A. Joseph and M. Shahidehpour, “Battery storage systems in electric power systems,” in *2006 IEEE Power Engineering Society General Meeting*, pp. 8–pp, IEEE, 2006.
  - [50] G. Albright and S. Al-Hallaj, “Making lithium-ion safe through thermal management.” AllCell Technologies, Chicago, Retrieved 20. January 2017.
  - [51] MathWorks, “Implement generic battery model.” <https://se.mathworks.com/help/physmod/sps/powersys/ref/battery.html>. Retrieved 11. March 2017.
  - [52] M. Ahmed, “Modeling lithium-ion battery chargers in plects.” [https://www.plexim.com/sites/default/files/plecs\\_lithium\\_ion\\_adv.pdf](https://www.plexim.com/sites/default/files/plecs_lithium_ion_adv.pdf). Plexim Inc., Retrieved 7. March 2017.
  - [53] M. Chen and G. A. Rincon-Mora, “Accurate electrical battery model capable of predicting runtime and iv performance,” *IEEE transactions on energy conversion*, vol. 21, no. 2, pp. 504–511, 2006.

- [54] L. W. Yao, J. Aziz, P. Y. Kong, and N. Idris, "Modeling of lithium-ion battery using matlab/simulink," in *Industrial Electronics Society, IECON 2013-39th Annual Conference of the IEEE*, pp. 1729–1734, IEEE, 2013.
- [55] O. Erdinc, B. Vural, and M. Uzunoglu, "A dynamic lithium-ion battery model considering the effects of temperature and capacity fading," in *Clean Electrical Power, 2009 International Conference on*, pp. 383–386, IEEE, 2009.
- [56] O. Tremblay, L.-A. Dessaint, and A.-I. Dekkiche, "A generic battery model for the dynamic simulation of hybrid electric vehicles," in *Vehicle Power and Propulsion Conference, 2007. VPPC 2007. IEEE*, pp. 284–289, IEEE, 2007.
- [57] O. Tremblay and L.-A. Dessaint, "Experimental validation of a battery dynamic model for ev applications," *World Electric Vehicle Journal*, vol. 3, no. 1, pp. 1–10, 2009.
- [58] A. T. Gaugstad, "Power quality studies of a Stand-alone Wind-powered Water Injection System without physical inertia," Master Thesis, NTNU, February 2017.
- [59] Z. Xu, P. Yang, Q. Zheng, and Z. Zeng, "Study on black start strategy of microgrid with pv and multiple energy storage systems," in *Electrical Machines and Systems (ICEMS), 2015 18th International Conference on*, pp. 402–408, IEEE, 2015.
- [60] L. Xu, "Modeling, analysis and control of voltage-source converter in microgrids and hvdc," *IEEE*, 2013.
- [61] A. Haruni, A. Gargoom, M. E. Haque, and M. Negnevitsky, "Dynamic operation and control of a hybrid wind-diesel stand alone power systems," in *Applied Power Electronics Conference and Exposition (APEC), 2010 Twenty-Fifth Annual IEEE*, pp. 162–169, IEEE, 2010.
- [62] K. Uhlen, *Modelling and Robust Control of Autonomous Hybrid Power Systems*. PhD Thesis, NTNU, January 1994. Department of Engineering Cybernetics.
- [63] T. H. Syverud, "Modeling and control of a dc-grid hybrid power system with battery and variable speed diesel generators," Master Thesis, NTNU, 2016.
- [64] B. Zahedi, *Shipboard DC Hybrid Power Systems*. PhD Thesis, NTNU, October 2014. Department of Electric Power Engineering.
- [65] Ø. N. Smogeli, *Control of Marine Propellers - From Normal to Extreme Conditions*. PhD Thesis, NTNU, 2006. Department of Marine Technology.
- [66] S. Roy, O. P. Malik, and G. S. Hope, "A k-step predictive scheme for speed control of diesel driven power plants," *IEEE Transactions on Industry Applications*, vol. 29, pp. 389–396, Mar 1993.
- [67] D. W. Augustine and K. S. P. Kumar, "A method for self-tuning a pid controller for control of small to medium sized diesel engines," in *IEEE 1991 International Conference on Systems Engineering*, pp. 85–88, Aug 1991.

- [68] A. Cuculić, J. Ćelić, and R. Prenc, “Marine diesel-generator model for voltage and frequency variation analysis during fault scenarios,” *Pomorski zbornik*, vol. 51, no. 1, pp. 11–24, 2016.
- [69] L. Luo, L. Gao, and H. Fu, “The control and modeling of diesel generator set in electric propulsion ship,” *International Journal of Information Technology and Computer Science (IJITCS)*, vol. 3, no. 2, p. 31, 2011.
- [70] S. J. Chapman, *Electric Machinery Fundamentals*. McGraw-Hill, Fifth ed., 2012,. ISBN 978-007-108617-2.
- [71] P. Kundur, N. J. Balu, and M. G. Lauby, *Power system stability and control*, vol. 7. McGraw-hill New York, 1994.
- [72] J. D. Glover, M. S. Sarma, and T. Overbye, *Power System Analysis & Design, SI Version*. Cengage Learning, 2012.
- [73] IEEE, “Ieee recommended practice for excitation system models for power system stability studies,” tech. rep., Institute of Electrical and Electronics Engineers, 2006.
- [74] IEEE, “Ieee standard definitions for excitation systems for synchronous machines,” tech. rep., Institute of Electrical and Electronics Engineers, 1986.
- [75] MathWorks, “Building Your Own Drive.” <https://se.mathworks.com/help/physmod/sps/powersys/ug/building-your-own-drive.html>. Retrieved 10. May 2017.
- [76] M. Mirošević, “The dynamics of induction motor fed directly from the isolated electrical grid,” *INTECH Open Science Open Mind*, 2012.
- [77] A. Garces Ruiz, *Design, Operation and Control of Series-Connected Power Converters for Offshore Wind Parks*. Phd thesis, NTNU, 2012.
- [78] HES, “Harmonics.” <http://www.hersheyenergy.com/harmonics.html>. Hershey Energy Systems, Retrieved 20. April 2017.
- [79] MathWorks, “Emergency Diesel-Generator and Asynchronous Motor.” <https://se.mathworks.com/help/physmod/sps/examples/emergency-diesel-generator-and-asynchronous-motor.html>. Retrieved 30. May 2017.
- [80] E. Arrais, F. H. Nascimento, V. O. Roda, R. L. Ribeiro, T. O. Rocha, R. L. Barreto, and C. M. Neto, “Strategy control converter to enhance the performance in the grid-connected pmsg wind power generation system,” in *Power Electronics Conference and 1st Southern Power Electronics Conference (COBEP/SPEC), 2015 IEEE 13th Brazilian*, pp. 1–5, IEEE, 2015.
- [81] I. A. Ahmed, A. F. Zobaa, and G. A. Taylor, “Power quality issues of 3mw direct-driven pmsg wind turbine,” in *Power Engineering Conference (UPEC), 2015 50th*

- International Universities*, pp. 1–6, IEEE, 2015.
- [82] J. Barreiro, M. Hernandez, and G. Ramos, “Systematic evaluation for harmonic distortion limits from iee 519,” in *2013 Workshop on Power Electronics and Power Quality Applications (PEPQA)*, pp. 1–6, July 2013.
  - [83] ENERCON, “Enercon wind energy converters - technology & service.” [http://www.enercon.de/fileadmin/Redakteur/Medien-Portal/broschueren/pdf/EC\\_TuS\\_en\\_092016\\_web.pdf](http://www.enercon.de/fileadmin/Redakteur/Medien-Portal/broschueren/pdf/EC_TuS_en_092016_web.pdf), September 2016. ENERCON, Retrieved 8. June 2017.
  - [84] EWT, “Ewt dw 52 - 500 kw.” [http://www.ewtdirectwind.com/uploads/tx\\_rkdownloads/EWT\\_Flyer-DW-52500.pdf](http://www.ewtdirectwind.com/uploads/tx_rkdownloads/EWT_Flyer-DW-52500.pdf). EWT, Retrieved 8. June 2017.
  - [85] MathWorks, “Synchronous machine - base values.” <https://se.mathworks.com/help/phymod/sps/powersys/ref/synchronousmachine.html>. Retrieved 17. March 2017.
  - [86] O. Arrieta Orozco, *PID Control Servo/regulation performance and robustness issues*. Phd thesis, Universitat Autònoma de Barcelona, 2010.
  - [87] C. Bajracharya, M. Molinas, J. A. Suul, T. M. Undeland, *et al.*, “Understanding of tuning techniques of converter controllers for vsc-hvdc,” in *Nordic Workshop on Power and Industrial Electronics (NORPIE/2008), June 9-11, 2008, Espoo, Finland*, Helsinki University of Technology, 2008.
  - [88] J. W. Umland and M. Safiuddin, “Magnitude and symmetric optimum criterion for the design of linear control systems: What is it and how does it compare with the others?,” *IEEE Transactions on Industry Applications*, vol. 26, no. 3, pp. 489–497, 1990.
  - [89] J. G. Balchen, T. Andresen, and B. A. Foss, “Reguleringsteknikk,” *NTNU Trykk*, 2003.
  - [90] “Protection circuit model specification lithium iron phosphate battery pack.” <http://makspower.no/Userfiles/Upload/files/Makspower150ABMS.pdf>. Makspower Batteries, Retrieved 20. April 2017.
  - [91] P. Anderson and A. Bose, “Stability simulation of wind turbine systems,” *IEEE transactions on power apparatus and systems*, no. 12, pp. 3791–3795, 1983.
  - [92] X. Ma, D. Tian, Z. Zhang, Y. Deng, and Y. Li, “Combined wind speed model based on real wind data,” in *Renewable Power Generation (RPG 2015), International Conference on*, pp. 1–4, IET, 2015.



# Appendices

# A || The Park Transformation

This Appendix' chapter includes the main features of the mathematical background of the Park Transformation that is used. In all the transformations, it is assumed that the rotating frame is aligned with the  $a$ -axis. There are two main types of  $dq$  transforms, one voltage invariant and one power invariant. In this work, only the voltage invariant have been used [71]:

$$\begin{bmatrix} v_d \\ v_q \\ v_0 \end{bmatrix} = \frac{2}{3} \cdot \begin{bmatrix} \cos(\theta) & \cos(\theta - \frac{2\pi}{3}) & \cos(\theta + \frac{2\pi}{3}) \\ -\sin(\theta) & -\sin(\theta - \frac{2\pi}{3}) & -\sin(\theta + \frac{2\pi}{3}) \\ \frac{1}{2} & \frac{1}{2} & \frac{1}{2} \end{bmatrix} \cdot \begin{bmatrix} v_a \\ v_b \\ v_c \end{bmatrix} \quad (\text{A.1})$$

The inverse transformation is:

$$\begin{bmatrix} v_a \\ v_b \\ v_c \end{bmatrix} = \begin{bmatrix} \cos(\theta) & -\sin(\theta) & 1 \\ \cos(\theta - \frac{2\pi}{3}) & -\sin(\theta - \frac{2\pi}{3}) & 1 \\ \cos(\theta + \frac{2\pi}{3}) & -\sin(\theta + \frac{2\pi}{3}) & 1 \end{bmatrix} \cdot \begin{bmatrix} v_d \\ v_q \\ v_0 \end{bmatrix} \quad (\text{A.2})$$

These transformations also apply for currents and flux linkages as well. During balanced conditions, the 0-component is *zero*. It is therefore not included in any models in this thesis. The reason why this transformation is called voltage invariant is that the magnitude of  $v_d$  and  $v_q$  remain the same as the peak value of  $v_a$  for a balanced system [38]. The power invariant transformation is shown below:

$$\begin{bmatrix} v_d \\ v_q \\ v_0 \end{bmatrix} = \sqrt{\frac{2}{3}} \cdot \begin{bmatrix} \cos(\theta) & \cos(\theta - \frac{2\pi}{3}) & \cos(\theta + \frac{2\pi}{3}) \\ -\sin(\theta) & -\sin(\theta - \frac{2\pi}{3}) & -\sin(\theta + \frac{2\pi}{3}) \\ \frac{\sqrt{2}}{2} & \frac{\sqrt{2}}{2} & \frac{\sqrt{2}}{2} \end{bmatrix} \cdot \begin{bmatrix} v_a \\ v_b \\ v_c \end{bmatrix} \quad (\text{A.3})$$

with the inverse:

$$\begin{bmatrix} v_a \\ v_b \\ v_c \end{bmatrix} = \sqrt{\frac{2}{3}} \begin{bmatrix} \cos(\theta) & -\sin(\theta) & \frac{\sqrt{2}}{2} \\ \cos(\theta - \frac{2\pi}{3}) & -\sin(\theta - \frac{2\pi}{3}) & \frac{\sqrt{2}}{2} \\ \cos(\theta + \frac{2\pi}{3}) & -\sin(\theta + \frac{2\pi}{3}) & \frac{\sqrt{2}}{2} \end{bmatrix} \cdot \begin{bmatrix} v_d \\ v_q \\ v_0 \end{bmatrix} \quad (\text{A.4})$$



# B || Per-unit Calculation

Simulations are mainly performed on a per-unit basis throughout this thesis. Therefore, the underlying base values should be deduced in this chapter. As there is a transformer present in the system, two per-unit systems are needed as seen from Figure B.1.

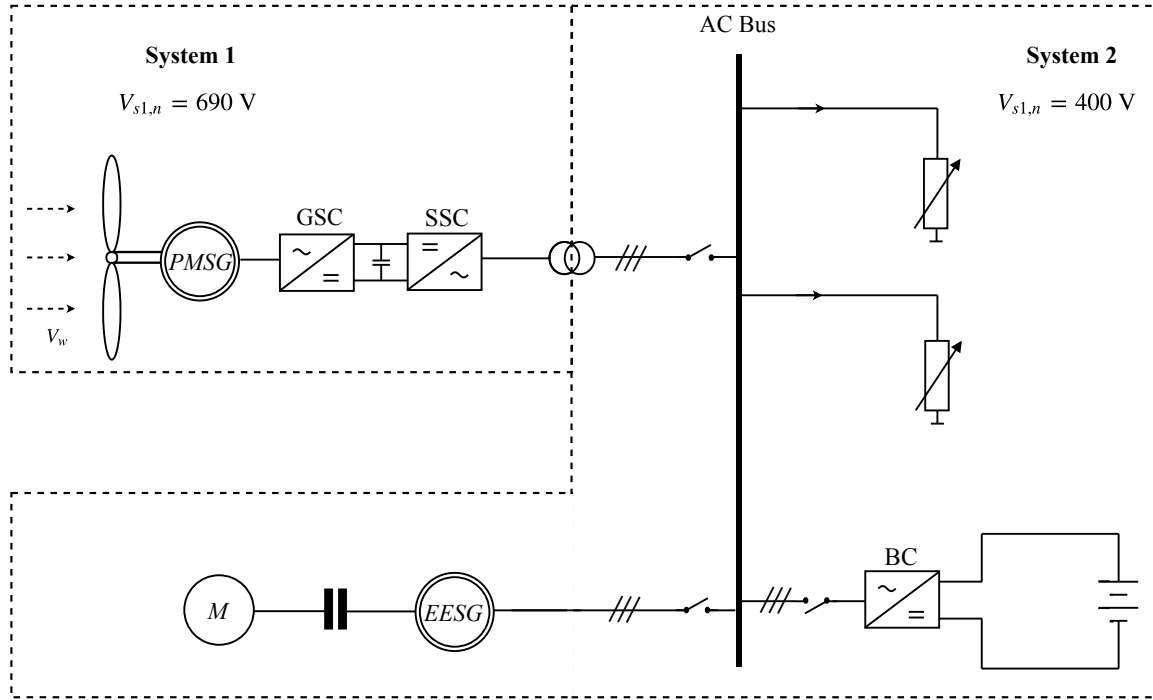


**Figure B.1:** Per-unit System Division

## B.1 Per-unit Calculation for System 1

The base values for this sub-system are retrieved from MathWorks' website on «Synchronous Machine» [85], because this describes the base values incorporated in the inbuilt synchronous machine equivalent that have been used as the turbine generator.

The stator base values are covered by equation (B.1):

$$\begin{aligned}
 S_{s1,base}^{3\phi} &= S_n \\
 V_{s1,base} &= \frac{\sqrt{2}}{\sqrt{3}} V_1 \\
 I_{s1,base} &= \frac{\sqrt{2}}{\sqrt{3}} \frac{S_n}{V_1} \\
 Z_{s1,base} &= \frac{V_{s1,base}}{I_{s1,base}} = \frac{V_1^2}{S_n} \\
 \omega_{s1,base} &= 2\pi f_n \\
 L_{s1,base} &= \frac{Z_{s1,base}}{\omega_{s1,base}}
 \end{aligned} \tag{B.1}$$

where,  $S_n$  is the three-phase nominal power [VA],  $V_1$  the nominal line-to-line voltage [V] and  $f_n$  is the nominal frequency [Hz]. For the particular synchronous generator, we have

$$\begin{aligned}
 S_n &= 250 \cdot 10^3 \text{ VA} \\
 V_1 &= 690 \text{ V} \\
 f_n &= 50 \text{ Hz}
 \end{aligned}$$

Inserting these values into equation (B.1) gives with two decimal precision:

$$\begin{aligned}
 S_{s1,base}^{3\phi} &= 250.00 \text{ kVA} & V_{s1,base} &= 563.38 \text{ V} \\
 I_{s1,base} &= 295.83 \text{ A} & Z_{s1,base} &= 1.90 \text{ } \Omega \\
 \omega_{s1,base} &= 100\pi \text{ rad/s} & L_{s1,base} &= 6.05 \text{ mH}
 \end{aligned}$$

## B.2 Per-unit Calculation for System 2

In the second and largest sub-system, the equations of (B.1) have been used as well. However, the nominal line-to-line voltage is 400 V and not 690 V here. This gives the following base values:

$$\begin{aligned}
 S_{s2,base}^{3\phi} &= 250.00 \text{ kVA} & V_{s2,base} &= 326.60 \text{ V} \\
 I_{s2,base} &= 510.31 \text{ A} & Z_{s2,base} &= 0.64 \text{ } \Omega \\
 \omega_{s2,base} &= 100\pi \text{ rad/s} & L_{s2,base} &= 2.04 \text{ mH}
 \end{aligned}$$

# C || Tuning of PI Controllers

Most of the controllers described in this thesis use Proportional - Integral (PI) controllers in one way or another. Therefore it seems natural to elaborate on the working principles and tuning of this type of controller, as they play a central role for the system dynamics. Equation (C.1) shows the transfer function of the general PI controller:

$$H(s) = K_{pi} \frac{1 + T_{ii}s}{T_{ii}s} \quad (C.1)$$

Here,  $K_{pi}$  is the proportional gain and  $T_{ii}$  is the integral time [86]. These two parameters are correlated, meaning that they have to be tuned together in order to obtain satisfactory behaviour of the controller. Two well-known tuning criteria have been used, namely the modulus optimum and symmetrical optimum. A brief explanation of these will be given in the next two sections. The controllers described in sections consists of a cascade control structure. This kind of alignment requires the speed of response to increase towards the inner loop [87]. Most of the controllers include an inner loop with fast response, and one outer loop designed to achieve proper regulation and stability. Hence, the inner loop is tuned according to the «modulus optimum» strategy because of its fast response and simplicity, whereas the outer loop is tuned according to the «symmetrical optimum».

It should be noted that not all of the controllers are tuned according to these criteria. This is due to nonlinear properties of the system that cannot be assumed negligible, e.g. when the controller depends on the aerodynamics of the system (ref (3.3)). As references for the tuning process, [87], [16], [58] and [88] have been utilised. Some of the key elements from these are summarised.

## C.1 Modulus Optimum

The modulus optimum criterion is applicable when the open-loop transfer function of the inner controller is given by equation (C.2). This is also shown in a block diagram in Figure C.1.

$$G(s) = K_{pi} \frac{1 + T_{ii}s}{T_{ii}s} \cdot \frac{K_{1m}}{1 + T_{1m}s} \cdot \frac{1}{1 + T_{2m}s} \quad (C.2)$$

Further, it is assumed that the time constant  $T_{1m}$  is significantly larger than  $T_{2m}$ . The objective of the PI controller is to eliminate the dominant pole of  $T_{1m}$ . Hence, the optimal tuning criteria is given by:

$$\begin{aligned} T_{ii} &= T_{1m} \\ K_{pi} &= \frac{T_{1m}}{2 \cdot K_{1m} \cdot T_{2m}} \end{aligned} \quad (C.3)$$

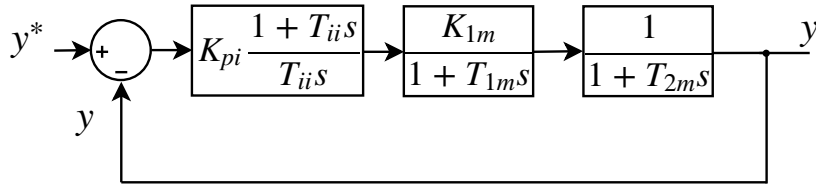


**Figure C.1:** Modulus Optimum Transfer Function

## C.2 Symmetrical Optimum

In the previous section, it was seen that modulus optimum is applicable whenever there is one dominant pole present in the open-loop transfer function. However, the outer control loop often involves one or more integrators, as shown in Figure C.2. Such systems have poles at the origin, and will thus worsen the phase margin - or in other words - the stability of the system. If the modulus optimum had been used on this transfer function, the system would be unstable. Thus, another method has to be used.

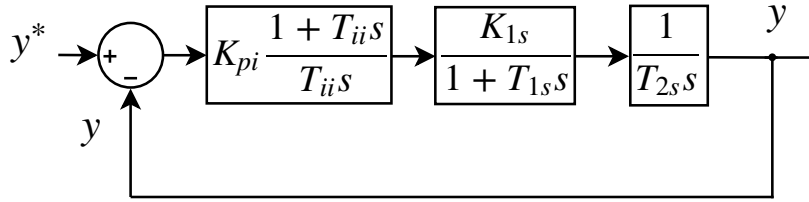


**Figure C.2:** Symmetrical Optimum Transfer Function

The main idea behind the symmetrical optimum criterion is to tune  $T_{ii}$ , so that the PI controller's pole lifts the phase of the closed-loop transfer function *before* it is decreased by  $T_{1s}$ . The symmetrical optimum strategy obtains a controller that maximises the phase margin, hence optimises the system response to disturbances. This implies that the system can tolerate more delays. The tuning criterion becomes:

$$\begin{aligned} T_{ii} &= \alpha^2 T_{1s} \\ K_{pi} &= \frac{T_{2s}}{\alpha \cdot K_{1s} \cdot T_{1s}} \end{aligned} \quad (C.4)$$

In equation (C.4),  $\alpha$  is a constant which determines the poles of the closed-loop transfer function of the system:

$$\alpha \begin{cases} < 3 & \implies \text{complex conjugated poles} \\ = 3 & \implies \text{real and equal poles} \\ > 3 & \implies \text{real and distinct poles} \end{cases} \quad (C.5)$$

In the thesis,  $\alpha = 3$  have been chosen.

# D || Tuning of the System Controllers

In this chapter, the tuning of the PI controllers is explained. First, the values obtained by applying the modulus optimum and symmetrical optimum criteria are shown, before the actual values that have been used in the simulations are given together with a brief argumentation.

## D.1 SSC Inner Current Controller

The open loop transfer function for the SSC current controller is given by [87]:

$$h_{0,SSC}(s) = \underbrace{K_{pi} \frac{1 + T_{ii}s}{T_{ii}s}}_{\text{PI Controller}} \cdot \underbrace{\frac{\omega_e T_1}{X_{filter}(1 + T_1 s)}}_{\text{PCC Transfer Function}} \cdot \underbrace{\frac{1}{1 + T_e s}}_{\text{PWM}} \quad (\text{D.1})$$

It is observed from equation (D.1) that the open loop transfer function only contains one integrator. Hence, the modulus optimum criterion can be applied for tuning of the inner current controller:

$$\begin{aligned} T_{ii} &= T_1 = \frac{X_{filter}}{\omega_e \cdot R_{filter}} \\ K_{pi} &= \frac{T_1}{2 \cdot K_1 \cdot T_e} \end{aligned} \quad (\text{D.2})$$

Here,  $X_{filter} = \omega_e L_{filter}$  and  $R_{filter}$  are the per-unit values of the the RL-filter connected between the SSC and the step-down transformer.  $T_e = 1.5 \cdot T_x$  is the equivalent analogue-to-digital time constant for the PWM, described in Section 3.3, and  $K_1 = 1/R_{filter}$ . Inserting values gives for the SSC:

$$\begin{aligned} T_{ii} &= \frac{X_{filter}}{\omega_e \cdot R_{filter}} = 0.017 \\ K_{pi} &= \frac{L_{filter}}{2 \cdot T_e} = 4.2441 \end{aligned} \quad (\text{D.3})$$

A step response has been carried out for the current controller, by setting the DC-side voltage of the SSC to a fixed value and connecting the AC-side to an infinite bus. The resulting response is shown in Figure D.1. It is observed that both  $i_d$  and  $i_q$  reacts swiftly, and without overshoot, to changes in their respective references. The cross-coupling between the  $d$  and  $q$  component is also visible: When a step is applied to  $i_d$  after 0.05 seconds, a small positive deflection is observed in  $i_q$ . The same phenomena is seen in  $i_d$  when a step is applied at  $t = 0.1$  seconds.

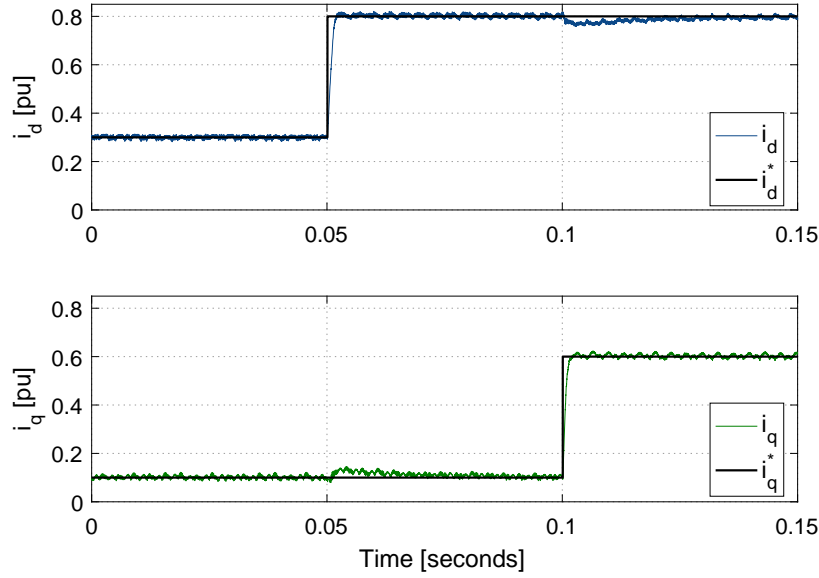


**Figure D.1:** Step Response for Current Controller

A Nichols diagram (Figure D.2) have been provided to assess the controller stability and robustness. Two of the variables assessed are the phase margin ( $\psi$ ) and the gain margin ( $\Delta K$ ). Briefly put, the phase margin is found as  $180^\circ$  minus the open-loop phase angle at the point where the open-loop gain crosses the 0 dB line. A rule of thumb is that this should be larger than  $45^\circ$  for the controller to be sufficiently stable [89]. In Figure D.2 the phase margin has been highlighted as a red line. Considering the gain margin, this is the difference between the 0 dB line and the open-loop gain at the frequency where open-loop phase crosses  $-180^\circ$ . Thus, the analysis of the current controller results in a phase margin of  $65.5^\circ$  and an infinite gain margin, as the phase is asymptotically approaching  $-180^\circ$ . The controller is therefore considered stable.

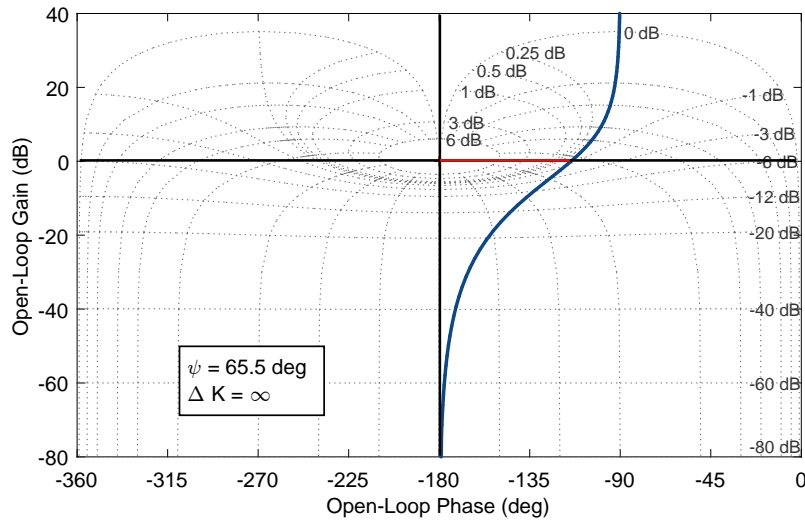


**Figure D.2:** Nichols Diagram for Current Controller

## D.2 GSC Inner Current Controller

The open-loop transfer function of the GSC current controller is equivalent to equation (D.1), but with the PMSG stator resistance and reactance instead of the filter values. Thus,

$$h_{0,GSC}(s) = \underbrace{K_{pi} \frac{1 + T_{ii}s}{T_{ii}s}}_{\text{PI Controller}} \cdot \underbrace{\frac{\omega_e T_2}{X_s(1 + T_2 s)}}_{\text{PMSG Transfer Function}} \cdot \underbrace{\frac{1}{1 + T_e s}}_{\text{PWM}} \quad (\text{D.4})$$

The modulus optimum criterion is applicable, and gives:

$$\begin{aligned} T_{ii} &= \frac{X_s}{\omega_e \cdot R_s} = 0.017 \\ K_{pi} &= \frac{L_s}{2 \cdot T_e} = 12.7324 \end{aligned} \quad (\text{D.5})$$

## D.3 Pitch Angle Controller

The open-loop transfer function of the pitch controller is given in equation (D.6)

$$h_{0,P}(s) = \underbrace{K_{pi} \frac{1 + T_{ii}s}{T_{ii}s}}_{\text{PI Controller}} \cdot \underbrace{\frac{0.5 \cdot \rho \cdot A \cdot C_p(\lambda, \beta) \cdot V_W^3}{\omega_{mech}}}_{\text{Transfer Function from } \tau_{mech} \text{ to } \beta} \cdot \underbrace{\frac{1}{Hs}}_{\text{Physics}} \quad (\text{D.6})$$

From this equation, it is evident that there are strong nonlinearities present, hence neither modulus optimum nor symmetrical optimum is applicable. Instead, the integral time and proportional gain of the pitch angle controller have been found through several simulations made in [16]. The values that are found to be adequate is:

$$\begin{aligned} T_{ii} &= 0.2 \\ K_{pi} &= 5 \end{aligned} \quad (\text{D.7})$$

The Nichols plot in Figure D.3 reveals a phase margin of 90° and an infinite gain margin. The pitch controller thus satisfies the recommended stability criteria.

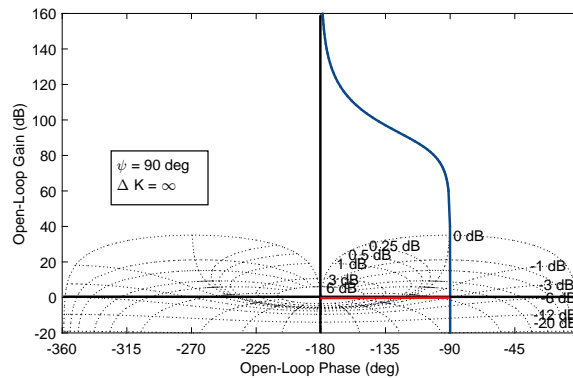


**Figure D.3:** Nichols Diagram for Pitch Controller

## D.4 GSC Speed Controller

Due to nonlinearities introduced by the wind turbine aerodynamics, the speed controller has to be tuned through simulations. The workings in [58] and [16] have simulated this thoroughly, and concludes that a low PI controller gain,  $K_{pi}$ , yields lower power fluctuations and low speed overshoot, but decreases the ability to follow the speed reference. The same is the situation with high integral times,  $T_{ii}$ . Thus, high  $K_{pi}$  and low  $T_{ii}$  allows fast speed tracking but comes at the price of higher power fluctuations. There is obviously a trade-off between speed and power fluctuations. Figure D.4 is taken from [16], and shows this principle. Here,  $K_{\omega}$  is the proportional gain and  $T_{\omega}$  the integral time.

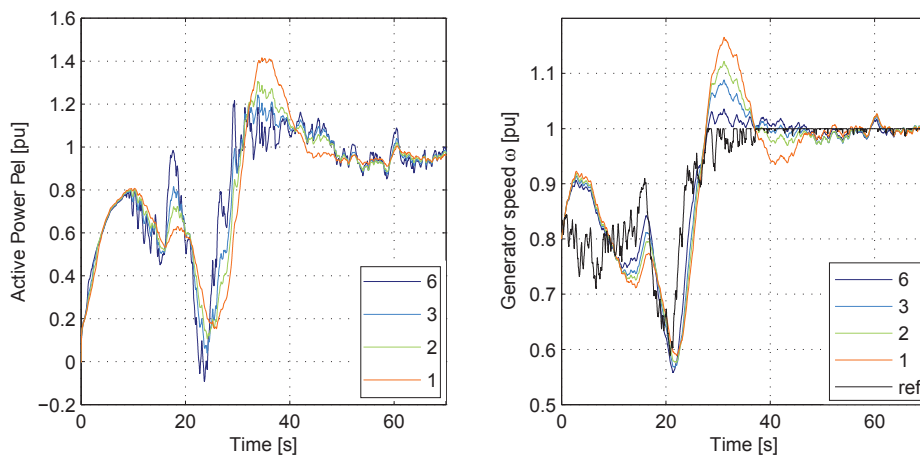


Fig. C.2: Varying  $K_{\omega}$  with  $T_{\omega} = 1$

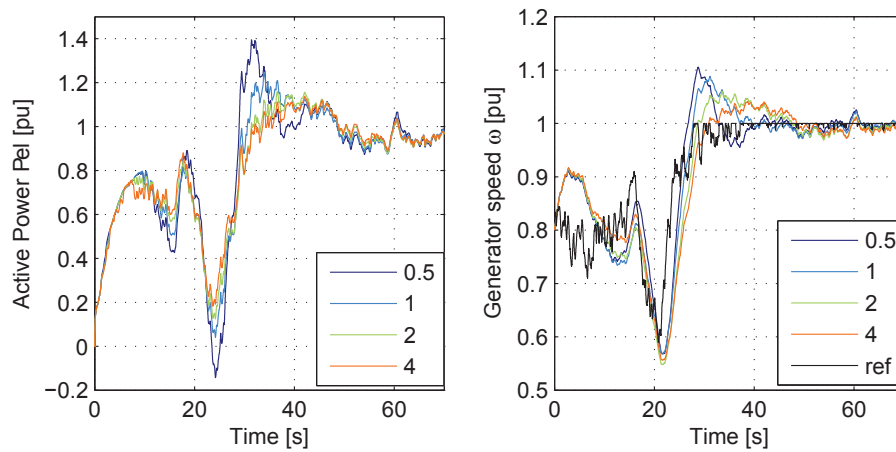


Fig. C.3: Varying  $T_{\omega}$  with  $K_{\omega} = 3$

**Figure D.4:** Simulations with Varying Gain and Integral Time

Based on the simulations, the values that have been found adequate are:

$$\begin{aligned} T_{ii} &= 4 \\ K_{pi} &= 4 \end{aligned} \tag{D.8}$$



## D.5 SSC DC-Link Voltage Controller

The open loop transfer function of the DC-Link voltage controller is given in equation (D.9)

$$h_{0,DC}(s) = \underbrace{K_{pi} \frac{1 + T_{ii}s}{T_{ii}s}}_{\text{PI Controller}} \cdot \underbrace{\frac{V_d}{V_{dc}(1 + T_3s)} \cdot \frac{1}{T_{dc}s}}_{\text{DC-Link Dynamics}} \quad (\text{D.9})$$

The symmetrical optimum criterion is applied for this controller.

$$\begin{aligned} T_{ii} &= \alpha^2 \cdot T_3 \\ K_{pi} &= \frac{T_{dc}}{\alpha \cdot K_3 \cdot T_3} \end{aligned} \quad (\text{D.10})$$

Here  $T_3 = 2 \cdot T_e$  is the first order time constant for the inner current loop and  $T_{dc} = 1/(\omega_e C)$  the time constant of the DC-Link capacitor. Inserting values yields:

$$\begin{aligned} T_{ii} &= 0.0054 \\ K_{pi} &= 5.7564 \end{aligned} \quad (\text{D.11})$$

The Nichols diagram in Figure D.5 shows a sufficient phase margin of  $53.1^\circ$  and an infinite gain margin.

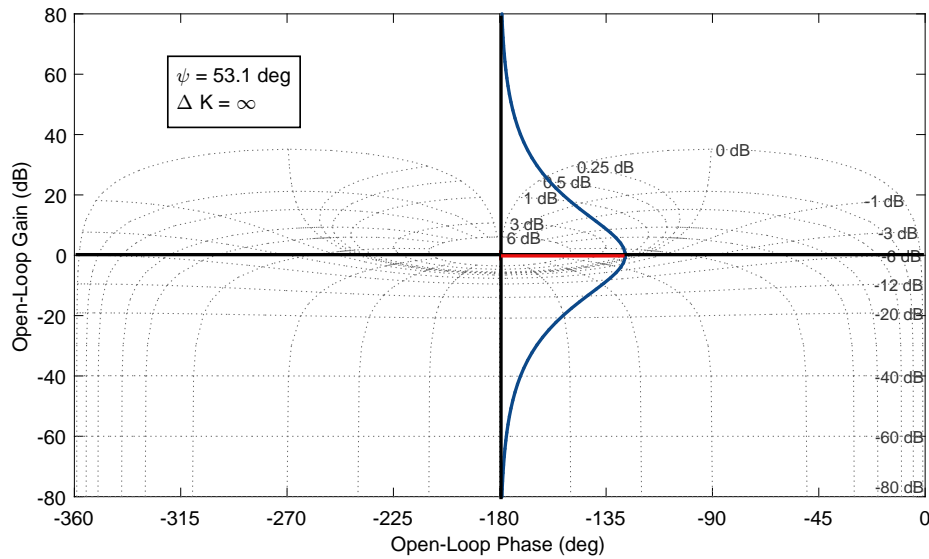


**Figure D.5:** Nichols Diagram for DC-Link Voltage Controller

## D.6 SSC Reactive Power Controller

The open loop transfer function of the reactive power controller is given in equation (D.12).

$$h_{0,Q}(s) = \underbrace{K_{pi} \frac{1 + T_{ii}s}{T_{ii}s}}_{\text{PI Controller}} \cdot \underbrace{\frac{1/R_{filter}}{1 + T_4s}}_{\text{Physics}} \cdot \underbrace{\frac{1}{1 + T_e s}}_{\text{PWM}} \quad (\text{D.12})$$

Thus, the modulus optimum criterion seems applicable. However, analysing the controller in a Nichols diagram reveals an open-loop phase of  $-180^\circ$  for frequencies almost up to the crossover frequency of the inner current loop. Therefore, the symmetrical optimum criterion is applied for this controller instead.

$$\begin{aligned} T_{ii} &= \alpha^2 \cdot T_e \\ K_{pi} &= \frac{T_4 \cdot R_{filter}}{\alpha \cdot T_e} \end{aligned} \quad (\text{D.13})$$

Here  $T_4 = L_{filter}/R_{filter}$  is the first order time constant for the inner current loop. Inserting values gives:

$$\begin{aligned} T_{ii} &= 0.0054 \\ K_{pi} &= 444.4444 \end{aligned} \quad (\text{D.14})$$

Similarly to the Nichols diagram for the DC-Link voltage controller, the reactive power controller has a phase margin of  $53.1^\circ$  and an infinite gain margin (Figure D.6). However, it is observed that the open-loop phase of this controller is better ( $-90^\circ$ ) at low frequencies, compared to the voltage controller.

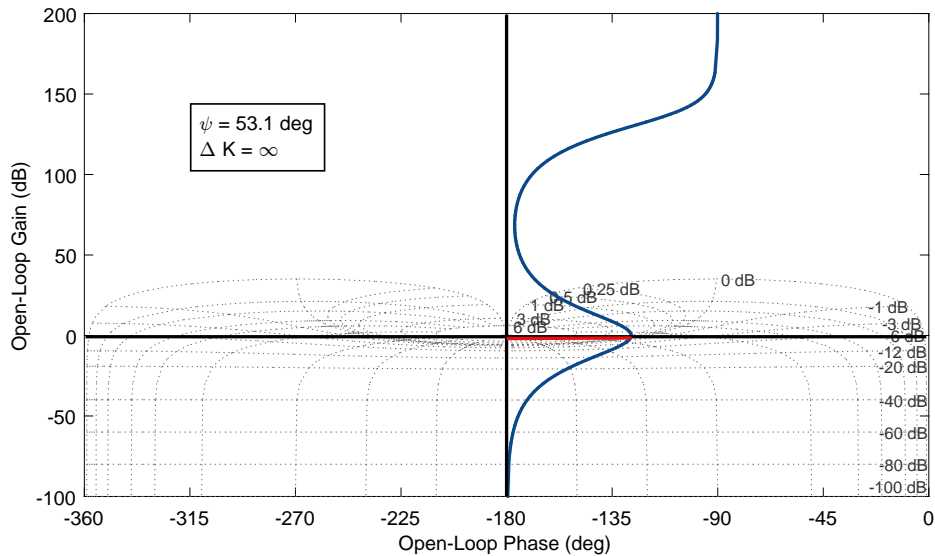


**Figure D.6:** Nichols Diagram for Reactive Power Controller

## D.7 Battery Converter Controller

The tuning of the battery controller is similar to the inner current controllers described in Appendix D.1 and D.2. This means that the open loop transfer function of the is given by equation (D.12).

$$h_{0,bat}(s) = \underbrace{K_{pi} \frac{1 + T_{ii}s}{T_{ii}s}}_{\text{PI Controller}} \cdot \underbrace{\frac{\omega_e T_5}{X_{filter,b}(1 + T_5s)}}_{\text{PCC Transfer Function}} \cdot \underbrace{\frac{1}{1 + T_e s}}_{\text{PWM}} \quad (\text{D.15})$$

It is observed from equation (D.1) that the open loop transfer function only contains one integrator. Hence, the modulus optimum criterion can be applied for tuning of the inner current controller:

$$\begin{aligned} T_{ii} &= T_5 = \frac{X_{filter,b}}{\omega_e \cdot R_{filter,b}} \\ K_{pi} &= \frac{T_5}{2 \cdot K_5 \cdot T_e} \end{aligned} \quad (\text{D.16})$$

with  $T_5 = 1/R_{filter,b}$ . Inserting values gives:

$$\begin{aligned} T_{ii} &= 0.0170 \\ K_{pi} &= 4.2441 \end{aligned} \quad (\text{D.17})$$

A step response, equivalent to the one performed in Appendix D.1, has been performed. This can be seen from Figure D.7. The simulation shows similar behaviour, but the signals of  $v_d$  and  $v_q$  contain more noise. Also, the response is swift and without overshoot, but the settling times is somewhat slower than in the SSC and GSC current controllers.

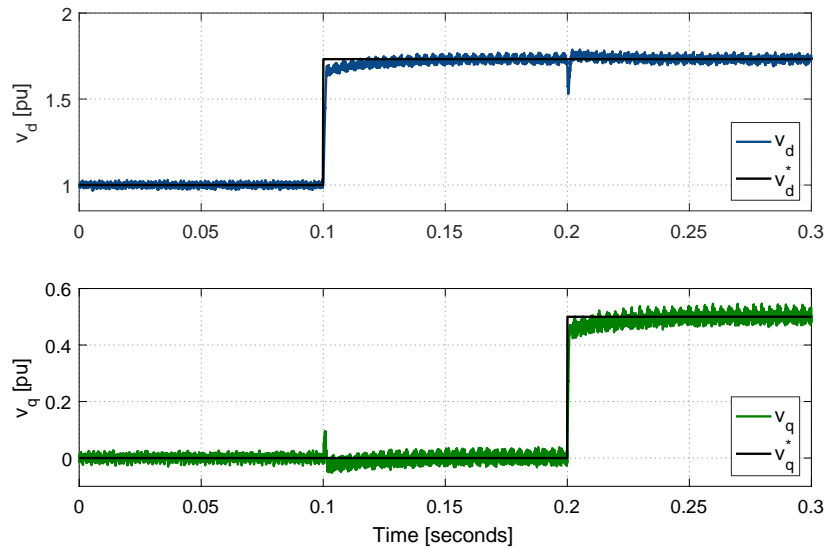


**Figure D.7:** Step Response for Battery Controller

# E || Derivation of Battery Parameters

This chapter includes additional information on the battery model parameters. We have the following relationship for the constants  $\mu_v$ ,  $\mu_c$ ,  $\rho$  and  $E_0$ :

$$\begin{aligned}\mu_v &= V_b^{full} - V_b^{exp} \\ \mu_c &= \frac{3}{q_{exp}} \\ \rho &= \frac{V_b^{full} - V_b^{nom} + \mu_v \cdot (e^{-\mu_c \cdot q_{nom}}) \cdot (\xi_{max} - q_{nom})}{q_{nom}} \\ E_0 &= V_b^{full} + \rho + R_b \cdot i_{1C} - \mu_v\end{aligned}\tag{E.1}$$

Here, for a single LFP battery [90]:

**Table E.1:** Overview of Single LFP Characteristics

Parameter	Value	Description
$V_b^{full}$	3.70 V	Voltage when fully charged
$V_b^{exp}$	3.40 V	Voltage at end of the exponential zone
$q_{exp}$	0.23 Ah	Charge depleted at end of the exponential zone
$V_b^{nom}$	3.22 V	Voltage at end of the nominal zone
$q_{nom}$	2.30 Ah	Charge depleted at end of the nominal zone
$i_{1C}$	2.30 A	Current at 1C rate
$R_b$	10.0 m $\Omega$	Battery internal resistance

However, the battery used is not a single battery, but multiple batteries connected in both parallel and series to get the right amount of power capability and energy capacity. Thus:

$$\begin{aligned}V_{full,pack} &= N_{series} \cdot V_b^{full} \\ V_{nom,pack} &= N_{series} \cdot V_b^{nom} \\ V_{exp,pack} &= N_{series} \cdot V_b^{exp} \\ q_{nom,pack} &= N_{parallel} \cdot q_{nom} \\ q_{exp,pack} &= N_{parallel} \cdot q_{exp} \\ i_{1C,pack} &= N_{parallel} \cdot i_{1C} \\ R_{pack} &= \frac{N_{series}}{N_{parallel}} \cdot R_b\end{aligned}\tag{E.2}$$

In this thesis,  $N_{series} = 290$  and  $N_{parallel} = 44$  is used.

# F || Additional System Parameters

This chapter includes the most relevant additional parameters for the Wind Turbine System, BESS, DG, DG Control and the IMs. All the reactances are unsaturated.

**Table F.1:** Additional PMSG and Wind System Parameters

Parameter	Symbol	Value
Number of Poles	$P$	230
System Side Filter Resistance	$R_{filter}$	0.15 pu
System Side Filter Reactance	$X_{filter}$	0.8 pu
DC-link Capacitor	$C_{dc}$	1.3 pu
Permanent Magnet Flux	$\Phi_{pm}$	1.5 Wb
Transformer Ratio	$N_1 : N_2$	690:400 V
Transformer Resistance	$R_T$	0.002 pu
Transformer Reactance	$X_T$	0.08 pu

**Table F.2:** Additional Battery Parameters

Parameter	Symbol	Value
Initial SOC	$SOC(0)$	60 %
Battery Response Time	$T_b$	0.1 s
Voltage at Full Charge	$V_{b,max}$	1148 V
Internal Resistance	$R_b$	98.6 m $\Omega$

**Table F.3:** Additional Diesel Generator Parameters

Parameter	Symbol	Value
Total Inertia	$H_{dg}$	0.7 s
Generator Number of Poles	$P$	40

**Table F.4:** DG Governor Control Parameters

Parameter	Symbol	Value
Controller Gain	$K_{pc}$	40
Controller Time Constant	$T_{1c}$	0.01 s
Controller Time Constant	$T_{2c}$	$2 \cdot 10^{-4}$ s
Controller Time Constant	$T_{3c}$	0.1 s
Actuator Time Constant	$T_{1a}$	0.25 s
Actuator Time Constant	$T_{2a}$	$9 \cdot 10^{-3}$ s
Actuator Time Constant	$T_{3a}$	0.0384 s
Engine Time Delay	$T$	0.024 s

**Table F.5:** DG AC5A Exciter Parameters

Parameter	Symbol	Value
Low-pass Filter Constant	$T_r$	$20 \cdot 10^{-3}$
Regulator Gain	$K_1$	500
Regulator Time Constant	$T_1$	0.02 s
Regulator Max Limit	$V_{max}$	7.3 V
Regulator Min Limit	$V_{min}$	-7.3 V
Damping Filter Gain	$K_2$	0.03
Damping Filter Time Constant	$T_2$	1 s
Damping Filter Time Constant	$T_3$	0 s
Damping Filter Time Constant	$T_4$	0 s
Exciter Gain	$K_E$	1
Exciter Time Constant	$T_E$	0.02 s

**Table F.6:** Feed Blower IM General Parameters

Parameter	Symbol	Value
Stator Resistance	$R_{s,im}$	87 m $\Omega$
Stator Inductance	$X_{s,im}$	0.8 mH
Rotor Resistance	$R_{r,im}$	228 m $\Omega$
Rotor Inductance	$X_{r,im}$	0.8 mH
Mutual Inductance	$L_{m,im}$	35.4 mH
Inertia	$J_{im}$	1.662 kg $\cdot$ m <sup>2</sup>
Poles	$P$	4

**Table F.7:** Fixed-Speed IM General Parameters

Parameter	Symbol	Value
Stator Resistance	$R_{s,im}$	$19.65 \cdot 10^{-3}$ pu
Stator Inductance	$X_{s,im}$	$39.7 \cdot 10^{-3}$ pu
Rotor Resistance	$R_{r,im}$	$19.09 \cdot 10^{-3}$ pu
Rotor Inductance	$X_{r,im}$	$39.7 \cdot 10^{-3}$ pu
Mutual Inductance	$L_{m,im}$	$1.354 \cdot 10^{-3}$ pu
Inertia	$J_{im}$	0.6 s
Poles	$P$	4

# G || Additional Plots

## G.1 Wind Turbine GSC

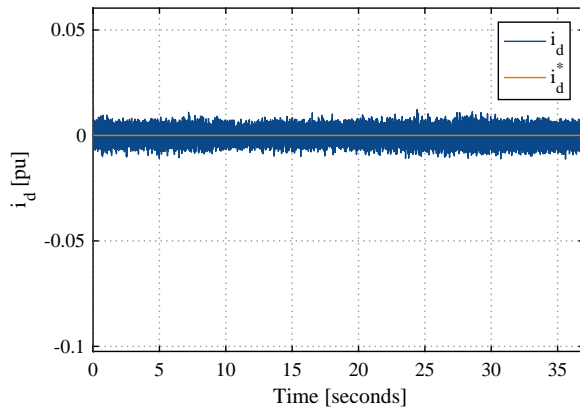


Figure G.1: GSC Current Control,  $i_d$

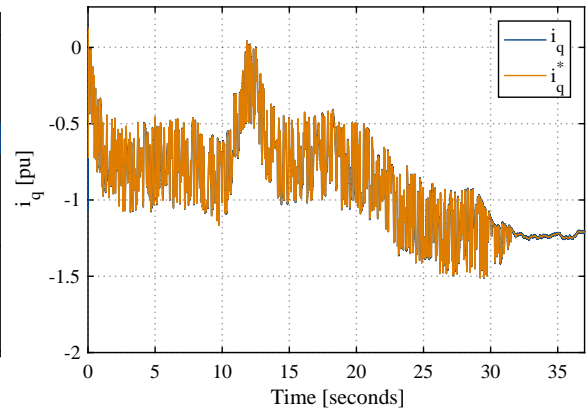


Figure G.2: GSC Current Control,  $i_q$

## G.2 Wind Turbine SSC

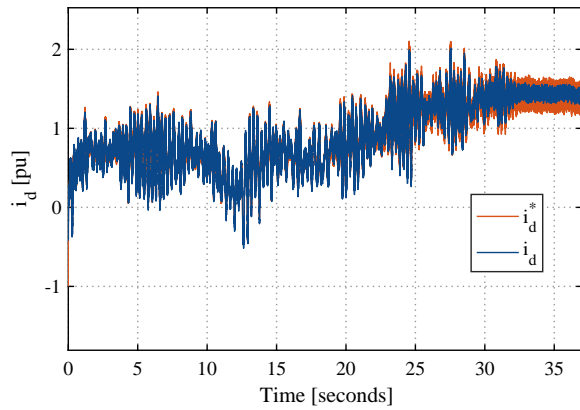


Figure G.3: SSC Current Control,  $i_d$

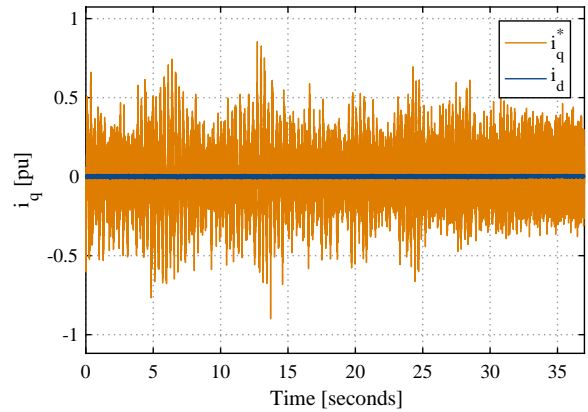
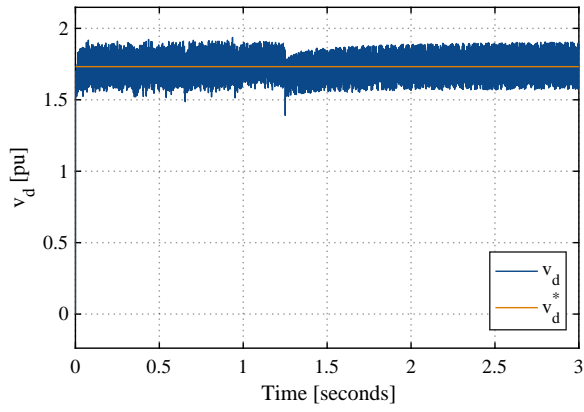
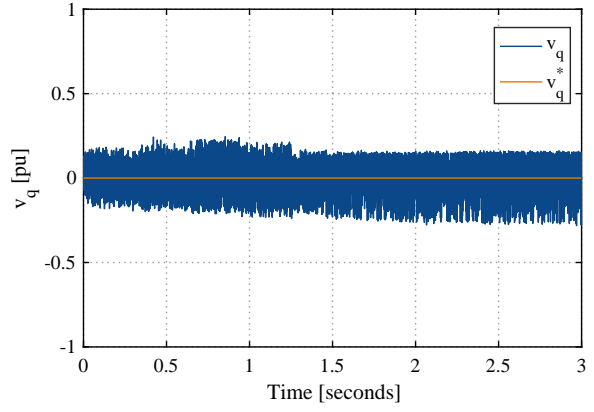


Figure G.4: SSC Current Control,  $i_q$

### G.3 Battery System Control



**Figure G.5:** Battery Control,  $v_d$



**Figure G.6:** Battery Control,  $v_q$



# H || IEC-61892 Standard

The table is obtained from [16] and summarises some of the key points from the IEC-61892 Standard.

**Table H.1:** Extraction of Relevant IEC-61892 Data

<b>Parameter</b>	<b>Limits [pu]</b>
Frequency (transient)	0.9-1.1
Frequency (stationary)	0.95-1.05
Voltage (transient)	0.8-1.2
Voltage (stationary)	0.9-1.06

# I || Wind Profile Model

The wind profile that is used for the simulation in Chapter 4 is based on the techniques presented in [91] and [92]. The profile aims to reflect a realistic wind profile for the proposed location, and also include *low*, *medium* and *high* wind speeds relative to the turbine rating. A MATLAB<sup>®</sup> code creating the wind profile used in Section 4.1 is shown below.

```
%%%%%%%%%%%%%%%%%%%%%%%%%%%%%%%%%%%%%%%%%%%%%%%%%%%%%%%%%%%%%%%%%%%%%%%%%%%%%%
% Make wind speed
%%%%%%%%%%%%%%%%%%%%%%%%%%%%%%%%%%%%%%%%%%%%%%%%%%%%%%%%%%%%%%%%%%%%%%%%%%%%%%

clear;
clc;

% General parameters
winit = 5.7; % Initial wind speed [m/s]
Tstart = 0;
Tend = 40;
timevec = linspace(0,40,1000);

% Mean wind speed
vw = 5.7; % Mean wind speed [m/s]

% Ramp component
Tsr = 17; % Ramp start time [s]
Ter = 36; % Ramp end time [s]
Ar = 10.3-vw; % Ramp amplitude [m/s]

% Gust component
Tsg = 8; % Gust start time [s]
Teg = 13; % Gust end time [s]
Ag = -0.5; % Gust amplitude [m/s]
Dg = Teg-Tsg; % Gust duration [s]

% Turbulence component
h = 50; % Nacelle height [m]
l = 600; % Turbulence length scale [m]
z0 = 1e-3; % Roughness length [m]
N = 250;
Sf = zeros(1,N);
Δw = 10;
Δt = 1.75;
T = Δt*N;

% Initialising variables
vwvec = zeros(1,length(timevec));
vrvec = zeros(1,length(timevec));
vgvec = zeros(1,length(timevec));
vtvec = zeros(1,length(timevec));
```

```

sumvec = zeros(1,length(timevec));
vtot = zeros(1,length(timevec));

for k = 1:1000
    vwvec(1,k) = vw;
    t = timevec(1,k);

    if (t ≥ Tsr && t ≤ Ter)
        vrvec(1,k) = Ar*(1 - (t-Ter)/(Tsr-Ter));
    end

    if (t ≥ Tsg && t ≤ Teg)
        vgvec(1,k) = Ag*(1-cos(2*pi*(t/Dg - Tsg/Dg)));
    end

    if (t > Ter)
        vwvec(1,k) = 10.3;
    end

    for i = 1:N
        phi = 2*pi*rand();
        freq = ((i-1)/2)*Δw;
        Sf(1,i) = ((1/log(h/z0)^2)*l*vw)/((1+(1.5*freq*l/vw))^(5/3));
        sumvec(1,i) = sqrt(2*Sf(1,i)/T)*cos(freq*t+phi);
    end

    vtvec(1,k) = sum(sumvec);
    vtot(1,k) = vwvec(1,k) + vrvec(1,k) + vgvec(1,k) + vtvec(1,k);
end

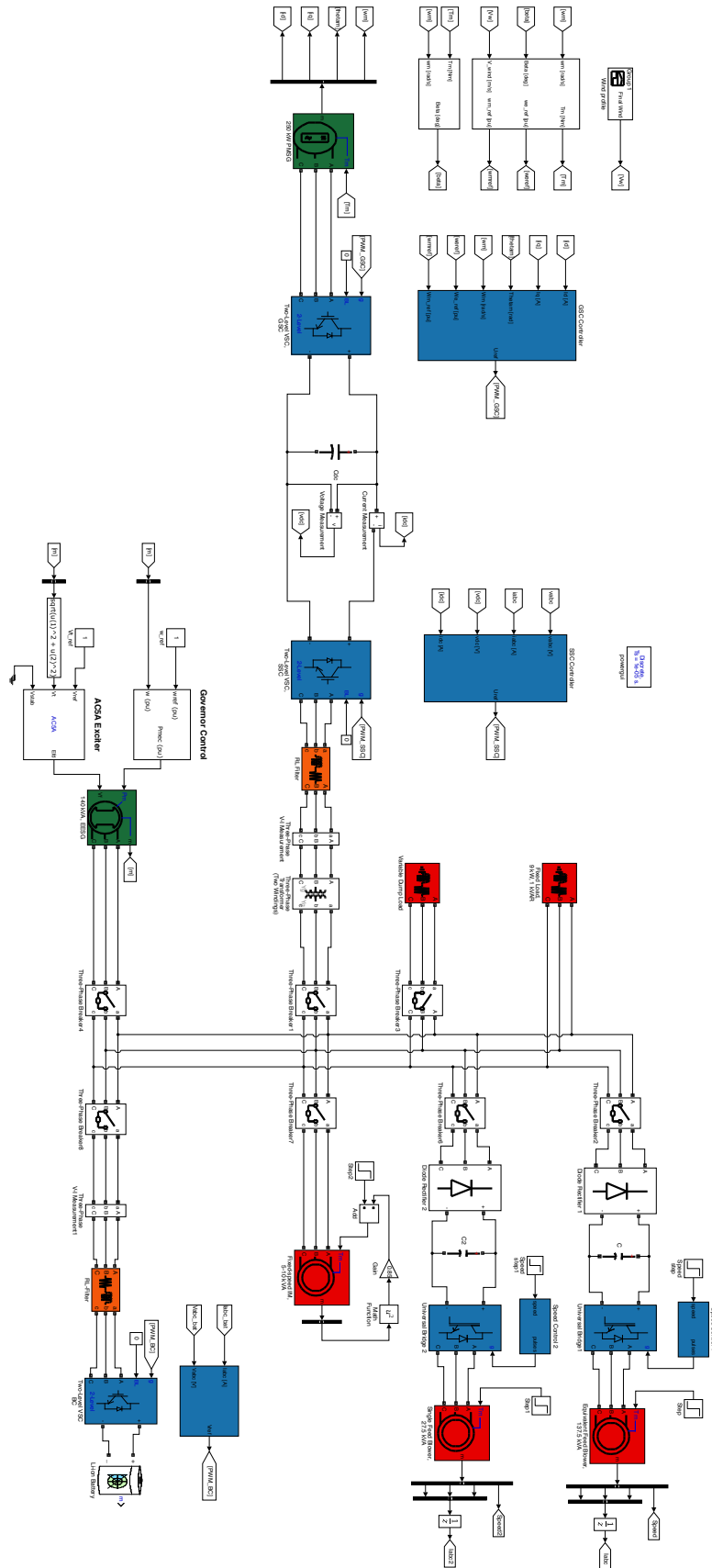
plot(timevec,vtot);
grid on;
ylim([2,12]);

```

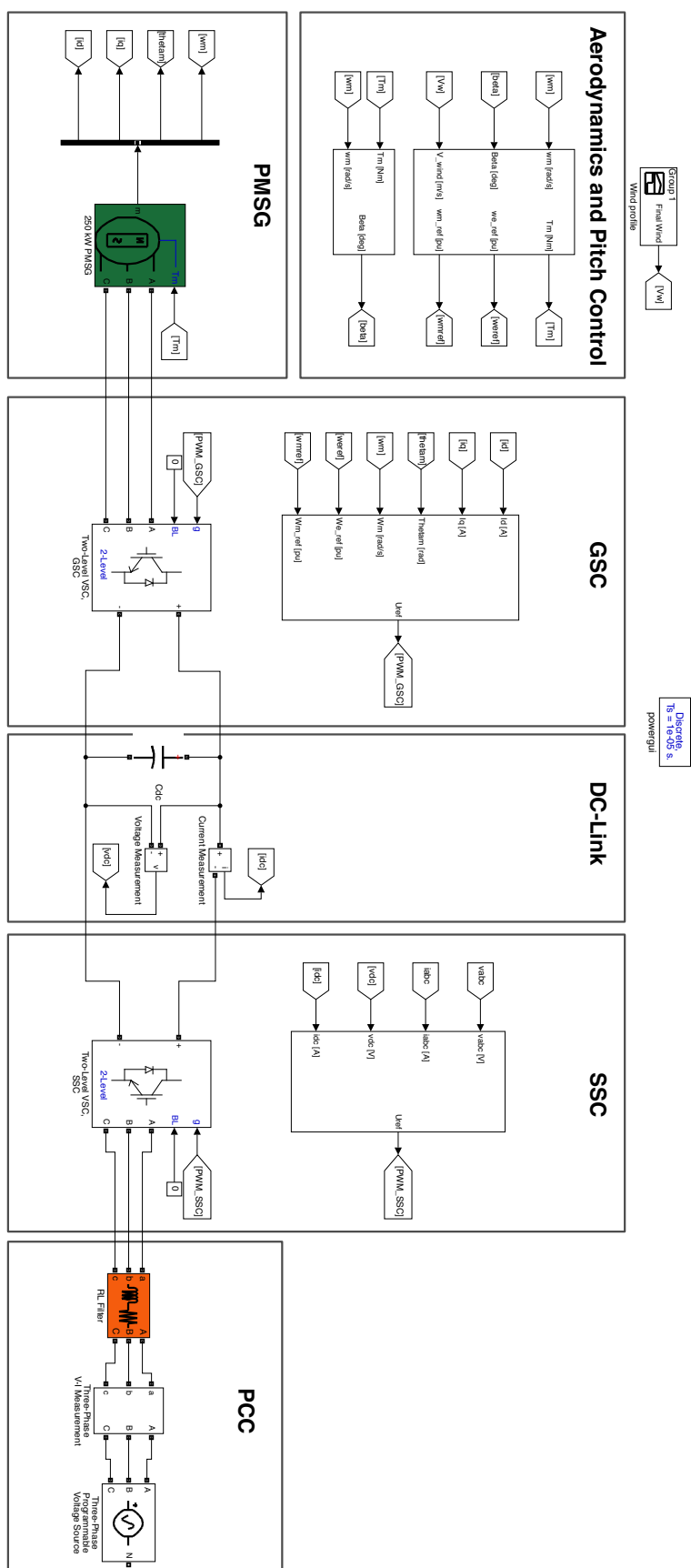
# J || The MATLAB<sup>®</sup>/Simulink Model

This chapter contains the Simulink models that have been used.

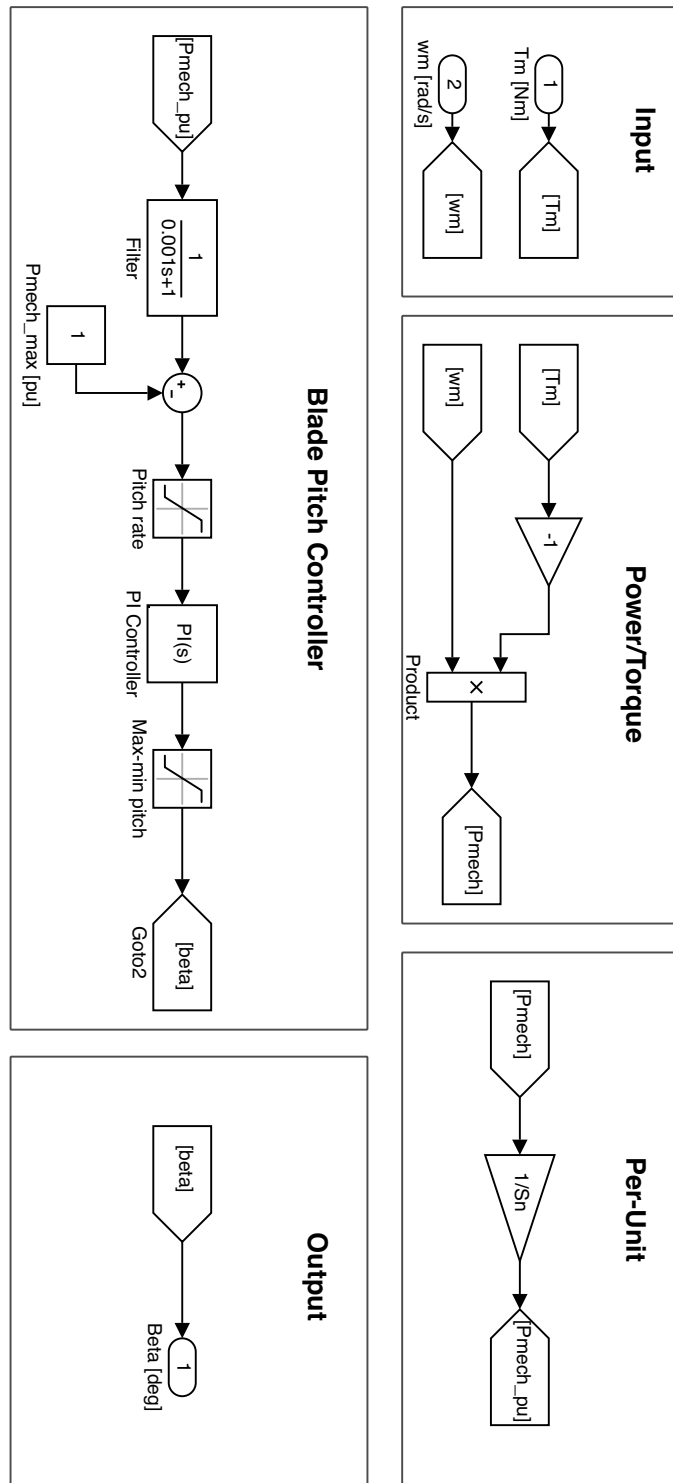
## J.1 Overall System Model



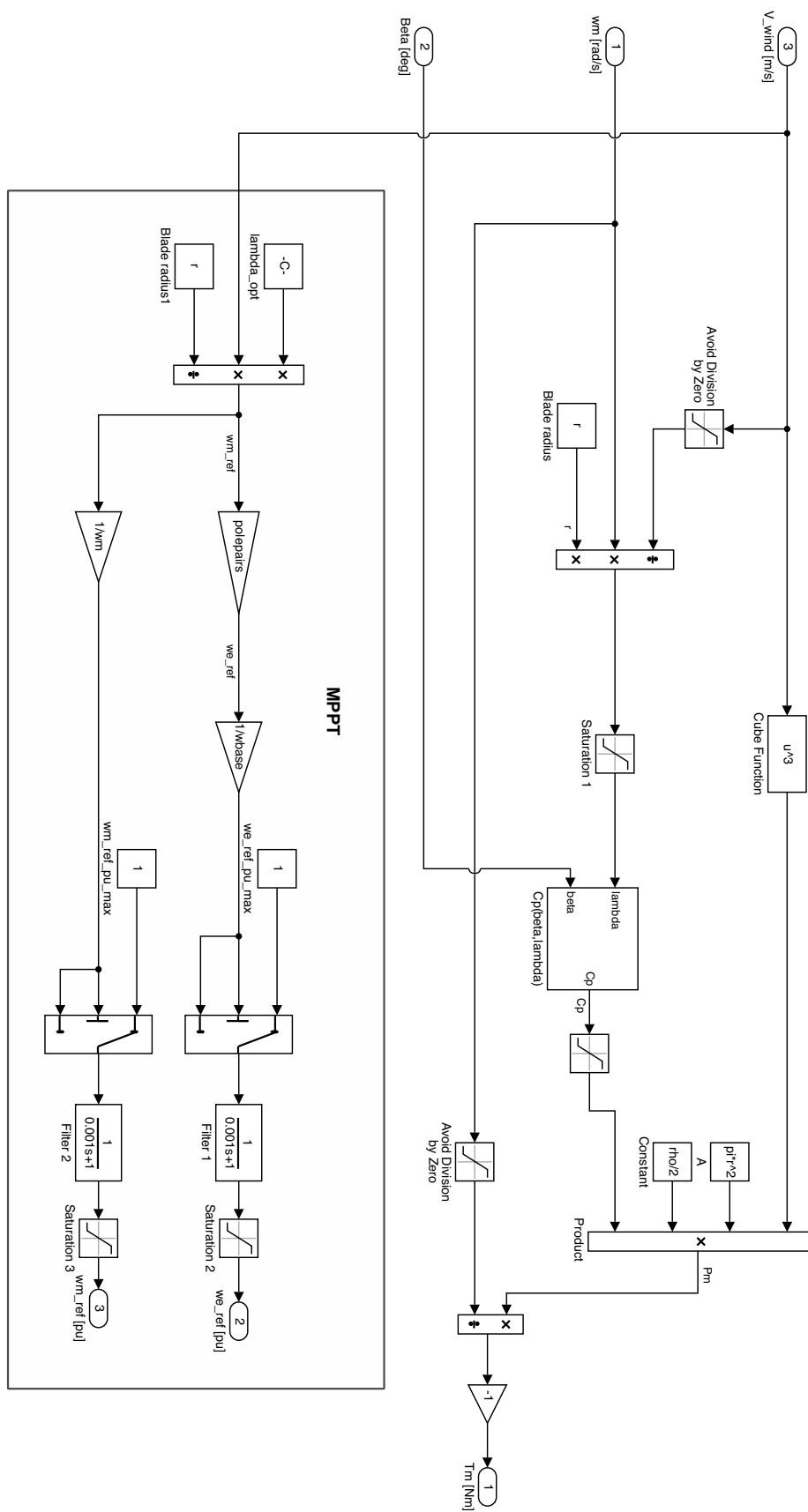
## J.2 Overall Wind Model



### J.3 Pitch Controller

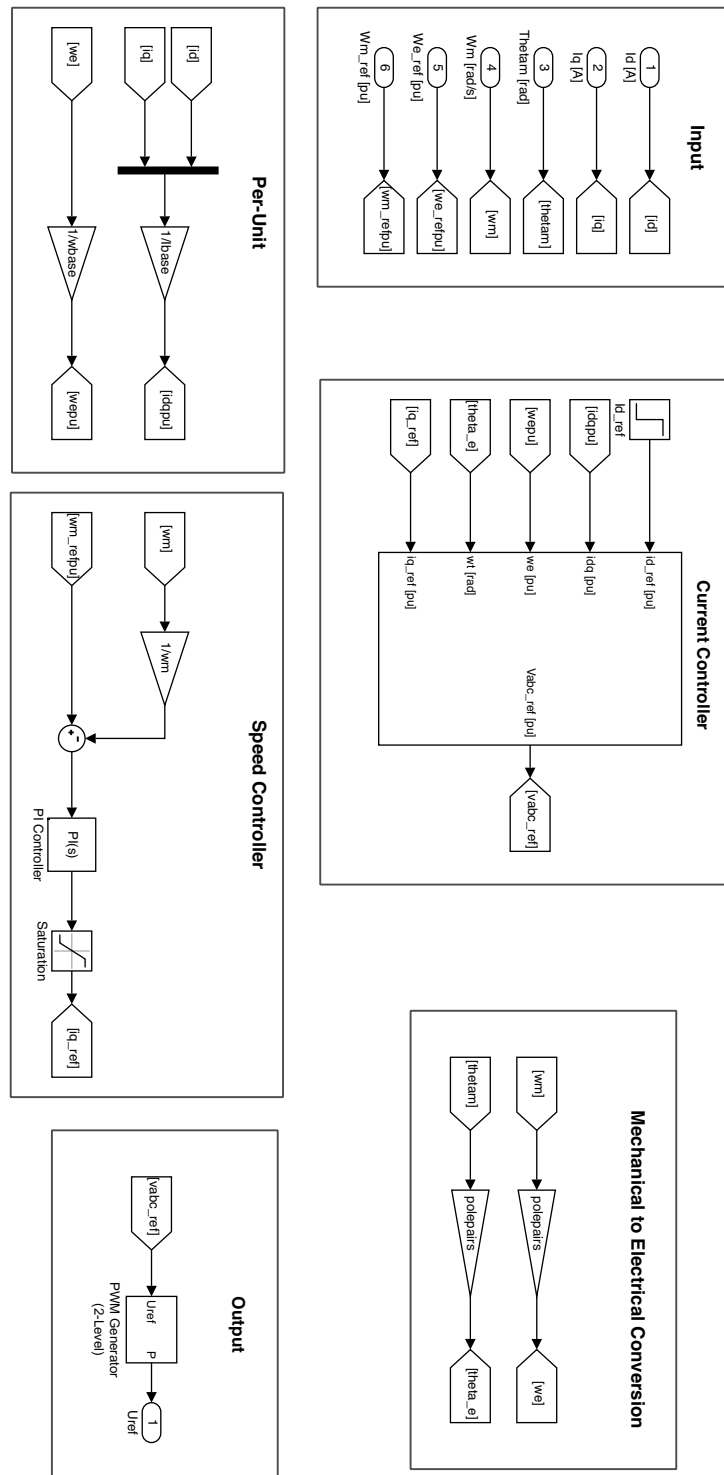


## J.4 Aerodynamic Model

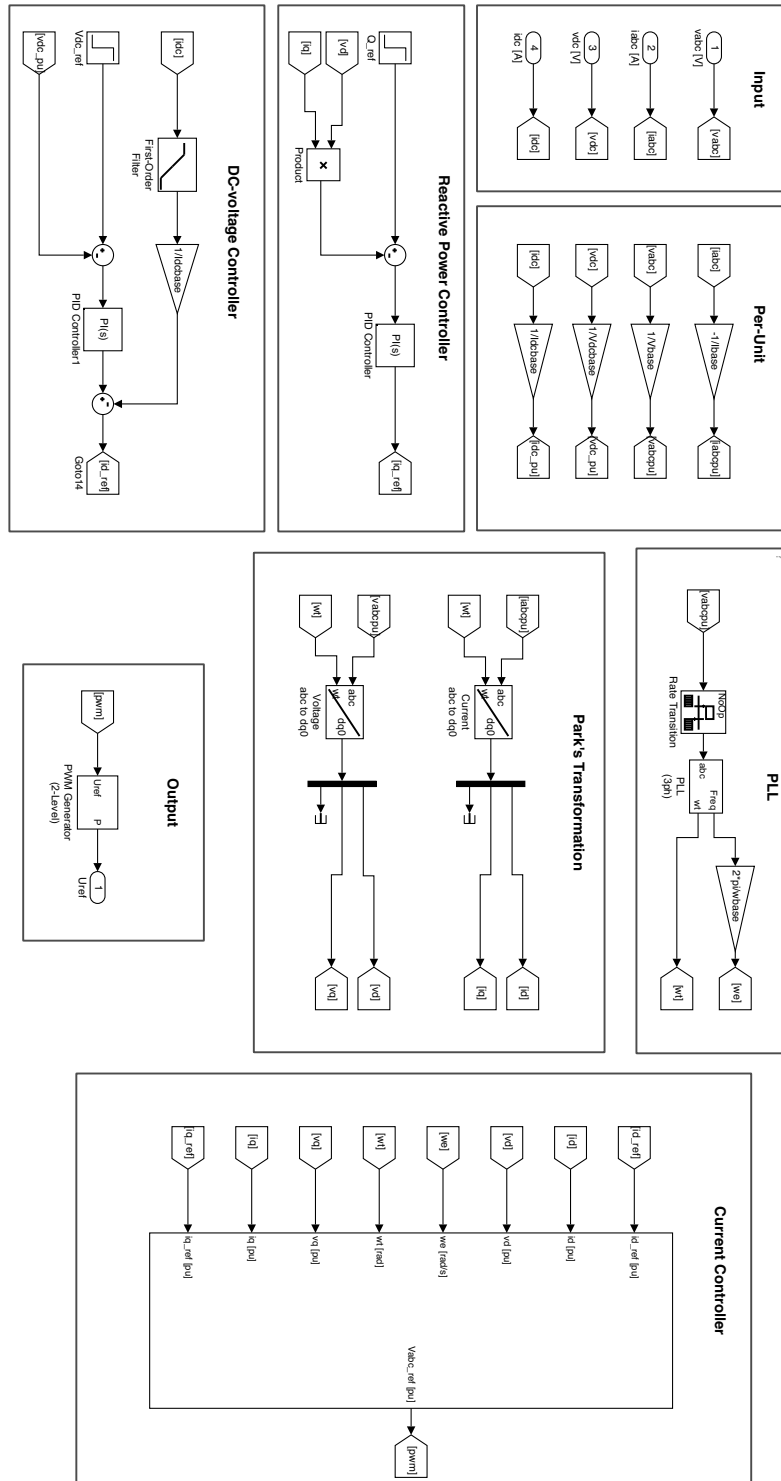




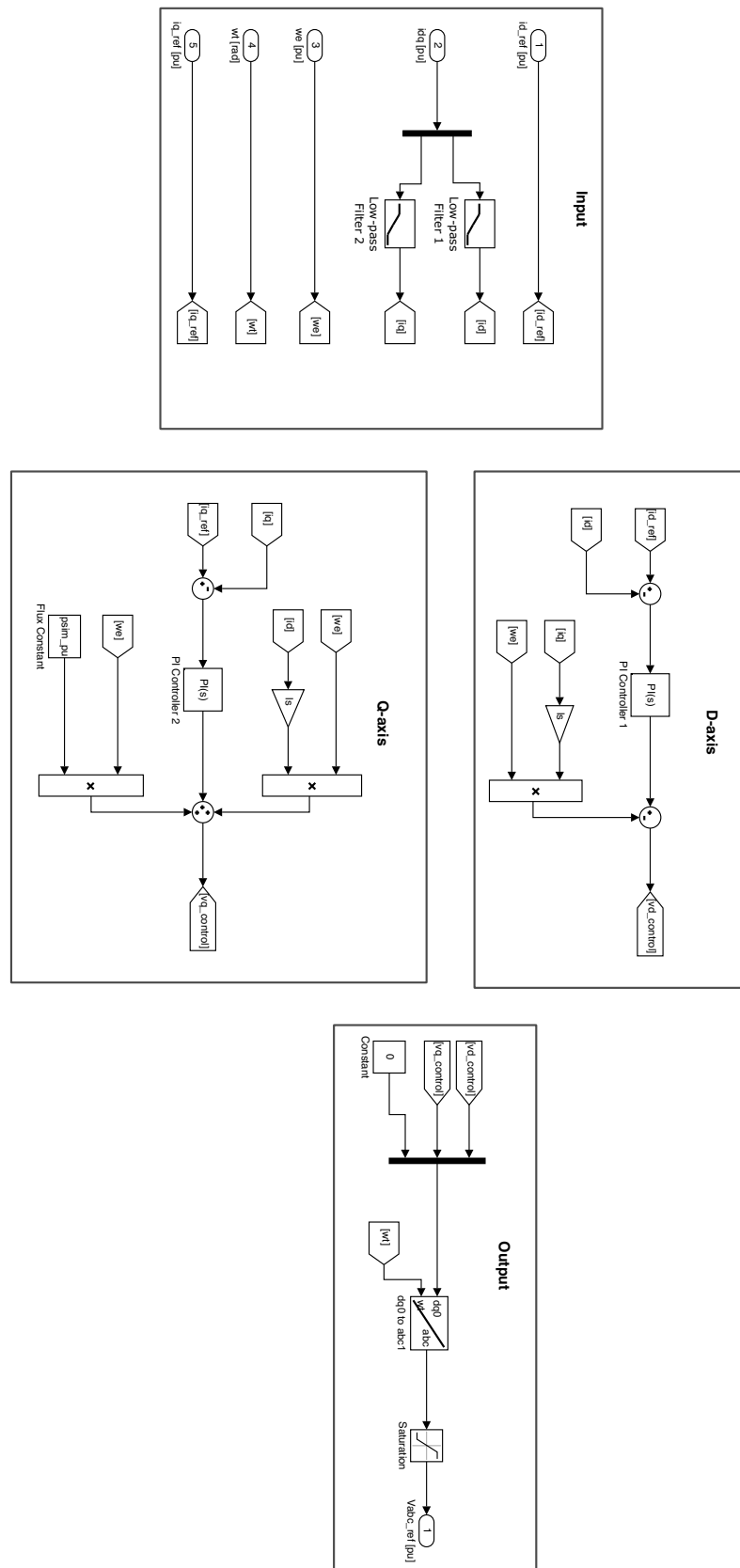
## J.5 GSC Model



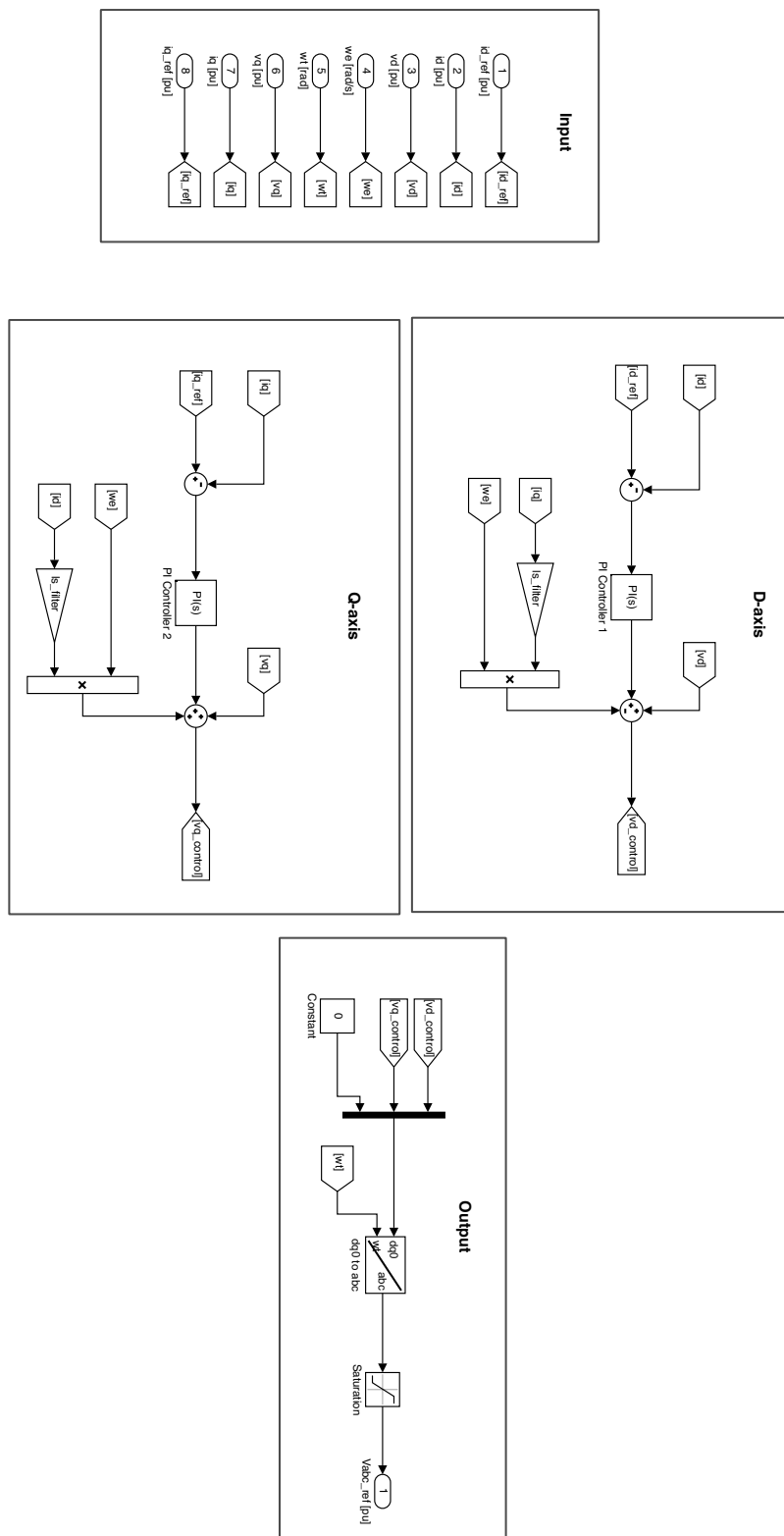
## J.6 SSC Model



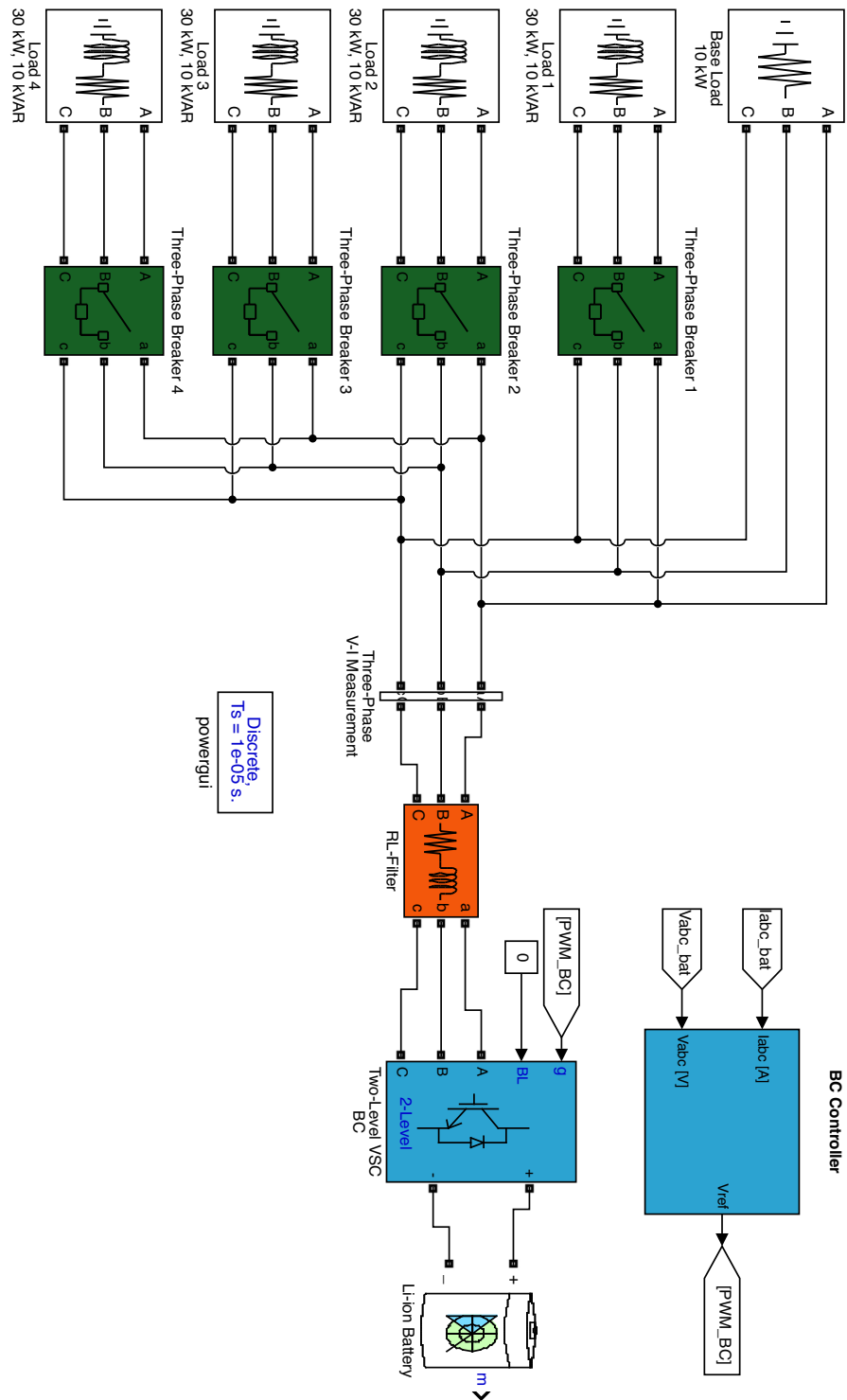
## J.7 GSC Current Control



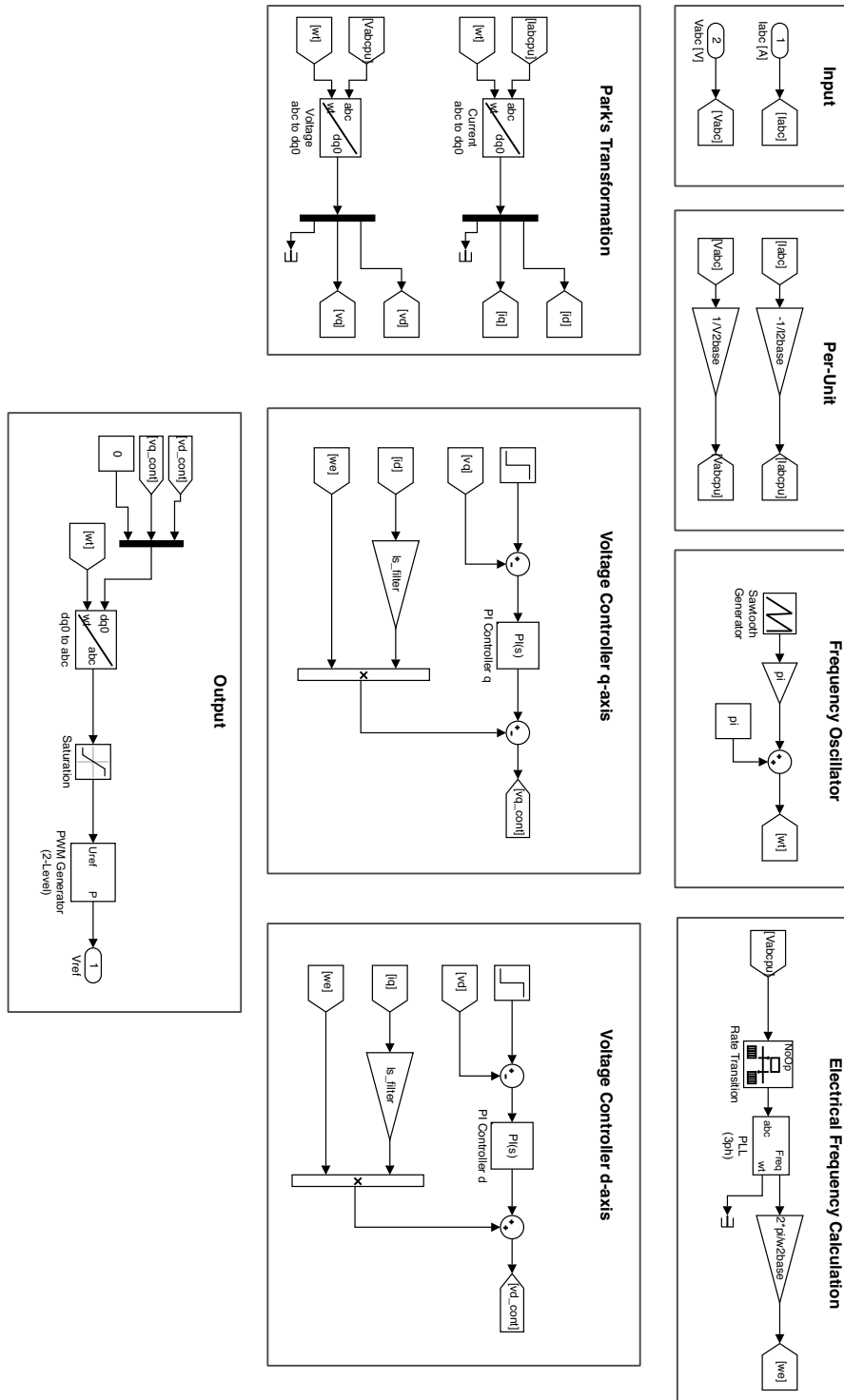
## J.8 SSC Current Control



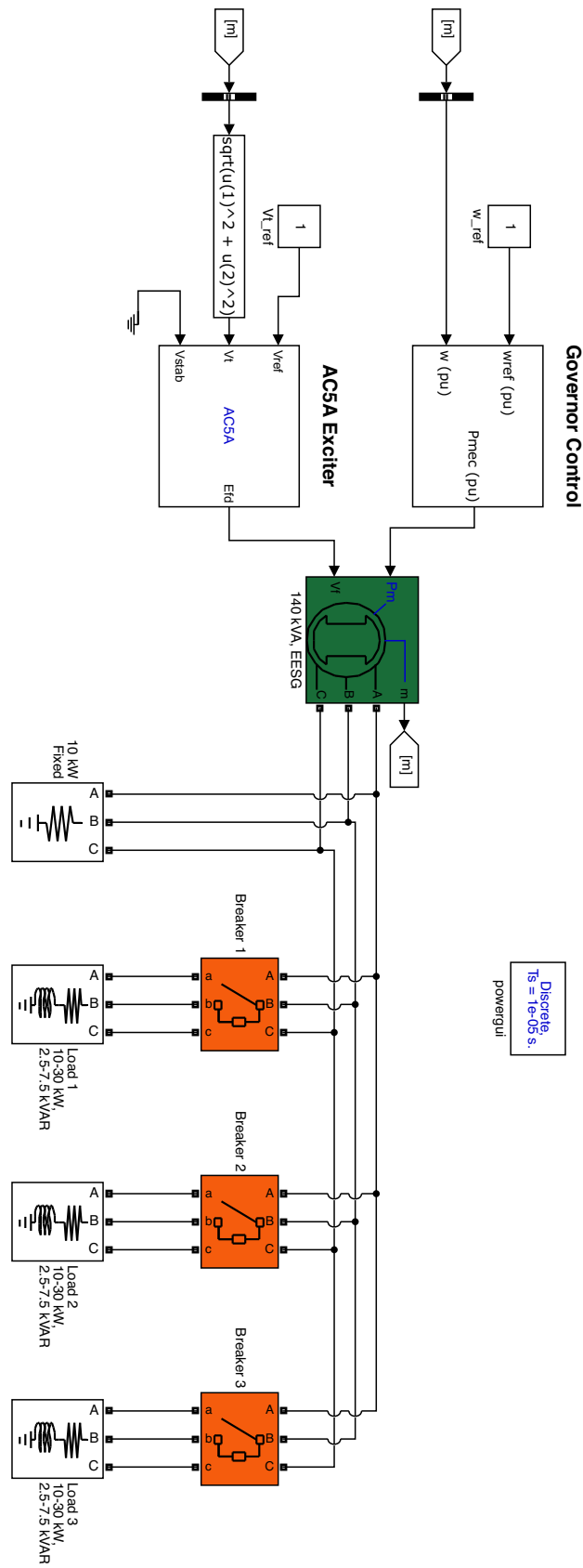
## J.9 Overall Battery Model



## J.10 Battery Converter



## J.11 Overall Diesel Generator Model




# K || PowerPoint from the EERA DeepWind'2017

  
NTNU  
Norwegian University of Science and Technology

## A hybrid wind-diesel stand-alone system for fish farming applications

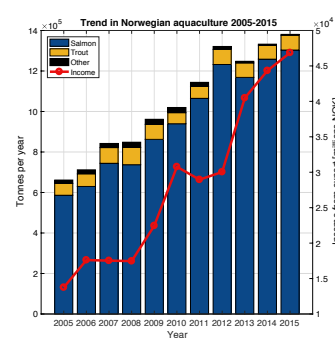
Marius Holt, NTNU

EERA DeepWind'2017

  
NTNU

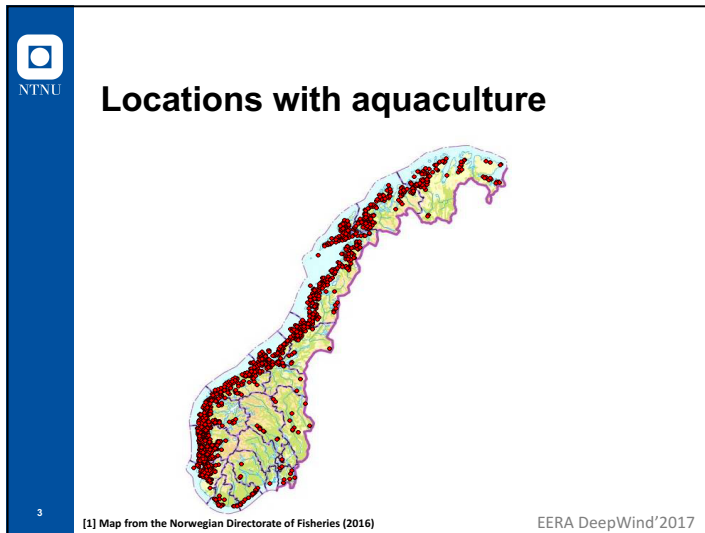
## The Norwegian fish farming industry

- Export 2015: ~47 billion NOK
- Salmon dominates
- Expected to increase further
- Challenges
  - Sea lice
  - Escaping fish
  - Available space
  - Environmental impacts



EERA DeepWind'2017





NTNU

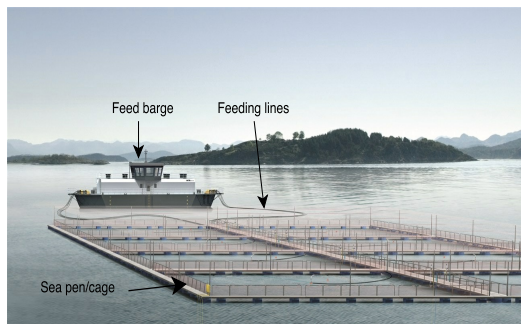
## Problem definition

- Used today: Diesel aggregates
- Desirable to replace diesel with local renewable sources
- Initiative by Pure Farming
- Co-op. with The National Wind Energy Center Smøla (NVES)
- Objective: *Design a hybrid wind-diesel system in order to reduce diesel fuel consumption as much as possible*

4

EERA DeepWind'2017

## A conventional offshore fish farm



[2] Figure based on AKVA Group's brochure "Cage Farming Aquaculture"

5

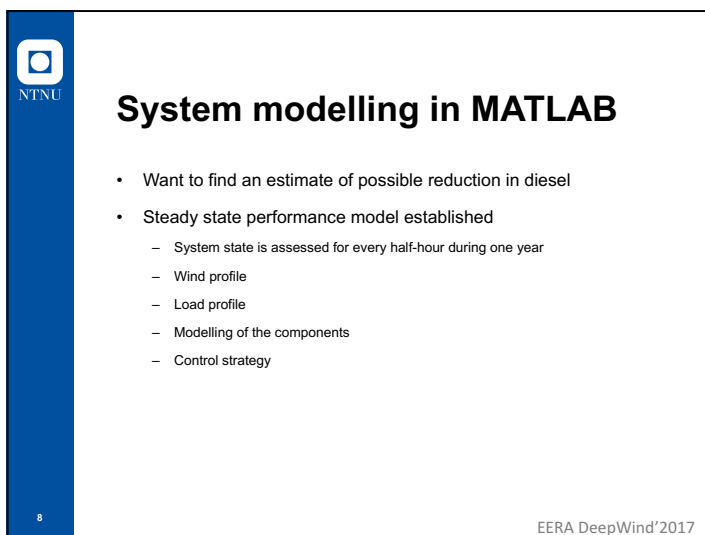
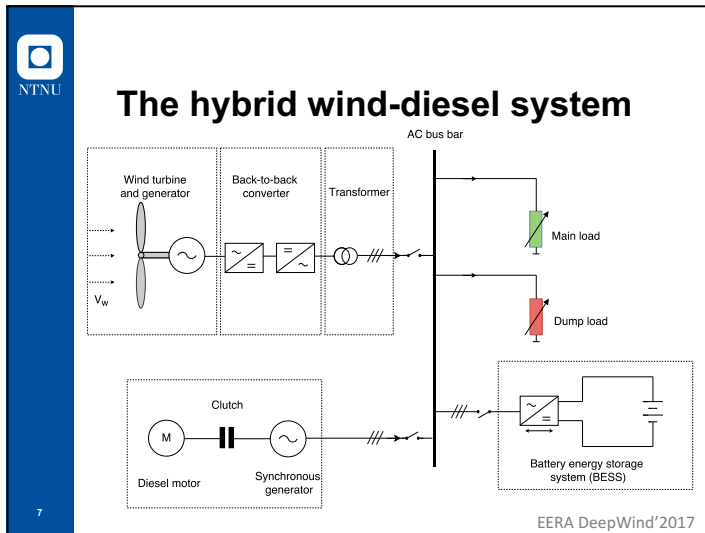
EERA DeepWind'2017

## The proposed fish farm

- Location: Gråøya, close to Smøla
- 6 feed blowers (each rated at 22 kW)
- 12 cages
- LED lightning of cages
- Expected yearly energy consumption: ~470 000 kWh



EERA DeepWind'2017





## Wind profile

- Based on actual data from Veiholmen (1994-2014)
  - Resolution 1 hour
  - Takes into account seasonal variations
- WAsP used to transform wind speeds to hub height and desired geographical location
- Very good wind conditions
  - Average wind speed: 8.7 m/s (1994-2014)

9

EERA DeepWind'2017



## Consumption profile

- Expected yearly energy consumption ~470 000 kWh

### Deterministic load

- Feed blowers and lightning of cages
- Depends on the day length
  - Blowers run at day-time
  - Lightning at night-time
- Blowers: 72.6 kW
- Lightning: 14.4 kW

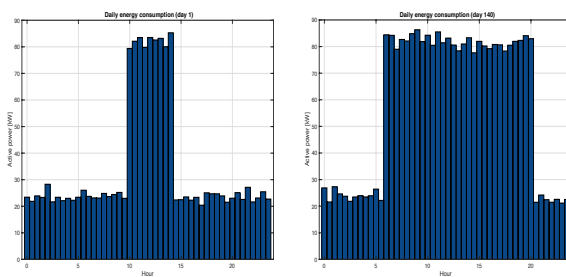
### Stochastic load

- The feed barge's own consumption
  - Heating
  - Lightning
  - Control system
- Gaussian distribution used
  - Expectation: 9 kW
  - Std. deviation: 2 kW

10

EERA DeepWind'2017

## Consumption profile



EERA DeepWind'2017

## Modelling of the components

- Wind turbine: Power curve of an EWT DW52 250 kW turbine used
- Dump load: Operational power range
  - Max and min power limits
- Battery Energy Storing System (BESS) :
  - Max power capability
  - Max energy capacity
  - Depth of discharge
- Diesel aggregate: Treated as the resolving post
  - Fuel consumption predicted by a simple linear relationship

12

EERA DeepWind'2017



## Case studies

- Simulated over the year of 2012
- One base case
- Sensitivity cases on
  - Battery size
  - Depth of discharge
  - Max power to/from battery
  - Dump load margins
- Special cases

13

EERA DeepWind'2017



## Main results

- Battery size have largest impact on diesel fuel
- Potential of ~1 500 000 kWh from wind turbine
  - Dump load margins important
- Wind conditions fairly stable
- Reduction in fuel from approx. 170 000 litres to 25 000 litres yearly solely by including a wind turbine (~85 % reduction)
  - More than 1 million NOK yearly in purchase cost only
  - Very large battery may not be needed

14

EERA DeepWind'2017



## Shortcomings and further work

- Main goal: form a sound decision basis
- Steady state analyses does not take into account
  - Voltage fluctuations
  - Power quality
  - Other transients
- Cost of components and operation not yet surveyed
  - Will be given special focus in the master thesis